Australian National University

Epitaxial growth, optical properties and structural studies of GaN nanorods and related heterostructures

Bijun Zhao

August 2020

A THESIS SUBMITTED FOR THE DEGREE OF DOCTOR OF PHILOSOPHY

OF THE AUSTRALIAN NATIONAL UNIVERSITY

Department of Electronic Materials Engineering

Research School of Physics

College of Sciences

The Australian National University

© Copyright by Bijun Zhao 2020

All Rights Reserved

Declaration

This thesis reports the research I conducted during 2013 and 2020 at the Department of Electronic Materials Engineering, Research School of Physics, The Australian National University, Canberra, Australia.

To the best of my knowledge, the material reported here is original except where acknowledged and reference in appropriate manner. It has not been previously published by others, or submitted in whole or in part for any university degrees.

Bijun Zhao

August 2020

Bijun Zhao

Acknowledgement

My supervisors, colleagues and friends have offered me generous support during my PhD study and contributed greatly to the completion of this thesis. I would like to express my most sincere gratitude to all of them.

First of all, I would like to thank my panel of supervisors: Prof. Chennupati Jagadish, Prof. Hark Hoe Tan, Dr. Philippe Caroff, A/Prof. Jennifer Wong-Leung, and Prof. Lan Fu.

Becoming a member of Jagadish's group is my great privilege. Prof. Chennupati Jagadish, a pioneer and leader in the field of nanotechnology, has inspired students in his group not only to engage in research but also to achieve a good balance between work and life. I always remembered his inspirational words: "*work smart than work hard*". I also like to thank Prof. Hoe Tan as the chair of my supervisory panel. He is the most efficient and fair supervisor I have ever met. The research in this thesis largely arises from my fruitful discussions with Hoe, who always provide useful advice. I also would like to thank Dr. Philippe Caroff, who has encouraged and guided me through my early stages in Ph.D. studies. Although he has left the university, I shall always appreciate the knowledge and time he has shared with me. I also like to thank A/Prof. Jennifer Wong-Leung for her guidance in TEM and life as well. She is always happy to share her ideas on TEM analysis with me and I would like to thank her for encouraging me to keep persevering with my PhD at times when it seems like too steep a mountain to climb. I also would like to thank Prof. Lan Fu for her guidance through the years where she not only act as my supervisor but also acts as an HDR convenor in our school. I would like to thank her for providing advice in nano-fabrication and also for my daily life as well.

I would like to thank the Australian National Fabrication Facility (ANFF) ACT node for providing all the essential equipment and technical support. Dr. Mark

Lockrey, Dr. Li Li, Dr. Mykhaylo Lysevych, Dr. Kaushal Vora, and Dr. Naeem Shahid from ANFF all offered me tremendous help. A special thanks go to Dr. Mark Lockrey for teaching and discussing CL related research topics with me. We worked closely together in optimising the CL measurement procedures and also being a very kind friend. I would like to thank Dr. Li Li and her husband Dr. Xiangyuan Cui for their great friendship that warmed my heart during my stay in Canberra. Dr. Li Li has worked very hard to help me get the lamellae in FIB, which is a tough and time-consuming task.

Our research group is full of talented people who are willing to share their expertise and ideas with me. I would like to thank Dr. Qiang Gao, who has taught me many MOCVD knowledge and always backed me up in life. My thanks also go to Naiyin Wang, Rowena Yew, Dr. Zhe Li, Prof. Fangfang Ren, Prof. Jiandong Ye, Dr. Kun Peng, Dr. Xiaoming Yuan, Dr. Qian Gao, Dr. Dipankar Chugh for sharing their expertise and friendship with me. With their collegiality and encouragement, I never felt lonely and kept on working hard. I also like to thank Dr. Ziyuan Li, Dr. Fan Wang, Dr. Sudha Mokkapati, Dr. Nian Jiang, Dr. Aruni Fonseka, Dr. Amira Ameruddin and Dr. Inseok Yang for showing their valuable knowledge with me during my stay in the group. These colleagues and friends have been role-models for me to live up to.

I also like to thank the collaborators who have contributed to this thesis. I would like to thank Dr. Gilberto Casillas Garcia at the Electron Microscopy Centre at the University of Wollongong and Paul Guagliardo at Centre for Microscopy, Characterisation and Analysis at the University of Western Australia. They have provided help in Cs-corrected TEM imaging and nano-SIMS imaging, respectively. I also like to thank Dr. Xu Zhang in his discussion on the strain.

The Research School of Physics has some of the best administrative staff I know. Julie Arnold, being our Departmental Administrator, is always being helpful and extremely efficient. She has helped me with various complicated paperwork and my travels, which allows me to only focus on research. Karen Nulty and Liudmilla Mangos are also acknowledged for their kind assistance in sorting out my

admission in the Ph.D. program, and assisting in my scholarship and travel grant applications.

Last but not least, I would like to thank my family members and friends. I would like to thank my father, Prof. Nianshun Zhao, and my mother, Juanjuan Li, for always caring for me and not giving me too much pressure. I would like to thank my dear husband Dr. Xin Chen and our family members. Xin has travelled with me to Australia and did his Ph.D. in ANU as well. I cannot finish my thesis without his love and encouragement. I would like to thank Miffy, Bruno, and Mochi for comforting me at my hardest time of life. I would like to thank Naiyin, for being a very good friend of mine for over 10 years and supporting me over the years. Finally, I would like to thank my best friend Kunrong Yang and her husband David Lockwood for sharing a lot of laughter and providing me a lovely home to live.

Abstract

Group III-nitride nanorods have attracted substantial research focus thanks to their direct bandgap, full solar spectrum coverage, and wide optoelectronic applications. GaN nanorod growth has been achieved by several growth methods, and among them, self-assembled nanorod growth by metalorganic chemical vapour deposition (MOCVD) is an optimal and time-saving method due to its catalyst-free and minimal substrate preparation requirements. This approach has been applied in devices that do not demand precise positionings, such as single nanorod light-emitting diodes (LEDs) and flexible nanorod array LEDs.

This dissertation presents a detailed growth study of GaN self-assembled nanorods on sapphire (0001) substrates by MOCVD. Both the pre-growth and growth parameters have been systemically studied. Due to their wurtzite crystal structure, how to control their polarity has been a critical issue in the nanomaterial growth and nano-device fabrication. In this thesis, we show and discuss how the polarity and optical properties are affected by nitridation, one of the pre-growth conditions. With appropriate nitridation, the nanorods can be grown with uniform hexagonal morphology and N-polar, resulting in homogenous luminescence with a strong near-band edge emission. This thesis also studies the effect of growth parameters such as silane co-injection, growth temperature, and growth time on the morphology and density of the nanorods.

Rosette-shaped cathodoluminescence (CL) patterns are found in GaN nanodisks and nanorods. This unique pattern forms at a very early stage of nanorod growth and consists of yellow luminescence (YL) and non-luminous regions. To explore its origin, CL, electron microscopy, and nanoscale secondary ion mass spectrometry studies are conducted. These studies found optical resonance modes and polarity inversion do not contribute to this phenomenon. Higher concentration of carbon and nitrogen clusters are found at the pattern area, which indicates pattern could be related to facet preferential distribution of defects related to excess

carbon/nitrogen. This study adds the knowledge of defect-related emission in GaN nanorod, which is essential for future optoelectronic applications.

Finally, this dissertation presents the growth of $In_xGa_{1-x}N$/GaN multi-quantum well (MQW) core-shell structures and the formation of $In_xGa_{1-x}N$ quantum dots (QDs). Through high-resolution CL and transmission electron microscopy (TEM) studies, the strong QW emission is found only at the tip area and indium segregation is observed at the nanorod sidewall MQW area. The $In_xGa_{1-x}N$ MQW emission shows high sensitivity to minor changes in trimethylindium source flow and quantum barrier growth temperature. The MQW emission shifts to longer wavelengths due to increasing indium source supply and decreasing quantum barrier growth temperature as a result of higher indium incorporation. This study extends our knowledge of growth & optical properties of $In_xGa_{1-x}N$/GaN MQW and QDs, which also demonstrates their potential of application in LEDs in the future.

Publications

Journal articles

1. B. Zhao, M. N. Lockrey, P. Caroff, N. Wang, L. Li, J. Wong-Leung, H. H. Tan and C. Jagadish, *Effect of nitridation on the polarity and optical properties of GaN self-assembled nanorods*. Nanoscale, 2018. **10**(23): p. 11205-11210. DOI: 10.1039/C8NR00737C

2. B. Zhao, M. N. Lockrey, N. Wang, P. Caroff, X. Yuan, L. Li, J. Wong-Leung, H. H. Tan and C. Jagadish, *Highly regular rosette-shaped cathodoluminescence in GaN self-assembled nanodisks and nanorods*. Nano Research, 2020. DOI: 10.1007/s12274-020-2886-6

3. N. Wang, X. Yuan, X. Zhang, Q. Gao, B. Zhao, L. Li, M. Lockrey, H. H. Tan, C. Jagadish and P. Caroff, *Shape engineering of InP nanostructures by selective area epitaxy*. ACS Nano, 2019. **13**(6): p. 7261-7269. DOI: 10.1021/acsnano.9b02985

Conference papers

1. B. J. Zhao, M. N. Lockrey, N. Y. Wang, L. Li, F. Kremer, J. Wong-Leung, P. Caroff, H. H. Tan, and C. Jagadish, *Exploring the Highly regular rosette-shaped cathodoluminescence in GaN self-assembled nanodisks and nanorods*. Material Research Society (MRS) 2017.

2. B. J. Zhao, M. N. Lockrey, N. Y. Wang, L. Li, F. Kremer, J. Wong-Leung, P. Caroff, H. H. Tan, and C. Jagadish, *Wafer scale self-organized InGaN multiple quantum well columns grown on sapphire substrates*. International Conference on Nanoscience and Nanotechnology (ICONN) 2016.

3. B. J. Zhao, M. N. Lockrey, N. Y. Wang, L. Li, F. Kremer, J. Wong-Leung, P. Caroff, H. H. Tan, and C. Jagadish, *Effect of nitridation on the polarity and optical properties of GaN self-assembled nanorods*. International Conference on Optoelectronics and Microelectronics Materials and Devices (COMMAD) 2016.

Acronyms and Symbols

ABF	annular bright-field
BSF	basal plane stacking faults
CBED	convergent beam electron diffraction
CBM	conduction band minimum
CL	cathodoluminescence
Cs-corrected	aberration-corrected scanning transmission
STEM	electron microscope
CVD	chemical vapour deposition
D°h	free hole transition
DAP	donor-acceptor pair
DFT	density functional theory
eA°	free electron to acceptor transition
EBL	electron beam lithography
E_C/E_V	conduction/valence band
E_D/E_A	donor/acceptor level
EDX	energy dispersive X-ray spectroscopy
EELS	electron energy loss spectroscopy
EL	electroluminescence
FIB	focused ion beam
Ga_i/N_i	gallium/nitrogen interstitial
Ga_N/N_{Ga}	gallium/nitrogen antisite
HAADF	high-angle annular dark-field
H_i	hydrogen interstitial
HVPE	halide vapour phase epitaxy
KPFM	kelvin probe force microscopy

LED	light-emitting diodes
MBE	molecular beam epitaxy
MOCVD	metalorganic chemical vapour deposition
MOVPE	metalorganic vapour phase epitaxy
MQW	multi-quantum well
nano-SIMS	nanoscale secondary ion mass spectrometry
NBE	near-bandgap emission
NH_3	ammonia
PAS	positron annihilation spectroscopy
PL	photoluminescence
QCSE	quantum-confined Stark effect
QD	quantum dot
QW	quantum well
SAD	selective area diffraction
SAE	selective area epitaxy
SEM	scanning electron microscope
SiH_4	silane
SRH	Shockley-Read-Hall
STEM	scanning transmission electron microscopy
TEGa	triethylgallium
TEM	transmission electron microscope
TMAl	trimethylaluminium
TMGa	trimethylgallium
TMIn	trimethylindium
V_{Ga}/V_N	gallium/nitrogen vacancy
VLS	vapour-liquid-solid
VSS	vapour-solid-solid

YL	yellow luminescence
ZPL	zero phonon line

Table of Contents

Declaration iii
Acknowledgement v
Abstract ix
Publications xi
Acronyms and Symbols xii
List of Figures and Tables xix

Chapter 1: Introduction 1
- 1.1 Significance of GaN nanorods 1
- 1.2 Techniques for the synthesis of GaN nanorods 2
- 1.3 Challenges in GaN nanorod growth and thesis motivation 3
- 1.4 Thesis Synopsis 4
- References 6

Chapter 2: Background and experimental techniques 12
- 2.1 Introduction 12
- 2.2 Backgrounds 12
  - 2.2.1 Crystal structure and polarity of III-nitride material 12
  - 2.2.2 Bottom-up GaN nanorod synthesis approach 15
    - 2.2.2.1 Catalyst-assisted approach 15
    - 2.2.2.2 The selective-area epitaxy 16
    - 2.2.2.3 The self-assembled growth 20
  - 2.2.3 Point defects 22
    - 2.2.3.1 Extrinsic point defects 22
    - 2.2.3.2 Intrinsic point defects 24
  - 2.2.4 Optical properties of GaN 26
  - 2.2.5 GaN nanorod LED 28
- 2.3 Experimental techniques 31
  - 2.3.1 Epitaxial growth: MOCVD technique 31
  - 2.3.2 Thermal evaporation 35
  - 2.3.3 Scanning electron microscope 36
  - 2.3.4 Energy-dispersive X-ray spectroscopy 37
  - 2.3.5 Cathodoluminescence 38
  - 2.3.6 Transmission electron microscope 40

2.3.7 Scanning transmission electron microscope 41
2.3.8 Focused ion beam for TEM sample preparation 42
2.3.9 Nanoscale secondary ion mass spectrometry 46
References 48

Chapter 3: Growth of GaN nanorods 60
3.1 Introduction 60
3.2 Experiments 61
3.3 Studies of Pre-growth conditions 62
3.3.1 Surface nitridation 63
3.3.1.1 Nitridation effects on crystal morphology 63
3.3.1.2 Nitridation effects on polarity 66
3.3.1.3 Cathodoluminescence on nitridation 68
3.3.1.4 Summary on nitridation 74
3.4 Studies of growth parameter 75
3.4.1 Effects of silane injection 75
3.4.2 Effects of growth temperature 76
3.4.3 Effects of growth time 77
3.5 Summary 78
References 78

Chapter 4: Rosette-shaped cathodoluminescence pattern in GaN nanostructures 82
4.1 Introduction 82
4.2 Experiment 83
4.3 CL observaton of the rosette-shaped pattern 84
4.4 Optical modes inside the hexagonal cavity 88
4.5 Polarity determination and STEM imaging 90
4.6 Strain analysis 94
4.7 Nano-SIMS studies 95
4.8 Evolution of the CL pattern 97
4.9 Summary 100
References 100

Chapter 5: Growth and characterisation of $In_xGa_{1-x}N$ quantum wells and quantum dots in GaN nanorods 105

5.1 Introduction 105
5.2 Experiment 106
5.2.1 Growth of $In_xGa_{1-x}N$ MQWs on GaN nanorods 106
5.2.2 Optical and structural characterisations 106
5.3 $In_xGa_{1-x}N$/GaN MQWs and $In_xGa_{1-x}N$ QDs 107
5.4 Summary 113
References 113

Chapter 6: Conclusion 116
6.1 Outcomes 116
6.2 Outlook and future work 117
6.2.1 Challenges in nanorod growth and characterisation 117
6.2.2 Future Outlook 118
References 119

List of Figures and Tables

Figure 1.1 Bandgap as a function of lattice constant for III-nitrides
and a few commonly used substrates for growth 2
Figure 2.1 Schematic drawing of GaN crystal structure 13
Table 2.1 Material properties of GaN, AlN, InN, and sapphire........ 13
Figure 2.2 Schematic drawing of Ga-polar and N-polar GaN. 14
Figure 2.3 Schematic illustration of catalyst-assisted nanorod growth. 15
Figure 2.4 Schematic drawings of selected area epitaxy of nanorods. 17
Figure 2.5 Illustrations of different growth modes used in SAE
growth of GaN nanorods 17
Figure 2.6 H-passivation effects on Ga-polar and N-polar GaN 18
Figure 2.7 Schematic model for pulsed mode demonstrating
the effect of NH_3 interruption. 19
Figure 2.8 Schematic drawing illustrating the various processes
occurring during self-assembled nanowire growth. 20
Figure 2.9 Formation energy of carbon-related point defects and
schematic illustration of C_N^+ in GaN 23
Figure 2.10 Charge density of the localized defect state of V_N and V_{Ga} 25
Figure 2.11 The energy transition between initial states E_i and
final states E_f for direct and indirect bandgap semiconductor 26
Figure 2.12 Schematic drawing of the radiative energy transition
in the semiconductor. 27
Figure 2.13 Typical optical emission peaks of GaN 28
Figure 2.14 Schematic drawing of GaN-InGaN MQW structure. 29
Figure 2.15 A photo and a schematic drawing of the Aixtron 3×2FT
close-coupled showerhead MOCVD system. 32
Figure 2.16 Schematic drawing of the gas circuit diagram
in an MOCVD system. 33
Figure 2.17 MOCVD reactor and heating coils. 33
Figure 2.18 Schematic drawing of precursors reaction
inside the MOCVD chamber 34
Figure 2.19 Schematic drawing and a photo of thermal
evaporator system. 35
Figure 2.20 Schematic drawing of an SEM system. 36
Figure 2.21 Different signals produced when an electron
beam impinges on a sample 36

Figure 2.22 Schematic drawing of EDX process and an example of GaN STEM/EDX map 38
Figure 2.23 Schematic drawings and photo of a CL system. 39
Figure 2.24 Schematic drawings of the imaging system in TEM. 40
Figure 2.25 Schematic drawing of the effect of spherical aberration in a geometrical optics view. 41
Figure 2.26 Schematic drawings of a dual FIB-SEM system and related-process 43
Figure 2.27 Schematic drawings, photo and SEM images of the FIB-lamella preparation process. 45
Figure 2.28 Schematic drawing of the ion bombardment process at a metal surface 46
Figure 2.29 Schematic drawing of the Cameca Nano-SIMS 50/50L machine. 48
Figure 3.1 Illustration for the self-assembled growth of nanorods used in the work. 61
Figure 3.2 45° SEM images of samples with nitridation time ranging from 0 to 600 s 63
Figure 3.3 Statistical studies of nanorod morphology with varied nitridation durations 64
Figure 3.4 Polarity determination of nitridated and non-nitridated sample using Cs-corrected TEM. 66
Figure 3.5 45° SEM and corresponding panchromatic CL images of nanorods grown on sapphire substrate with various nitridation time from 0 to 600s. 68
Figure 3.6 SEM and panchromatic CL images of a nanorod viewed from different rotation angles ranging from 0 to 300 ° 69
Figure 3.7 Optical properties of a non-nitridated nanorod a 300 s nitridated nanorod 70
Figure 3.8 SEM and panchromatic CL images focused at the middle/bottom areas of both non-nitridated and 300 s nitridated samples 71
Figure 3.9 SEM and panchromatic CL images of the nanorod cross-sections sliced by FIB 73
Figure 3.10 SEM images of GaN nanorods grown with different silane co-injection flow rates ranging from 0 to 500 nmol/min 75
Figure 3.11 SEM images and statistic study of nanorods with different growth temperatures 76
Figure 3.12 SEM images and statistic study of nanorods with different growth times 77
Figure 4.1 SEM and panchromatic CL images of GaN nanostructures with rosette-shaped pattern 84

Figure 4.2 Composite images reconstructed from red-green-blue (RGB) color filters ... 86
Figure 4.3 Low-temperature (80 K) spectral imaging and spectra of GaN nanostructure ... 87
Figure 4.4 SEM images of intentionally broken and merged GaN nanodisks ... 88
Figure 4.5 SEM and corresponding panchromatic CL images of a nanorod at different acceleration voltages ... 89
Figure 4.6 Polarity determination at various spots in a GaN nanorod lamella sample ... 90
Figure 4.7 STEM images of a nanodisk lamella attached to the substrate ... 92
Figure 4.8 SEM, panchromatic CL and STEM images of a lamella sliced before reaching the turning point in the diamond shape. ... 93
Figure 4.9 TEM images and GPA maps at middle/edge of a GaN nanorod lamella ... 94
Figure 4.10 SEM images, nano-SIMS maps, and nano-SIMS line-scans of a nanorod lamella sample ... 95
Figure 4.11 SEM& panchromatic CL composite images and statistical analyses of the CL pattern ... 97
Figure 4.12 CL pattern evolution. ... 98
Figure 5.1 SEM , panchromatic CL images, and CL spectrum of GaN nanorods with MQW structure ... 107
Figure 5.2 STEM bright field image of the MQW cross-section lamella ... 109
Figure 5.3 TEM images of the dot-like formation on the surface of the $In_xGa_{1-x}N$ MQWs ... 110
Figure 5.4 SEM and panchromatic CL images of the QDs ... 110
Figure 5.5 SEM, panchromatic CL images and CL spectra of the MQW and QDs ... 111
Figure 5.6 CL spectra studies of MQW with indium injection concentration and barrier growth temperature variations ... 112
Figure 6.1 Illustrations of single nanorod contacting and single nanorod LED. ... 119

Chapter 1

Introduction

1.1 Significance of GaN nanorods

GaN is a binary III/V semiconductor with a wide and direct bandgap of 3.4 eV. It can form ternary alloys with AlN (6.01 eV) and InN (0.65 eV) such that its bandgap can be tuned from deep UV to near-infrared, thereby offering full coverage of the solar spectrum. The tuneable bandgap makes it a popular candidate for the application of optoelectronics including lasers [1], solar cells [2-4], light-emitting diodes (LED) [5-7], and photo-detectors [8-10].

However, there are still several challenges in the epitaxial growth of GaN such as a high dislocation density in heteroepitaxy and the immature technology of GaN native substrates. Reducing the dislocation density is one of the key challenges. For GaN planar growth, dislocation density [11] can be as high as 10^8-10^9 cm^{-2} due to thermal expansion and lattice mismatch with the foreign substrates they are normally grown on, such as sapphire, silicon and silicon carbide. Such high dislocation density lowers the efficiency in device applications such as by forming non-radiative recombination centres that quench the light emission [12]. GaN based planar device are usually grown on the c-plane of wurtzite phase substrates in the polar [0001] direction. Such structures result in a strong spontaneous and strain-induced polarization that leads to an internal built-in electric field. Due to this electric field, the potential band tilts in quantum well (QW) structures, resulting in spatial separation between the electrons and holes that lowers the radiative combination efficiency in the QWs. This phenomenon is known as the quantum-confined Stark effect (QCSE), which could be minimized by growing on the non-polar and semi-polar planes. However, reports [13-16] have shown that dislocation density might be even higher when growing GaN and related structures on non-polar and semi-polar directions. Growing directly on native GaN substrates or thick GaN templates may alleviate this issue but the cost of these substrates and templates is

still prohibitive [17-19].

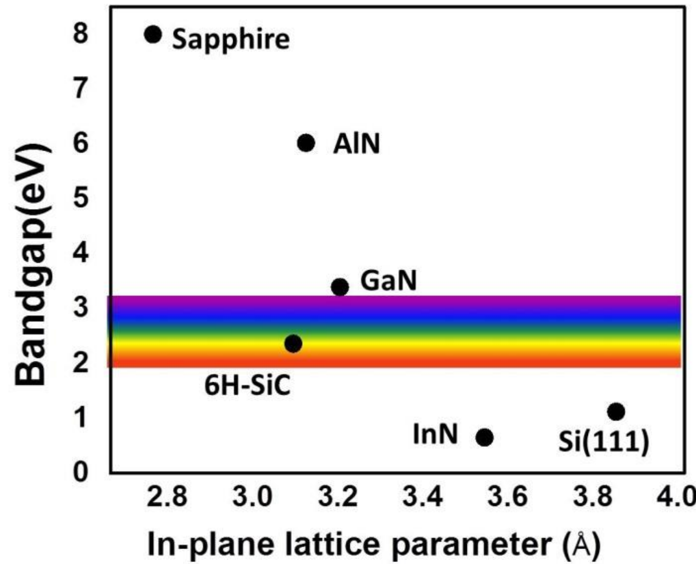

Figure 1.1 Bandgap as a function of lattice constant for III-nitrides and a few commonly used substrates for growth.

The growth of the nanorods or nanowires provides a new prospect to tackle these challenges.

(i) Benefiting from a small footprint, GaN nanorods are less strained in hetero-epitaxial growth and threading dislocation density can be largely reduced [20] by changing the growth conditions through spatial filtering and dislocation bending.

(ii) Due to their inherent 1D geometry, the larger surface area on the sidewalls decreases current overcrowding due to carrier injection that helps to relieve the efficiency droop phenomenon [21] in III-nitride LEDs.

(iii) The sidewalls of the nanowires have nonpolar and/or semi-polar planes which can negate the spontaneous and piezoelectric polarization effect. Therefore, InGaN QW structures grown on the sidewalls of GaN nanorods are free from QCSE [22]. Thicker quantum wells could also be grown on the sidewalls that helps to relieve current leakage issues in LEDs and laser diodes, thereby increasing their radiative recombination efficiency.

1.2 Techniques for the synthesis of GaN nanorods

There are two basic approaches in the synthesis of GaN nanorods: top-down and

bottom-up. In the top-down method [23-25], the nanostructures are formed by shaping the bulk layer by lithography or electrophoresis through a mask, followed by etching. This method provides precise positioning of the arrays and the size of the nanorods are controlled through the etching process. However, because its crystal quality and epitaxy design are restricted to the bulk layer, many advantages of nanostructures such as elastic strain relaxation, spatial filter effects, and material saving are lost in this approach. Extra fabrication processes are required and surface defects [26, 27] could be introduced during the etching process, which in turn may affect the electrical and optical properties of nanorods.

The bottom-up approach involves directly synthesizing the nanostructures by combining the constituent atoms. The nanorods with desired morphology, electrical, and optical properties could be achieved by controlling the growth parameters. To date, GaN nanorods have been grown by a number of techniques: sputter deposition [28, 29], chemical vapour deposition (CVD) [30, 31], molecular beam epitaxy (MBE) [32-36] halide vapor phase epitaxy(HVPE) [37-39], and metalorganic chemical vapour deposition (MOCVD) [40-42]. In this thesis, we focused on the growth of nanorods using MOCVD, which is a dominant method in the industry for growing GaN and related materials. In the bottom-up approach, it can be further categorized into catalyst-assisted and catalyst-free depending on whether a catalyst is used during the growth process.

The catalyst growth includes vapour-liquid-solid (VLS) and vapour-solid-solid (VSS) depending on the catalyst is a liquid or solid. Metal catalysts such as Au [40, 43] and Ni [44] have been used to control the nanorod morphology and optical properties. Catalyst-free approach includes the selective-area growth (SAE) and self-assembled growth. With the help of a regular patterned mask, the SAE approach is able to achieve precise positioning of each nanorod, which is suitable for nanorod array devices application [45, 46]. Self-assembled growth is a mask-free and foreign catalyst-free approach that is suitable for applications without positioning requirements [47]. In self-assembled growth using MOCVD, wafer-scale growth has been achieved on sapphire substrate with silane injection to promote the vertical growth rate [48-50].

1.3 Challenges in GaN nanorod growth and thesis motivation

As discussed in section 1.2, different nanorod synthesis processes have different advantages and limitations. For the most widely used catalyst-assisted VLS growth, it has less requirements in substrate preparation and is easy to achieve large-area growth. The nanorod diameter is determined predominantly by the size of the metal catalyst and the presence of metal particles may deteriorate the performance of the devices. Another approach is SAE growth using a dielectric mask to grow in the openings of the mask and can achieve uniform nanorod arrays with uniform diameter and length. However, the mask patterning process often involves the use of techniques such as nano-imprint or electron beam lithography, which are complex, expensive, and time-consuming. Therefore, it is attractive to investigate mask-free and catalyst-free growth approach such as the self-assembled growth described above. Although there have been several reports in the literature on using this technique to grow GaN nanorods [48-53] and the associated devices [47, 54], some challenges still exist. In particular, controlling the polarity and obtaining a deeper understanding of the growth mechanism and how they affect the optical properties of the nanorods require further investigations.

1. Polarity control.

GaN nanorods with mixed-polarity rods have been found in both SAE and self-assembled growth [49, 50, 55]. Mixed polarity may lead to current leakage in devices [56], which in turn reduces the device efficiency. Therefore, unipolar GaN nanorods are highly desirable to obtain high efficiency nano-devices.

2. Origin of defect-related optical processes

Defect-related optical processes such as YL and non-radiative recombination would reduce the efficiency of the optoelectronic devices and they have long been observed in GaN planar layers [57-59] and nanorods [49, 60]. However, the chemical origin of YL is still under debate [58]. GaN nanorods offer a unique perspective to study the YL and non-radiative recombination. The effects of threading dislocations and grain boundaries are minimized in nanorods [61, 62] and their inherent rod-like geometry offers the opportunity to investigate polar and non-polar planes simultaneously.

1.4 Thesis Synopsis

This dissertation presents a detailed study into the growth and characterization of self-assembled GaN nanorods and InGaN/GaN multi-quantum well core-shell nanorods. The thesis is divided into six chapters.

Chapter 1: The present chapter discusses the advantages of GaN nanorods over their planar counterparts. The various techniques to synthesise these nanorods including catalyst-assisted, selective-area, and self-assembled growth and their advantages and limitations are briefly discussed.

Chapter 2: The second chapter first introduces the general knowledge of III-nitride material. We provide the background information of the crystalline structure, polarity orientations, point defects formation, and bottom-up growth approaches of GaN nanorods. The optical properties and the application of GaN nanorod-based LEDs are also discussed. Then growth and characterization techniques used in this dissertation are discussed.

Chapter 3: This chapter discusses the optimisation of pre-growth and growth conditions of GaN nanorods, and the underlaying growth mechanism. We first studied the effect of pre-growth nitridation on the nucleation, polarity and optical properties of the GaN nanorods. High resolution cathodoluminescence (CL) and aberration corrected transmission electron microscopy (Cs-corrected STEM) were used to obtain a deeper insight into the relationship between the crystal structure of the nanorods and their polarity and optical properties. It is found that high quality GaN nanorods with good optical properties and uniform polarity can be achieved using an optimised nitridation process. Other growth parameters are also studied in this chapter, including growth temperature, silane co-injection, and growth time.

Chapter 4: In this chapter, we investigated a six-fold rosette-shaped cathodoluminescence in the GaN nanorods. We used high-resolution cathodoluminescence, electron microscopy and nano secondary ion mass spectrometry to investigate the origins of this pattern. We found the optical resonance modes or polarity inversion domains are not responsible for the phenomenon. Through chemical composition and geometrical phase analysis (strain analysis), we found that a higher concentration of nitrogen and carbon clusters are associated with the pattern.

Chapter 5: This chapter discusses the growth, structural and optical properties of $In_xGa_{1-x}N$/GaN core-shell MQW nanorods. We found that the QWs at the top of the

nanorods emit strong luminescence, while quantum dot (QD)-like structures are formed on the sidewalls of the nanorods with weaker emission. From the CL mapping, we found these QD-like emissions originate from indium phase segregation in the QWs. The effect of indium precursor flow rate and growth temperature are also studied.

Chapter 6: The last chapter summarized the important experimental findings and also provides prospective for the future works.

References

1. C. Li, J. B. Wright, S. Liu, P. Lu, J. J. Figiel, B. Leung, W. W. Chow, I. Brener, D. D. Koleske, T. S. Luk, D. F. Feezell, S. R. J. Brueck and G. T. Wang, *Nonpolar InGaN/GaN core–shell single nanowire lasers.* Nano Letters, 2017. **17**(2): p. 1049-1055.
2. S. L. Howell, S. Padalkar, K. Yoon, Q. Li, D. D. Koleske, J. J. Wierer, G. T. Wang and L. J. Lauhon, *Spatial mapping of efficiency of GaN/InGaN nanowire array solar cells using scanning photocurrent microscopy.* Nano Letters, 2013. **13**(11): p. 5123-5128.
3. M. Ebaid, J. H. Kang and S. H. Lim, *Enhanced solar hydrogen generation of high density, high aspect ratio, coaxial InGaN/GaN multi-quantum well nanowires.* Nano Energy, 2015. **12**: p. 215-223.
4. A. T. M. Golam Sarwar and R. C. Myers, *Exploiting piezoelectric charge for high performance graded InGaN nanowire solar cells.* Applied Physics Letters, 2012. **101**(14): p. 143905.
5. X. Dai, A. Messanvi, H. Zhang, C. Durand, J. Eymery, C. Bougerol, F. H. Julien and M. Tchernycheva, *Flexible light-emitting diodes based on vertical nitride nanowires.* Nano Letters, 2015. **15**(10): p. 6958-6964.
6. J. R. Riley, S. Padalkar, Q. Li, P. Lu, D. D. Koleske, J. J. Wierer, G. T. Wang and L. J. Lauhon, *Three-dimensional mapping of quantum wells in a GaN/InGaN core–shell nanowire light-emitting diode array.* Nano Letters, 2013. **13**(9): p. 4317-4325.
7. C. Zhao, T. K. Ng, R. T. ElAfandy, A. Prabaswara, G. B. Consiglio, I. A. Ajia, I. S. Roqan, B. Janjua, C. Shen, J. Eid, A. Y. Alyamani, M. M. El-Desouki and B. S. Ooi, *Droop-free, reliable, and high-power InGaN/GaN nanowire light-emitting diodes for monolithic metal-optoelectronics.* Nano Letters, 2016. **16**(7): p. 4616-4623.
8. T. He, X. Zhang, X. Ding, C. Sun, Y. Zhao, Q. Yu, J. Ning, R. Wang, G. Yu and S. Lu, *Broadband ultraviolet photodetector based on vertical Ga_2O_3/GaN nanowire array with high responsivity.* Advanced Optical Materials, 2019. **7**(7): p. 1801563.

9. J. Lahnemann, A. Ajay, M. I. Den Hertog and E. Monroy, *Near-infrared intersubband photodetection in GaN/AlN nanowires.* Nano Letters, 2017. **17**(11): p. 6954-6960.

10. N. Erhard, A. T. M. G. Sarwar, F. Yang, D. W. McComb, R. C. Myers and A. W. Holleitner, *Optical control of internal electric fields in band gap-graded InGaN nanowires.* Nano Letters, 2015. **15**(1): p. 332-338.

11. G. Pierre, *Metal organic vapour phase epitaxy of GaN and lateral overgrowth.* Reports on Progress in Physics, 2004. **67**(5): p. 667.

12. D. Cherns, S. J. Henley and F. A. Ponce, *Edge and screw dislocations as nonradiative centers in InGaN/GaN quantum well luminescence.* Applied Physics Letters, 2001. **78**(18): p. 2691-2693.

13. C. F. Johnston, M. J. Kappers and C. J. Humphreys, *Microstructural evolution of nonpolar (11-20) GaN grown on (1-102) sapphire using a 3D-2D method.* Journal of Applied Physics, 2009. **105**(7) : p. 073102.

14. Z. Liliental-Weber, J. Jasinski and D. Zakharov, *GaN grown in polar and non-polar directions.* OptoElectronics Review, 2004. **12**(4): p. 339.

15. H. Song, J. Suh, E. K. Kim, K. H. Baik and S.-M. Hwang, *Growth of high quality a-plane GaN epi-layer on r-plane sapphire substrates with optimization of multi-buffer layer.* Journal of crystal growth, 2010. **312**(21): p. 3122-3126.

16. M. Moram, C. Johnston, J. Hollander, M. Kappers and C. Humphreys, *Understanding x-ray diffraction of nonpolar gallium nitride films.* Journal of Applied Physics, 2009. **105**(11): p. 113501.

17. H. Zhong, A. Tyagi, N. N. Fellows, F. Wu, R. B. Chung, M. Saito, K. Fujito, J. S. Speck, S. P. DenBaars and S. Nakamura, *High power and high efficiency blue light emitting diode on freestanding semipolar (1011) bulk GaN substrate.* Applied Physics Letters, 2007. **90**(23): p. 233504.

18. Y. K. Ee, J. M. Biser, W. Cao, H. M. Chan, R. P. Vinci and N. Tansu, *Metalorganic vapor phase epitaxy of III-nitride light-emitting diodes on nanopatterned AGOG sapphire substrate by abbreviated growth mode.* IEEE Journal of Selected Topics in Quantum Electronics, 2009. **15**(4): p. 1066-1072.

19. K. Gurnett and T. Adams, *Native substrates for GaN: The plot thickens.* III-Vs Review, 2006. **19**(9): p. 39-41.

20. S. D. Hersee, A. K. Rishinaramangalam, M. N. Fairchild, L. Zhang and P. Varangis, *Threading defect elimination in GaN nanowires.* Journal of Materials Research, 2011. **26**(17): p. 2293-2298.

21. J. Cho, E. F. Schubert and J. K. Kim, *Efficiency droop in light-emitting diodes: Challenges and countermeasures.* Laser & Photonics Reviews, 2013. **7**(3): p. 408-421.

22. R. Koester, J. S. Hwang, D. Salomon, X. Chen, C. Bougerol, J. P. Barnes, D. L.

S. Dang, L. Rigutti, A. de Luna Bugallo and G. Jacopin, *M-plane core–shell InGaN/GaN multiple-quantum-wells on GaN wires for electroluminescent devices.* Nano Letters, 2011. **11**(11): p. 4839-4845.

23. J. Bai, Q. Wang and T. Wang, *Characterization of InGaN-based nanorod light emitting diodes with different indium compositions.* Journal of Applied Physics, 2012. **111**(11): p. 113103.

24. Q. Li, K. R. Westlake, M. H. Crawford, S. R. Lee, D. D. Koleske, J. J. Figiel, K. C. Cross, S. Fathololoumi, Z. Mi and G. T. Wang, *Optical performance of top-down fabricated InGaN/GaN nanorod light emitting diode arrays.* Optics Express, 2011. **19**(25): p. 25528-25534.

25. N. P. Reddy, N. Shagufta, M. Sudha, V. Kaushal, S. Naeem, K. Fouad, T. Hark Hoe and J. Chennupati, *Enhanced luminescence from GaN nanopillar arrays fabricated using a top-down process.* Nanotechnology, 2016. **27**(6): p. 065304.

26. C. H. Chang, L. Y. Chen, L. C. Huang, Y. T. Wang, T. C. Lu and J. J. Huang, *Effects of strains and defects on the internal quantum efficiency of InGaN/GaN nanorod light emitting diodes.* IEEE Journal of Quantum Electronics, 2012. **48**(4): p. 551-556.

27. L. Y. Chen, C. K. Li, J. Y. Tan, L. C. Huang, Y. R. Wu and J. J. Huang, *On the efficiency decrease of the GaN light-emitting nanorod arrays.* IEEE Journal of Quantum Electronics, 2013. **49**(2): p. 224-231.

28. L. Yang, C. S. Xue, C. M. Wang and H. X. Li, *Growth of GaN nanowires by ammoniating Ga_2O_3 thin films deposited on quartz with radio frequency magnetron sputtering.* Nanotechnology, 2003. **14**(1): p. 50-52.

29. C. S. Xue, Q. Q. Wei, Z. C. Sun, Z. H. Dong, H. B. Sun and L. W. Shi, *Fabrication of GaN nanowires by ammoniating Ga_2O_3/Al_2O_3 thin films deposited on Si(111) with radio frequency magnetron sputtering.* Nanotechnology, 2004. **15**(7): p. 724-726.

30. J. C. Wang, S. Q. Feng and D. P. Yu, *High-quality GaN nanowires synthesized using a CVD approach.* Applied Physics A: Materials Science & Processing, 2002. **75**(6): p. 691-693.

31. X. M. Cai, A. B. Djurisic and M. H. Me, *GaN nanowires: CVD synthesis and properties.* Thin Solid Films, 2006. **515**(3): p. 984-989.

32. R. Calarco, M. Marso, T. Richter, A. I. Aykanat, R. Meijers, A. v.d. Hart, T. Stoica and H. Lüth, *Size-dependent photoconductivity in MBE-grown GaN−nanowires.* Nano Letters, 2005. **5**(5): p. 981-984.

33. G. Tourbot, C. Bougerol, A. Grenier, M. Den Hertog, D. Sam-Giao, D. Cooper, P. Gilet, B. Gayral and B. Daudin, *Structural and optical properties of InGaN/GaN nanowire heterostructures grown by PA-MBE.* Nanotechnology, 2011. **22**(7): p. 075601.

34. Y. L. Chang, J. L. Wang, F. Li and Z. Mi, *High efficiency green, yellow, and*

amber emission from InGaN/GaN dot-in-a-wire heterostructures on Si(111). Applied Physics Letters, 2010. **96**(1): p. 013106.

35. H. P. T. Nguyen, M. Djavid, S. Y. Woo, X. Liu, A. T. Connie, S. Sadaf, Q. Wang, G. A. Botton, I. Shih and Z. Mi, *Engineering the carrier dynamics of InGaN nanowire white light-emitting diodes by distributed p-AlGaN electron blocking layers.* Scientific Reports, 2015. **5**(1): p. 1-7.

36. Y. W. Steffi, G. Nicolas, P. T. N. Hieu, M. Zetian and A. B. Gianluigi, *Interplay of strain and indium incorporation in InGaN/GaN dot-in-a-wire nanostructures by scanning transmission electron microscopy.* Nanotechnology, 2015. **26**(34): p. 344002.

37. S. R. Ryu, S. D. Gopal Ram, Y. H. Kwon, W. C. Yang, S. H. Kim, Y. D. Woo, S. H. Shin and T. W. Kang, *HVPE growth of self-aligned GaN nanorods on c-plane, a-plane, r-plane, and m-plane sapphire wafers.* Journal of Materials Science, 2015. **50**(19): p. 6260-6267.

38. Y. Cheng, H. Zong, J. Wu, P. Liu, T. Han, T. Yu, X. Hu and G. Zhang, *Exceptionally long GaN sub-micrometer rods grown by HVPE on a MOCVD-GaN rod template.* Journal of Alloys and Compounds, 2016. **688**: p. 967-971.

39. K. Lekhal, S. Y. Bae, H. J. Lee, T. Mitsunari, A. Tamura, M. Deki, Y. Honda and H. Amano, *Controlled morphology of regular GaN microrod arrays by selective area growth with HVPE.* Journal of Crystal Growth, 2016. **447**: p. 55-61.

40. J. P. Ahl, H. Behmenburg, C. Giesen, I. Regolin, W. Prost, F. J. Tegude, G. Z. Radnoczi, B. Pecz, H. Kalisch, R. H. Jansen and M. Heuken, *Gold catalyst initiated growth of GaN nanowires by MOCVD.* Physica Status Solidi C: Current Topics in Solid State Physics, 2011. **8**(7-8): p. 2315-2317.

41. K. Choi, M. Arita and Y. Arakawa, *Selective-area growth of thin GaN nanowires by MOCVD.* Journal of Crystal Growth, 2012. **357**: p. 58-61.

42. W. Bergbauer, M. Strassburg, K. Ch, N. Linder, C. Roder, A. Trampert, S. Li, H. Wehmann and A. Waag, *Continuous-flux MOVPE growth of position-controlled N-face GaN nanorods and embedded InGaN quantum wells.* Nanotechnology, 2010. **21**(30): p. 305201.

43. V. Dobrokhotov, D. N. McIlroy, M. G. Norton, A. Abuzir, W. J. Yeh, I. Stevenson, R. Pouy, J. Bochenek, M. Cartwright, L. Wang, J. Dawson, M. Beaux and C. Berven, *Principles and mechanisms of gas sensing by GaN nanowires functionalized with gold nanoparticles.* Journal of Applied Physics, 2006. **99**(10): p. 104302.

44. T. Y. Kim, S. H. Lee, Y. H. Mo, H. W. Shim, K. S. Nahm, E. K. Suh, J. W. Yang, K. Y. Lim and G. S. Park, *Growth of GaN nanowires on Si substrate using Ni catalyst in vertical chemical vapor deposition reactor.* Journal of Crystal Growth, 2003. **257**(1-2): p. 97-103.

45. X. Wang, S. Li, M. S. Mohajerani, J. Ledig, H. H. Wehmann, M. Mandl, M. Strassburg, U. Steegmüller, U. Jahn, J. Lähnemann, H. Riechert, I. Griffiths, D. Cherns and A. Waag, *Continuous-flow MOVPE of Ga-polar GaN column arrays and core–shell LED structures.* Crystal Growth & Design, 2013. **13**(8): p. 3475-3480.

46. J. Hartmann, X. Wang, H. Schuhmann, W. Dziony, L. Caccamo, J. Ledig, M. S. Mohajerani, T. Schimpke, M. Bähr, G. Lilienkamp, W. Daum, M. Seibt, M. Straßburg, H. H. Wehmann and A. Waag, *Growth mechanisms of GaN microrods for 3D core–shell LEDs: The influence of silane flow.* Physica Status Solidi A, 2015. **212**(12): p. 2830-2836.

47. G. Jacopin, A. D. Bugallo, P. Lavenus, L. Rigutti, F. H. Julien, L. F. Zagonel, M. Kociak, C. Durand, D. Salomon, X. J. Chen, J. Eymery and M. Tchernycheva, *Single-wire light-emitting diodes based on GaN wires containing both polar and nonpolar InGaN/GaN quantum wells.* Applied Physics Express, 2012. **5**(1): p. 014101.

48. C. Tessarek and S. Christiansen, *Self-catalyzed, vertically aligned GaN rod-structures by metal-organic vapor phase epitaxy.* Physica Status Solidi C, 2012. **9**(3-4): p. 596-600.

49. C. Tessarek, M. Bashouti, M. Heilmann, C. Dieker, I. Knoke, E. Spiecker and S. Christiansen, *Controlling morphology and optical properties of self-catalyzed, mask-free GaN rods and nanorods by metal-organic vapor phase epitaxy.* Journal of Applied Physics, 2013. **114**(14): p. 144304.

50. W. Xue, L. Shunfeng, F. Sönke, H. W. Hergo, S. Martin, L. Hans-Jürgen, S. Ulrich and W. Andreas, *Mechanism of nucleation and growth of catalyst-free self-organized GaN columns by MOVPE.* Journal of Physics D: Applied Physics, 2013. **46**(20): p. 205101.

51. R. Koester, J. S. Hwang, C. Durand, S. Dang Dle and J. Eymery, *Self-assembled growth of catalyst-free GaN wires by metal-organic vapour phase epitaxy.* Nanotechnology, 2010. **21**(1): p. 015602.

52. X. J. Chen, G. Perillat-Merceroz, D. Sam-Giao, C. Durand and J. Eymery, *Homoepitaxial growth of catalyst-free GaN wires on N-polar substrates.* Applied Physics Letters, 2010. **97**(15): p. 151909.

53. C. Tessarek, M. Heilmann, E. Butzen, A. Haab, H. Hardtdegen, C. Dieker, E. Spiecker and S. Christiansen, *The role of Si during the growth of GaN micro- and nanorods.* Crystal Growth & Design, 2014. **14**(3): p. 1486-1492.

54. V. Neplokh, A. Messanvi, H. Zhang, F. H. Julien, A. Babichev, J. Eymery, C. Durand and M. Tchernycheva, *Substrate-free InGaN/GaN nanowire light-emitting diodes.* Nanoscale research letters, 2015. **10**(1): p. 1-6.

55. X. Wang, S. Li, S. Fündling, J. Wei, M. Erenburg, H.-H. Wehmann, A. Waag, W. Bergbauer, M. Strassburg, U. Jahn and H. Riechert, *Polarity control in 3D GaN structures grown by selective area MOVPE.* Crystal Growth & Design,

2012. **12**(5): p. 2552-2556.

56. H. Lu, D. Cao, X. Xiu, Z. Xie, R. Zhang, Y. Zheng and Z. Li, *Schottky rectifiers fabricated on bulk GaN substrate analyzed by electron-beam induced current technique.* Solid-State Electronics, 2008. **52**(5): p. 817-823.

57. O. Toshio and A. Masaharu, *Mechanism of yellow luminescence in GaN.* Japanese Journal of Applied Physics, 1980. **19**(12): p. 2395.

58. P. Huang, H. Zong, J. J. Shi, M. Zhang, X. H. Jiang, H. X. Zhong, Y. M. Ding, Y. P. He, J. Lu and X. D. Hu, *Origin of 3.45 eV emission line and yellow luminescence band in GaN nanowires: Surface microwire and defect.* ACS Nano, 2015. **9**(9): p. 9276-9283.

59. J. Neugebauer and C. G. Van de Walle, *Gallium vacancies and the yellow luminescence in GaN.* Applied Physics Letters, 1996. **69**(4): p. 503-505.

60. B. Liu, F. Yuan, B. Dierre, T. Sekiguchi, S. Zhang, Y. Xu and X. Jiang, *Origin of yellow-band emission in epitaxially grown GaN nanowire arrays.* ACS Applied Materials & Interfaces, 2014. **6**(16): p. 14159-14166.

61. P. M. Coulon, B. Alloing, V. Brändli, P. Vennéguès, M. Leroux and J. Zúñiga-Pérez, *Dislocation filtering and polarity in the selective area growth of GaN nanowires by continuous-flow metal organic vapor phase epitaxy.* Applied Physics Express, 2016. **9**(1): p. 015502.

62. R. Colby, Z. Liang and I. H. Wildeson, *Dislocation filtering in GaN nanostructures.* Nano Letters, 2010. **10**(5): p. 1568-1573.

Chapter 2

Background and experimental techniques

2.1 Introduction

In this chapter, we introduce the background and experimental methods for GaN nanorod growth and characterization. The chapter is arranged as follows: section 2.2 discusses the basic properties of GaN nanorods including their crystal structure, synthesis methods, polarity, optical properties, and application in LEDs. In section 2.3, we describe the epitaxial growth using metalorganic chemical vapour deposition (MOCVD), and various characterisation techniques used in this thesis, including scanning electron microscope (SEM), transmission electron microscope (TEM), scanning transmission electron microscope (STEM), cathodoluminescence (CL), focused ion-beam (FIB), and nanoscale secondary ion mass spectrometry (nano-SIMS).

2.2 Backgrounds

2.2.1 Crystal structure and polarity of III-nitride material

For III-nitride materials, there are mainly two phases: wurtzite (figure 2.1 a) and zinc-blende (figure 2.1 b). Wurtzite GaN is the thermodynamically stable phase with a hexagonal crystal structure. GaN grown by MOCVD system is mainly wurtzite in structure, while pure zinc-blende structure requires special growth conditions. The zinc-blende structure is the metastable phase with a cubic crystal structure. The two phases have differences in crystal symmetry, bandgap, impurity incorporation rate, etc [1]. The wurtzite and zinc-blende structures both have tetrahedral coordination, but their stacking sequences are different. The stacking sequence of wurtzite structure is …AaBbAaBb…along the c-axis (figure 2.1 c) while the stacking sequence of zinc-blende structure is …AaBbCcAaBbCc… (figure 2.1 d). The upper and lower case

letters stand for group III and nitrogen atoms, respectively.

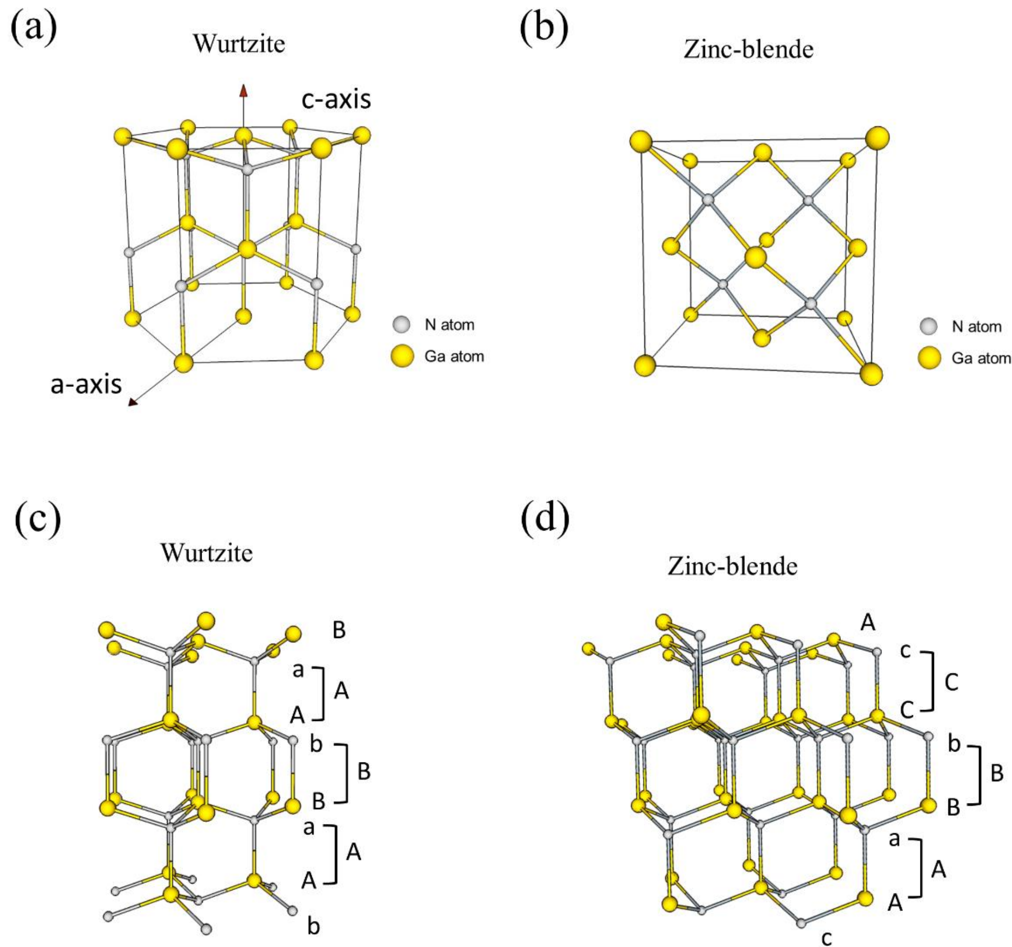

Figure 2.1 Schematic drawing of GaN crystal structure: (a) wurtzite and (b) zinc-blende phase. Layer sequence and the corresponding 3D presentation of (c) wurtzite and (d) zinc-blende structure.

Table 2.1 Material properties of GaN, AlN, InN, and sapphire [2].

Crystal properties	GaN	AlN	InN	a-Al_2O_3
Lattice constant (Å) a	3.189	3.112	3.548	4.758
Lattice constant (Å) c	5.185	4.982	5.760	12.991
Lattice constant (Å) c/a	1.625	1.600	1.623	2.730
Density (g/cm^3)	6.99	6.10	3.26	3.97
Thermal expansion coefficient (10^{-6}/℃) a	5.7	5.59	4.20	7.90-8.30
Thermal expansion coefficient (10^{-6}/℃) c	3.70	3.17	5.30	8.80-9.00

The lattice parameters and thermal expansion coefficients of GaN, AlN, InN, and

sapphire are shown in table 2.1. Although the lattice and thermal mismatch between III-nitrides and the sapphire substrate would lead to high dislocation density and cracking of the epitaxially grown film, the sapphire substrate is still widely used in GaN growth due to its high thermal stability, low cost, and high optical transparency.

Due to the non-centro symmetry of the wurtzite crystal structure, there exist two polarities along the [0001] direction (figure 2.2): Ga-polar [0001] and N-polar [000-1]. Apart from the polar planes, other planes also exist such as non-polar planes and semi-polar planes. The polarity would significantly affect the surface energy, which leads to diverse properties in dopant incorporation, surface reactivity, and thermal stability [3, 4].

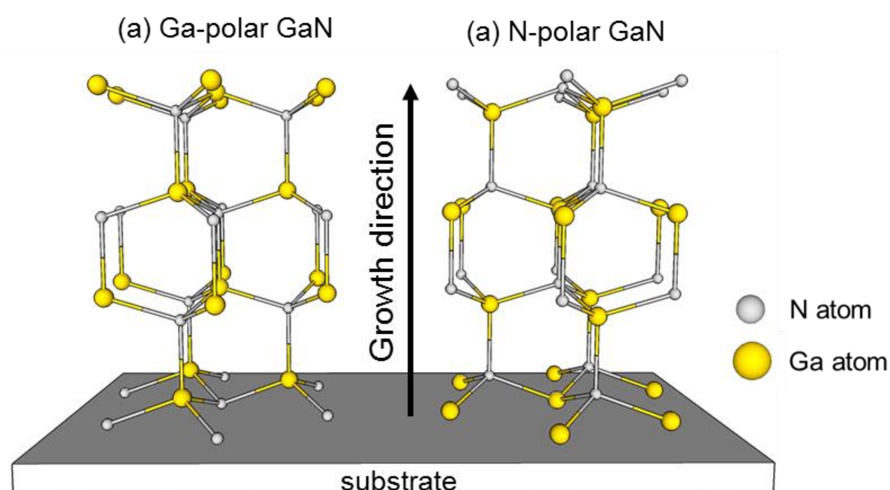

Figure 2.2 Schematic drawing of Ga-polar and N-polar GaN**.**

For traditional MOCVD growth, typically Ga-polar films are achieved, while specific growth conditions are needed to obtain N-polar films [4]. The selection of polarity is related to the nitridation process and buffer layer growth [5, 6]. An adequate nitridation and GaN low-temperature buffer are needed to achieve Ga-polar films [7]. For GaN nanorod growth, the small footprint makes it is more sensitive to polarity change [8, 9] and may lead to different morphology and optical properties. Several methods are used to determine the polarity of GaN, such as convergent beam electron diffraction (CBED) [10], electron energy loss spectroscopy (EELS) [11], X-ray photoelectron spectroscopic study [12], sensitive etching (KOH solution continuous etches N-polar GaN) [13], piezo-response force microscopy and aberration-corrected STEM measurements to directly image the group III and N atomic columns [14]. In this thesis, we used aberration-corrected STEM that will be discussed in 2.3.7 of this chapter.

2.2.2 Bottom-up GaN nanorod synthesis approach

2.2.2.1 Catalyst-assisted growth

The catalyst-assisted growth uses metal particles as catalyst to initiate growth. Depending on whether the catalysts are liquid or solid, growth could occur in either the vapour-liquid- solid (VLS) [15, 16] or vapor-solid-solid (VSS) growth modes [17]. For VLS growth (figure 2.3), radicals pyrolyzed from the vapour-phase precursors would either incorporate through the boundary of the particle-nanowire interface (triple-phase boundary) [15] or directly be absorbed into the droplet [16]. When the metal droplet becomes supersaturated, the nanorod would crystallize at the liquid-solid interface and grow along the main axis (axially). Other surrounding adatoms on the substrate can also diffuse along the nanorod and contribute to both axial and radial growth, resulting in a highly anisotropic 1D structure.

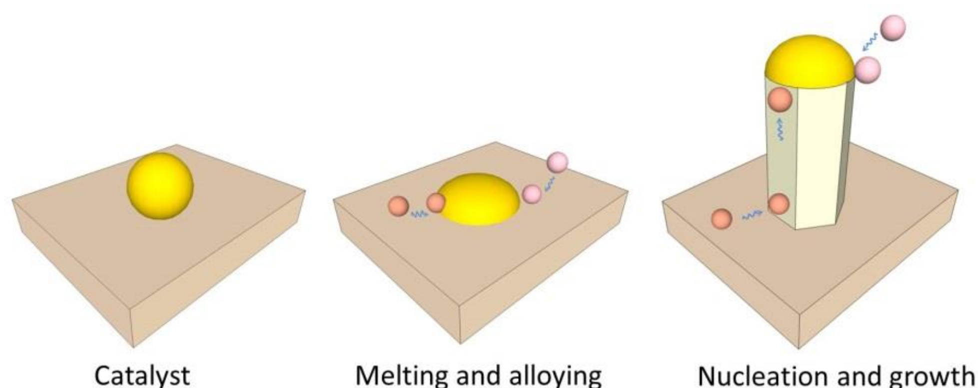

Figure 2.3 Schematic illustration of catalyst-assisted nanorod growth.

The first VLS growth of GaN nanorods was reported by Lieber's group [18] in the year 2000 using laser ablation and Fe catalyst. Other typical metal species used for GaN nanorod growth include Au [19, 20], Ni [21], and Al [22]. Depending on catalyst material composition, substrate, and growth conditions, nanorods can show variations in growth orientation, morphology, structural, electrical, and optical properties. For example, Kuykendall *et al.* [22] found that by changing the composition of the Ni-Au alloy catalyst, the nanorod growth direction could be altered from the $<1\bar{1}00>$ to $<11\bar{2}0>$ direction. Different combinations of catalysts and substrates can also change nanorod morphology. For instance, Au-seeded GaN nanorods grown on MgO substrate show hexagonal cross-sections [23], while Ni-seeded GaN nanorods grown on (100) γ-$LiAlO_2$ have triangular cross-sections [24]. Moreover, Zhou *et al.* [25] found nanorods grown using different catalyst differed in growth rates and optical properties. They

found the Ni-seeded nanorods grow faster without basal plane stacking faults (BSF), while Au-seeded nanorods contained BSF and their bandgap was blue-shifted [25]. This phenomenon was attributed to changes in supersaturation and surface energies in different types of seed particles.

The catalyst-assisted approach is simple and does not require complex fabrication facilities. However, the use of the metal catalyst could be detrimental for device applications. Additionally, the metal catalyst can also promote impurity incorporation and defects such as stacking faults, which could degrade the nanorod properties [26, 27]. Nevertheless, due to its simplicity, this approach is still attractive and provides a valuable platform for studying the fundamental growth mechanisms of nanorods.

2.2.2.2 Selective-area epitaxy

As mentioned above, there are many limitations in catalyst assisted-growth and hence, the catalyst-free approach was investigated as an alternative. Based on whether a dielectric mask is used or not, the catalyst-free approach can be categorized into selective-area epitaxy (SAE) and self-assembled growth.

In the SAE approach (figure 2.4), a patterned mask on the substrate or buffer layer/substrate is used to control the growth kinetics and form the nucleation sites to obtain uniform nanowire arrays. Selective area growths of GaN nanorods have been achieved on various substrates such as sapphire [28], GaN templates grown on sapphire [29], Si (111) [30] and SiC [31]. SiN_x [31] and SiO_x layers [29, 30] have been used as the mask. SAE grown GaN nanorods were first reported by Hersee *et al.* [31] using a pulsed mode in an MOCVD system. As illustrated in figure 2.5 (a), the pulsed mode is a growth method that alternately injects group III and group V precursors into the growth chamber, in a similar fashion as atomic layer deposition. Hersee *et al.* [31] have found that under a high V/III ratio (1500), continuous mode (figure 2.5 *b*) would lead to a lateral 2D growth, so they adopted a pulsed injection sequence of trimethylgallium (TMG), ammonia (NH_3) to achieve rapid and uniform nanorod array growth.

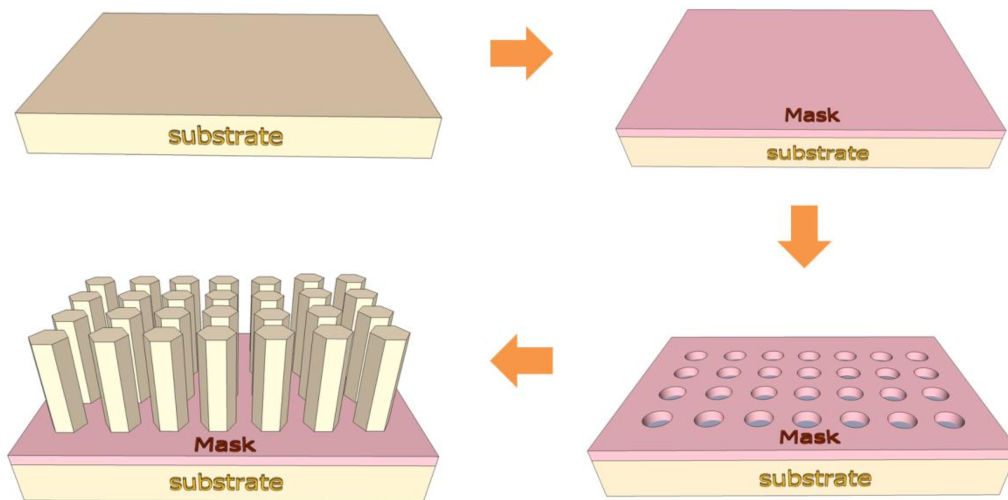

Figure 2.4 Schematic drawings of selected area epitaxy of nanorods.

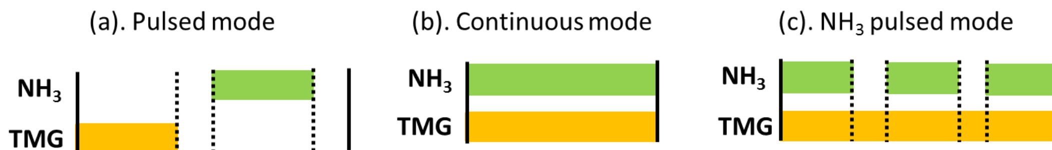

Figure 2.5 Illustrations of different growth modes used in SAE growth of GaN nanorods.

The reason for pulsing the precursors is to overcome the hydrogen passivation effect in GaN [32, 33]. As shown in figure 2.6 (b) and (c), the semi-polar planes in N-polar crystals are not passivated by hydrogen and can transform into non-polar planes through hydrogen etching effects, therefore forming into a nanorod morphology. However, in Ga-polar crystals, their semi-polar planes can be passivated by hydrogen [34-36] (figure 2.6 *a*). A continuous supply of precursors would keep the semi-polar planes and the slow growth rate of these planes [37] would lead to pyramid formation [32].

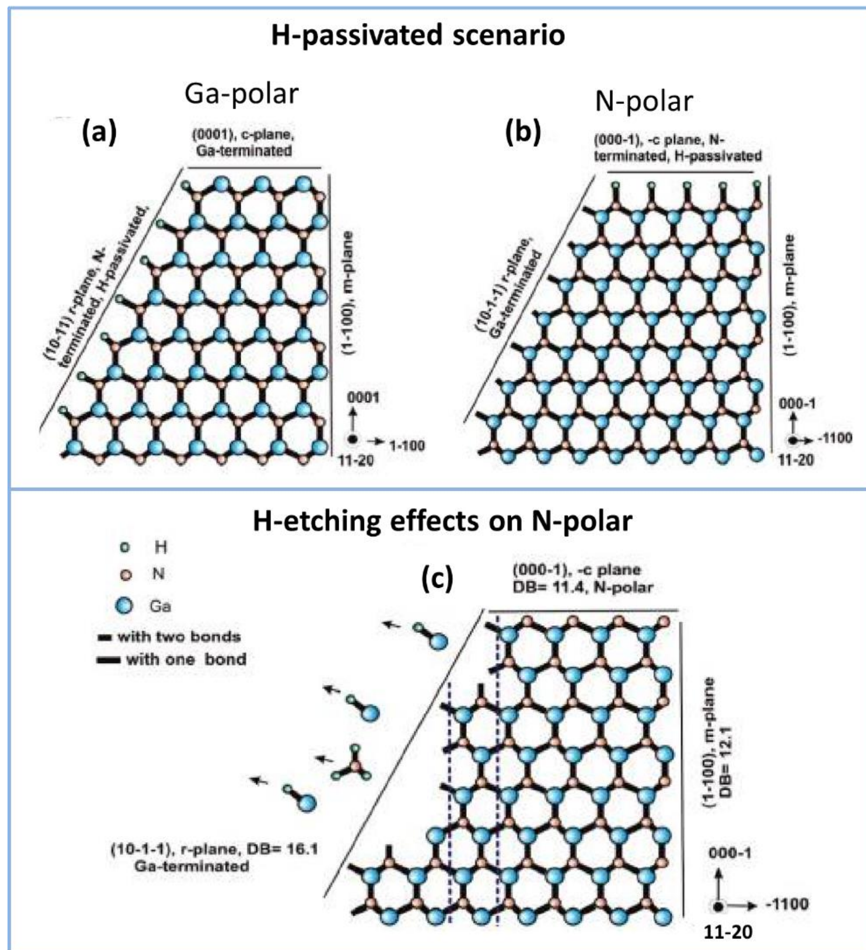

Figure 2.6 H-passivation effects on Ga-polar and N-polar GaN: (a, b) H-passivation effect on Ga polar and N-polar nanorod, respectively [32]. (c) semi-polar planes of the N-polar GaN structure etched by hydrogen (adapted from [32]).

To overcome this problem, in the pulsed mode, a pause step without any precursor supply is introduced to reduce the hydrogen passivation effects [33]. During the pause, residual precursors are flushed out of the reactor to enable H_2 etching on the semi-polar planes and also minimise the simultaneous presence of Ga and N atoms to reduce lateral growth [33]. As shown in figure 2.7 (b), by adjusting the precursor injection and pause times, lateral growth can be suppressed and the rod-like morphology is achieved.

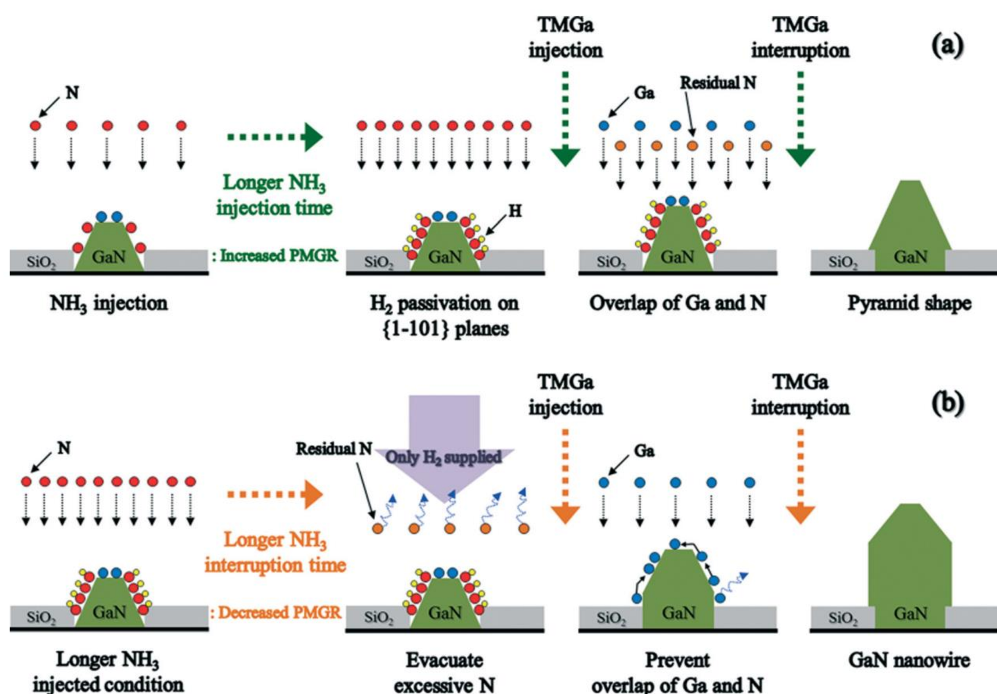

Figure 2.7 Schematic model for pulsed mode demonstrating the effect of NH3 interruption (adapted from [33]): (a) NH3 injection leading to H-passivation and the overlap of Ga and N to form a pyramidal shape. (b) NH3 interruption-leading to a rod-like morphology.

The pulsed mode requires a complicated sequence and combination of precursor pulsing and pause times to achieve optimum rod-like growth. To simplify the growth process, a continuous mode (figure 2.5 b) was proposed by Choi *et al*. [29] using extremely low precursor flow rates and V/III ratio (two orders of magnitude lower than V/III ratio used in typical GaN thin film growth). Nanorods with small diameters of ~50 nm were achieved through this method. However, the nanorod morphology is largely affected by mask opening size and larger diameter openings (400 nm) lead to lateral expansion [29]. Therefore, to achieve nanorods with small diameters, this method requires more complicated processes during mask preparation.

A method combining the advantages of pulsed and continuous mode [38] was proposed by Lin *et al.* [38], in which only NH_3 is pulsed during the growth. This NH_3 pulsed mode (figure 2.5 *c*) is simpler compared with standard pulsed mode and is more tolerant to the size of mask openings. The nanorods synthesised by this method also shows better optical properties with strong suppression of yellow luminescence (YL).

Through SAE growth, nanorod arrays with uniform diameter and pitch sizes have been achieved [39, 40]. However, this type of growth is highly dependent on the mask quality, and also mask fabrication is usually carried out by electron beam lithography

which is complicated and time-consuming.

2.2.2.3 Self-assembled growth

Self-assembled growth is a mask-free approach and was first used for GaN nanorod growth in a molecular beam epitaxy (MBE) system on Si (111) substrate [41] and sapphire (0001) substrate [42]. Later, it is also realised by MOCVD [43] and halide vapour phase epitaxy (HVPE) [44].

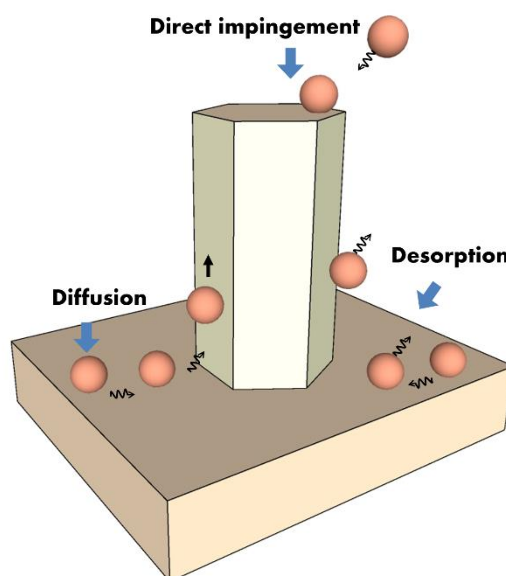

Figure 2.8 Schematic drawing illustrating the various processes occurring during self-assembled nanowire growth.

As shown in figure 2.8, a diffusion induced growth model is proposed in MBE growth [45-47]. The nanorods are grown under high temperature, high V/III ratio growth conditions, which could promote differential surface diffusion rates on the top and sidewall facets of the nanorods to achieve vertical growth [48]. Debnath *et al.* [45] found the top surface may act as an efficient collector of adatoms due to its lower chemical potential compared with other surfaces of the nanorods. The incoming atoms could be incorporated into the nanorod through direct impingement at the top of the nanorod. In addition, the adatoms arriving in regions between nanorods could diffuse towards the nearest nanorod and migrate along its sidewalls and be incorporated either on the sidewalls or at the top depending on the diffusion length of the adatoms. Direct impingement dominates in short and thick nanorods while in thin rods with a high aspect ratio, the adatom diffusion mechanism is more dominant [45].

MBE lacks large-scale productivity due to its slow growth rate and the high expenses

of maintaining the ultra-high vacuum growth conditions. In contrast, Koester *et al.* [43] reported a self-assembled growth method for high-speed growth of GaN nanorods on sapphire (0001) substrates via silane-assisted growth in MOCVD system. Their growth process could be divided into three steps: (i) Formation of a SiN_x mask by injecting silane and ammonia simultaneously. The function of the SiN_x mask is to restrain the nanorod growth within its openings; (ii) GaN nucleation without silane; (iii) Vertical nanorod growth with high silane injection. They found that the essential parameters to achieve nanorod growth are nucleation time, high silane injection and small V/III ratio [43]. Compared with the self-assembled growth in MBE without silane, the silane-assisted MOCVD growth has the advantages of wafer-scale productivity, uniform density (10^7 rods cm^{-2}) and extremely high growth rate (tens micrometer per hour) [43].

Later, self-assembled growth was also realised by other groups [49-51] with slightly different growth parameters and steps, but all of these reports show that silane is key in promoting vertical growth. The role of silane was clarified by Tessarek *et al.* [52] where it would lead to the formation of SiN_x on nanorod sidewalls and substrate. The SiN_x layer on the sidewalls could prevent lateral growth and etching of the sidewalls. In addition, it enhances adatom mobility and increases the growth rate of the nanorods [52].

The impacts of other growth parameters have also been investigated, including V/III ratio nucleation/growth temperature [51], nucleation/growth duration [50], precursor flow rate [50], chamber pressure [49] and carrier gas mix ratio (H_2/N_2) [49]. Although the optimum growth conditions can vary from chamber to chamber, by and large, the growth window for GaN nanorods grown by this technique are [43, 49-51]: (i) growth temperature: 1000-1150 °C; (ii) V/III ratio: 6-48 with very low NH_3 flow rate; (iii) high silane injection: 200-536 nmol/min. Xue *et al.* [51] showed that under certain growth conditions, self-assembled nanorod growth is limited by direct impingement on the top of the nanorod rather than the surface diffusion process. Mixed polarity has been found in some of their nanorods which have a Ga-polar core but covered by an N-polar shell [51]. Chen *et al.* [10] found that a low V/III ratio was necessary and using a high V/III ratio would lead to lateral coalescence of nanorods even under high silane injection. They also linked the morphology of pyramidal tops to Ga-polarity and flat tops to N-polarity based on CBED results [10].

The self-assembled approach of growing GaN nanorods is not only demonstrated on

sapphire substrates but also on graphene covered sapphire [53] and graphene covered Si (111) and (100) substrates [54]. Heilmann *et al.* [54] claimed the graphene layer can also act as a substrate and a chemically inert buffer to integrate the GaN nanorods onto any other substrates that can sustain the high growth temperature required for GaN nanorods. Multi-quantum well (MQW) structures grown on nanorods have also been reported [55, 56] and optoelectronic devices based on these structures have been realized, such as single nanorod LEDs [57], single nanorod photodetectors [56], and substrate-free nanorod array LEDs [58, 59].

In summary, the self-assembled approach is totally foreign-catalyst free and does not require complicate substrate preparation or mask fabrication process. It could be used for wafer-scale growth and transfer to other novel substrates. These advantages have made it an attractive approach for the nano-device applications that do not need precise positioning of the nanorods.

2.2.3 Point defects in GaN

Point defects are prevalent in III-nitrides, and they have fundamental effects on material properties [60]. Based on their chemical origins, point defects can be roughly divided into extrinsic defects, such as dopants and impurities, and native defects such as vacancies and interstitials.

2.2.3.1 Extrinsic point defects

Extrinsic defects include dopants that provide donors/acceptors to control conductivity and unwanted deep levels that act as traps and non-radiative recombination centers. In this section, we would briefly review the conventional dopants (Si, Mg) and several impurity elements (C, O, and H).

For silicon, it could be introduced into GaN as Si_{Ga} donor or Si_N acceptor. However, the Si_N is considered as unfavourable due to its large atomic size and high formation energy [61]. A heavy Si doping is used in n-type GaN to increase the carrier concentration and minimize Ohmic resistance. A carrier concentration limit around 1-2 $\times10^{19}$ cm^{-3} has been reported [62], which means over this limit, the material quality would be degraded. Excess Si would cause a large tensile strain, which gives rise to dislocations, surface roughening, and wafer cracking [63-65]. These defects may also act as nucleation sites for Si segregation and a second condensed phase formation [60].

Magnesium as a p-type dopant in GaN is introduced as Mg_{Ga} with a binding energy

of 224 meV [66]. The Mg_{Ga} acceptor is considered to have a sharp acceptor-bound excitons emission at 3.466 eV [67], donor-acceptor pair emission at 3.27 eV [67], and may also be related to a broad blue luminescence at 2.9 eV. The ionization energy for Mg_{Ga} is around 110-190 meV [68-70] depending on its doping concentration. Such high ionization energy would lead to a relatively low percentage of ionized acceptors under room temperature. Researchers have found a high Mg doping level above 1×10^{19} cm^{-3} would lead to defect-related hole compensation and also a decrease in conductivity [60].

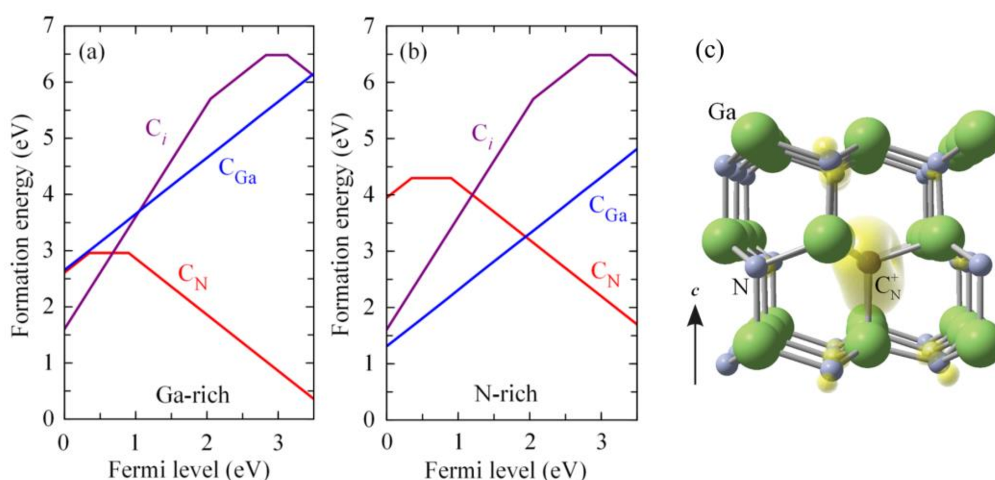

Figure 2.9 Formation energy of carbon-related point defects and schematic illustration of CN^+ in GaN: (a, b) Formation energy versus Fermi level for C_{Ga}, C_N, and C_i in GaN under Ga-rich and N-rich conditions, respectively (adapted from [71]). (c) Structure and spin density associated with CN^+ in GaN (adapted from [71]).

Carbon is introduced into the MOCVD through metalorganic precursors and can exist as an impurity in GaN. C is considered to be a source for yellow luminescence (YL) [72-74] and could be introduced as C_{Ga} donor, C_N acceptor, and C_i interstitial. For C_N, it has been linked with YL in many reports [71, 75, 76]. In undoped or n-doped GaN, C_N is considered as the most stable charge state. Christenson *et al.* [76] predicted C_N peaks at 2.18 eV with zero phonon line (ZPL) at 2.67 eV, which agrees well with the YL emission. Some reports [77-79] argued C_N–O_N complex with a transition level at 0.75 eV above the valance band as the primary source for YL in C-doped GaN. However, other studies pointed out C_N–O_N complex is not stable, and most recent calculation results show rather than C_N–O_N complex, the YL is related to isolated C_N defects [60].

For other forms of C incorporation, such as C_i, it has been reported to have high

formation energy [71] and occurs when the Femi level is near the valence band maximum. Density functional theory (DFT) calculations have shown C_{Ga} is introduced in GaN as a shallow donor and stable in the positive charge states across the bandgap [71]. However, C_{Ga} possesses the lowest formation energy only at N-rich growth conditions [71], and C_{Ga} is not the most favoured in undoped and n-doped GaN.

Oxygen as an abundant element in the environment can incorporate into GaN as a shallow O_N donor. The binding energy of O_N is 33.5 meV [61], and controlling isolated O_N concentration is difficult since O_N tends to form stable complexes with intrinsic point defects such as V_{Ga}.

Hydrogen is easily introduced into GaN as an interstitial (H_i) during growth or processing. It forms deep acceptor H_i^- and deep donor H_i^+ in n-type and p-type GaN, respectively [80]. H_i^+ has lower formation energy in p-type GaN, and Mg doping is enhanced in the presence of H_i^+[81]. H_i^+ donor can bond with Mg_{Ga} acceptor to form into a stable complex Mg-H complex with a binding energy of 1.02 eV [82]. The Mg-H complex would inactivate the Mg acceptor and reduces the free hole concentration in Mg-doped GaN [82]. Procedures such as anneal after the growth is introduced to reduce the passivation and reactive the acceptors [83].

2.2.3.2 Intrinsic point defects

The intrinsic point defects in GaN include vacancies (V_{Ga}, V_N), interstitials (Ga_i, N_i), antisites (Ga_N, N_{Ga}), and complexes like V_{Ga}-V_N, Ga_N-V_{Ga}, and N_{Ga}-V_N. To identify the nature of native defects, comparisons between the results of optical experiments such as photoluminescence (PL), Raman spectroscopy with the first-principle calculations and other supporting experiments are necessary.

Vacancies have the lowest formation energy among the native defects and exist with substantial concentrations in GaN. V_N is one of the most stable native defects for a large range of Fermi levels, but the high formation energy close to the conduction band minimum (CBM) makes it unlikely to form in n-doped and unintentional doped GaN [84, 85]. V_N can exist in p-type GaN with an optical signature visible in PL, and it is suggested as a source of green and yellow luminescence (YL) in p-type GaN [86]. Yan *et al.* [87] predict the recombination of a hole from V_N^{3+} with an electron from the CBM

emits at 2.18 eV with ZPL at 2.99 eV.

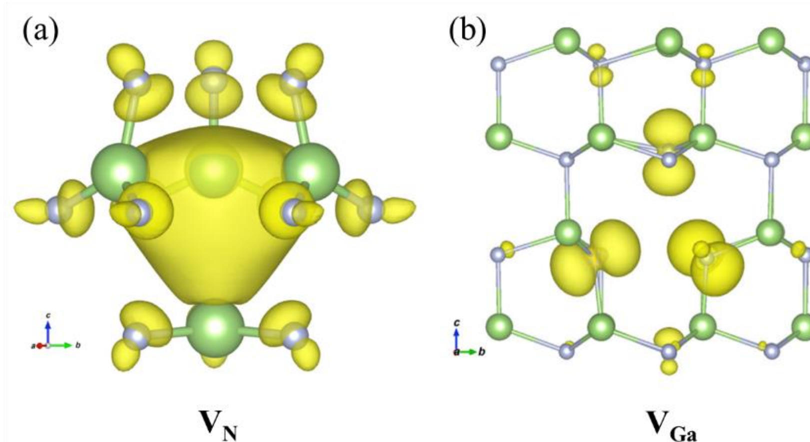

Figure 2.10 Charge density of the localized defect state of V_N and V_{Ga}. (a) V_N calculated in the 3+ charge state. (b) V_{Ga} in 3- charge state (adapted from [85]).

Ga vacancy possesses the lowest energy among all the native defects in n-type GaN. Ga vacancy has long been considered as a source of YL through experimental results in combination with positron annihilation spectroscopy (PAS) [61]. In recent DFT simulations, Lyons *et al.* [88] predict the capture of a hole from the valence band maximum to V_{Ga}^{3-} emits at 2.27 eV with ZPL at 2.8 eV, matching the YL emission position. Diallo *et al.* [85] have predicted another possible recombination process where isolated V_{Ga} emission peaks at 0.6 eV with ZPL at 1.4 eV, which is likely to be a non-radiative defect [85].

Interstitial and antisite defects are less favourable due to their high formation energy [60] and could be generated under non-equilibrium conditions, such as ion implantation or electron irradiation [89-91]. According to the latest hybrid functional calculations, the most stable configuration of N interstitial is in the form of N-N bond with an N host atom [85]. N_i is recently observed by electronic paramagnetic resonance, and electron-nuclear double resonance experiments in electron irradiated n-type GaN [92]. The most stable configuration for Ga interstitial, G_i is the one that exists alongside a Ga atom near the octahedral site along the c-axis of the crystal. G_i acts as a compensating center in p-type GaN and has been identified in electron irradiated GaN through electronic paramagnetic resonance [93]. N antisites have the highest formation energy among the native defects and unlikely to be formed in both n-type and p-type GaN. Ga antisites have lower formation at Fermi level close to the conduction band minimum (CBM) compared with Ga interstitials, and Ga antisites are the dominant native point defects

in n-type GaN, excluding vacancy-related defects.

2.2.4 Optical properties of GaN

For semiconductors, luminescence could be divided into two types: intrinsic emission and extrinsic emission (characteristic emission). Intrinsic emission is due to the recombination of electrons and holes at the energy bandgap, which is also known as fundamental emission. When the conduction band minimum and valence band maximum are at the same wave vector value **k** (as shown in figure 2.11 *a*), the semiconductor has a direct bandgap (such as in GaN and GaAs). In this process, the recombination of electron-hole would emit a photon whose value equals to the bandgap energy E_g, which would be affected by doping concentration, crystal structure, temperature and etc. [94]. If the extrema of both bands not at the same **k** (figure 2.11 *b*), the electron-hole recombination could emit a phonon, then the semiconductor has an indirect bandgap (such as in Si and GaP). Because of the necessity for extra phonon participation, the emission probability of indirect bandgap semiconductor is orders of magnitude lower than that of a direct bandgap semiconductor.

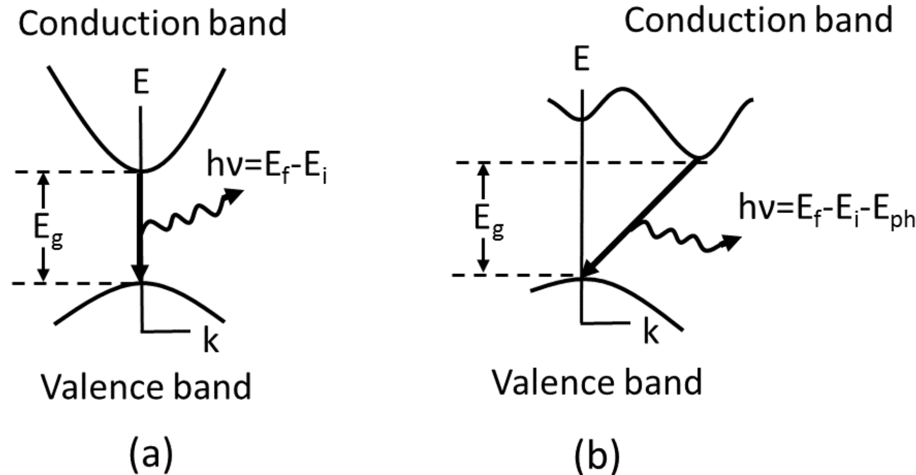

Figure 2.11 The energy transition between initial states E_i and final states E_f for (a) direct bandgap semiconductor, (b) indirect bandgap semiconductor. The transition in indirect bandgap requires the participation of a phonon.

At low temperatures, electron-hole pairs can form a bound state, known as the exciton. The recombination energy of the exciton states approximately corresponds to the energy bandgap, which belongs to intrinsic emission also known as 'near-band-emission' (NBE). The various types of radiative transitions in the semiconductor are shown in figure 2.12 [94]. In process 1, an excited electron relaxes from an excited state, which may be accompanied by phonon-assisted photon emission. In process 2, an electron directly recombines with a hole, accompanied by the emission of a photon (energy approximately equal to Eg). Process 3 describes free or impurities bound excitons decay. The impurities bound with exciton could be neutral/ionized donor $D^{\circ}X/D^{+}X$, neutral /ionized acceptor $A^{\circ}X/A^{-}X$. Processes 4 to 6 are extrinsic emission related to impurities states: process 4 is a donor to free hole transition (D°h), process 5 is free electron to acceptor transition (eA°), and process 6 is donor-acceptor pair (DAP) recombination.

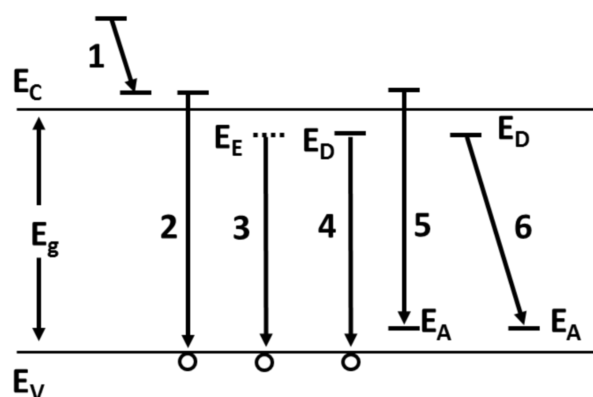

Figure 2.12 Schematic drawing of the radiative energy transition in the semiconductor: E_C (conduction band), E_V (valence band), E_E (exciton), E_D (donor level), E_A (acceptor level).

A typical emission spectrum at the liquid N_2 temperature of a GaN nanorod is shown in figure 2.13. The near band emission is centred around 3.4 eV and the broad peak at 2.2 eV is the yellow luminescence. The origin of yellow luminescence is commonly believed due to the Ga vacancy or carbon incorporation [77]. The carbon source comes

from the metalorganic precursors used for growth and/or chamber environment.

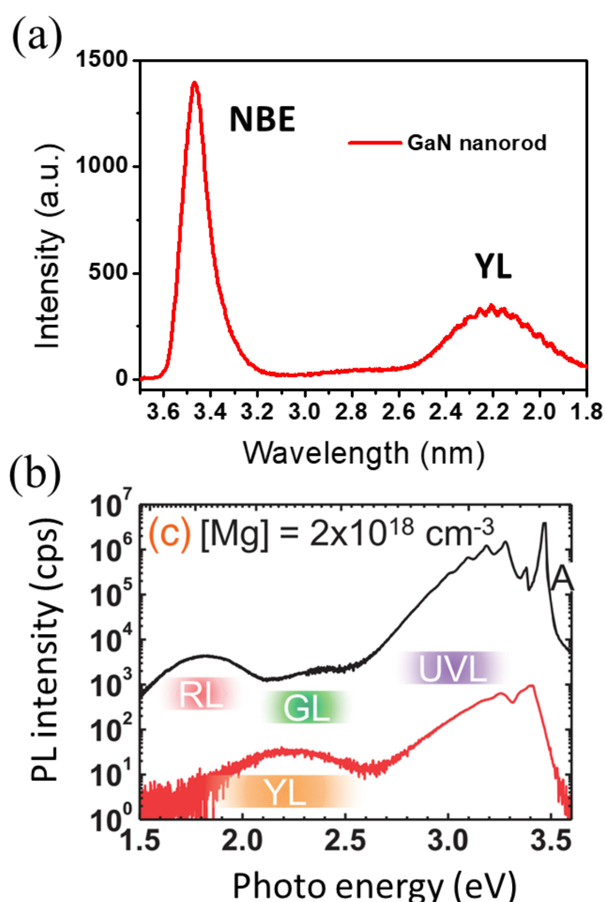

Figure 2.13 Typical optical emission peaks of GaN. (a) A typical CL spectrum of GaN nanorod taken at liquid N_2 temperature. (b) PL spectra of Mg-doped GaN epilayers with Mg-doping level of 2×10^{18} under 300 K (adapted from [95]).

Other types of defect-related luminescence also exist such as red luminescence (peaked around 1.8 eV), green luminescence (peaked around 2.5 eV), and blue luminescence (peaked around 2.9 eV). Figure 2.13 (b) shows the distribution of red, green, and yellow luminescence in an Mg-doped GaN epilayer [95]. Green luminescence in the Mg-doped sample has been attributed to point defects such as nitrogen vacancies. Blue luminescence in Mg-doped GaN layers has been studied by Kwon *et al.* [96] where they relate it to a shallow Mg acceptor or a complex composed of Mg acceptor and nitrogen vacancy.

2.2.5 GaN nanorod LEDs

LED is one of the most important applications for GaN and related nitride materials. GaN-based LEDs could have efficiency as high as 300 lm/W, which is more efficient

than traditional incandescent and fluorescent lamps that only offer efficiencies of 15-100 lm/W. In conventional planar GaN-based LED, there is an emission efficiency droop at longer wavelengths, which leads to a ‘green-yellow gap’ at 550 to 590 nm, which coincides with the highest human eye spectral response. This droop is attributed to a large lattice mismatch in $In_xGa_{1-x}N$/GaN structure and piezoelectric field for materials grown on c-plane (polar plane). This piezoelectric field in $In_xGa_{1-x}N$ quantum well leads to spatial separation of holes and electron wave-functions, which lowers the carrier recombination efficiency. To prevent the strain built up and higher dislocation density in thicker quantum wells, thin quantum wells with thickness around 2-4 nm are used [97]. However, thin quantum wells also lead to the efficiency droop at high carrier densities.

To overcome the limitations in GaN-based planar LEDs, GaN nanorod LED was proposed with various advantages [58, 98]: (i) improved carrier recombination efficiency on non-planar quantum-confined Stark effect (QCSE)-free sidewalls, (ii) superior crystal quality due to dislocation bending and spatial filtering, (iii) thicker InGaN MQWs with higher In content are possible on the sidewalls to span a wider wavelength range, (iv) improved light extraction efficiency due to natural geometry of the nanorod, and (v) the ability to fabricate single nanorod device and integration with silicon photonics circuit.

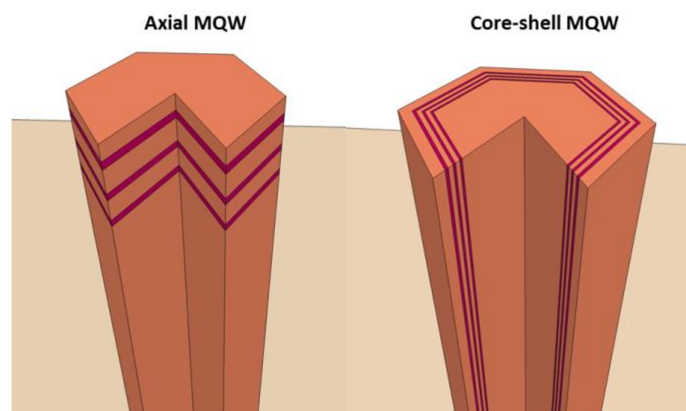

Figure 2.14 Schematic drawing of GaN-InGaN MQW structure: axial MQW (left) and core-shell MQW (right).

GaN nanorod LEDs could be divided into two types based on their geometries: one is a core-shell type (figure 2.14 right) with MQWs covering the whole nanorod as a shell while the other is axial configuration (figure 2.14 left) where the MQWs are

stacked the same orientation as the nanorod growth direction.

The core-shell geometry provides larger surface areas that fully utilize the advantage of nanorod geometry. This type of structure is mostly grown by MOCVD, and many groups [99-104] have successfully demonstrated nanorod array LEDs. Core-shell QWs could be grown on both non-polar or semi-polar plane. Ra *et al.*[104] found that the growth rates of m-plane (2.5 nm) and r-plane (2 nm) are different and the emission wavelengths are also different by 40 nm. Chang *et al.*[105] found that indium content and quantum well thickness vary with the number of QW growth. It is also found that forming a good ohmic contact for the p-contact is difficult in nanorod array LEDs [106].

The axial QW structure has a smaller active region making it suitable for applications such as LED and single photon emitter and are usually grown by MBE or through the top-down method. Nguyen *et al.*[107] have grown InGaN/GaN axial MQW nanorod LEDs and found that a p-type AlGaN blocking layer was necessary to prevent the electron overflow effects and no efficiency droop was observed in their device for injection currents up to 2200 A/cm^{-2}. Hon-Way Lin *et al.* [108] demonstrated white emission with 6000 K color temperature using plasma-assisted MBE grown axial MQW structure. They found the emission peak of the MQW could be controlled by growth temperature and In/Ga beam fluxes.

Single nanorod LEDs are attracting a lot of attention due to their small size and the possibility of integration with Si circuits. The first GaN single core-shell LED was reported by Qian *et al.* [109] with the following structure: n-GaN inner core, followed by a single undoped InGaN/GaN quantum well and covered by a p-AlGaN electron blocking layer. Later, J. Emery's group [110] demonstrated a single core-shell nanorod LED emitted at 392 nm. They confirmed there was no QCSE in the non-polar MQW structure through power-dependent CL measurements where no blue shift in the emission wavelength was observed with increasing excitation energy. Blue shift is related to the increased number of electron-hole pairs caused by QSCE screening effect. J. Emery's group [111] have also synthesized nanorod LEDs and detector on the same Si/SiO_2 template. The devices were connected by a SiN waveguide and the on/off state could be switched within less than 0.5 s.

Daylight illumination with white LEDs is one of the important applications in GaN-based LEDs. White light could be generated using two general approaches: polychromatic LEDs light mixing (blue, green, yellow, red, and etc.) or LED and

wavelength-converters combination (phosphors, semiconductor, and dyes). The commonly used phosphors [77] may lead to low modulation speed, low colour rendering index, and loss in colour conversion. Phosphors-free white LEDs, on the other hand, could be realized using nanorods with emission from the three primary colours by tuning the indium content in InGaN quantum wells. Hiroto Sekiguchi *et al.* [112] have found that in selective area growth, changing the nanorod diameter from 130 to 270 nm could tune the InGaN MQW emission from 513 to 632 nm. The change was attributed to the beam shadow effect caused by nearby nanorod and different in diffusion rates of the indium and gallium adatoms. Other structures such as quantum dots are also used to realize a wide emission wavelength range. Nguyen *et al.* [107] have inserted ten InGaN quantum dots with different indium content to achieve a steady chromaticity coordinate even under high injection current.

2.3 Experimental techniques

2.3.1 Epitaxial growth: MOCVD technique

MOCVD (metalorganic chemical vapour deposition), also known as MOVPE (metalorganic vapour phase epitaxy) is a crystal growth technique using organometallic precursors for chemical vapour deposition. We used an Aixtron 3×2FT close-coupled showerhead MOCVD system to grow the GaN nanorods. A photo and a schematic drawing of the system are shown in figure 2.15. The system could be divided into four major parts: the gas handling system, the reaction chamber, the heating and temperature control system, and the pumping, exhaust and pressure control system.

The gas handling system includes the sources (precursors and other necessary gas supply) and gas mixing system. Organometallic precursors such as trimethylgallium (TMGa), triethylgallium (TEGa), trimethylaluminium (TMAl), trimethylindium (TMIn) were used as the Ga, Al and In source, respectively. NH_3 was used as the nitrogen source. SiH_4 was used as the n-type. The carrier gases were nitrogen and/or hydrogen.

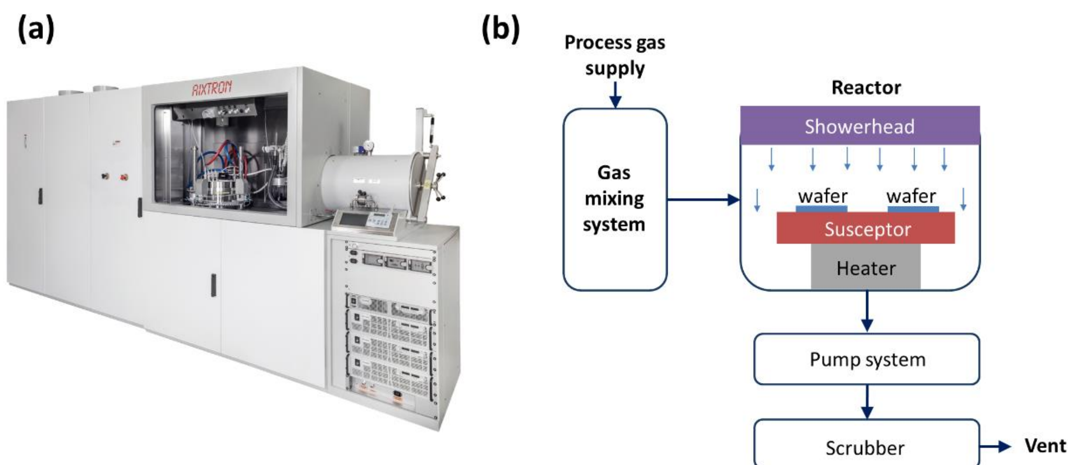

Figure 2.15 (a) A photo (adapted from [113]) and (b) a schematic drawing of the Aixtron 3×2FT close-coupled showerhead MOCVD system.

The schematic drawing of the gas delivery circuit is shown in figure 2.16. The metalorganic precursors were stored in pressure-controlled cylinders in temperature-controlled baths and carried into the reactor by the carrier gas. The substrate was heated to high temperature, while metalorganic precursors and hydride sources would pyrolyse inside the reactor leading to the growth of GaN nanorods:

$$Ga(CH_3)_3 + NH_3 \rightarrow GaN + 3CH_4 \quad (2.1)$$

$$Ga(C_2H_5)_3 + NH_3 \rightarrow GaN + 3\ C_2H_6 \quad (2.2)$$

During the growth of GaN nanorod, silane was additionally added, not only for n-doping, but also to promote the vertical growth of nanorod.

The reaction chamber used in this system is a vertical geometry close-coupled showerhead reactor as shown in figure 2.17. Inside the reactor, substrates are held on a SiC covered graphite susceptor. A quartz liner is used between the susceptor and the metallic reactor sidewall to minimise deposition on the chamber walls. The vertical design of the reactor allows the reactants to enter the reactor vertically through the showerhead in close proximity to the wafers to reduce flow vortices and improve uniformity.

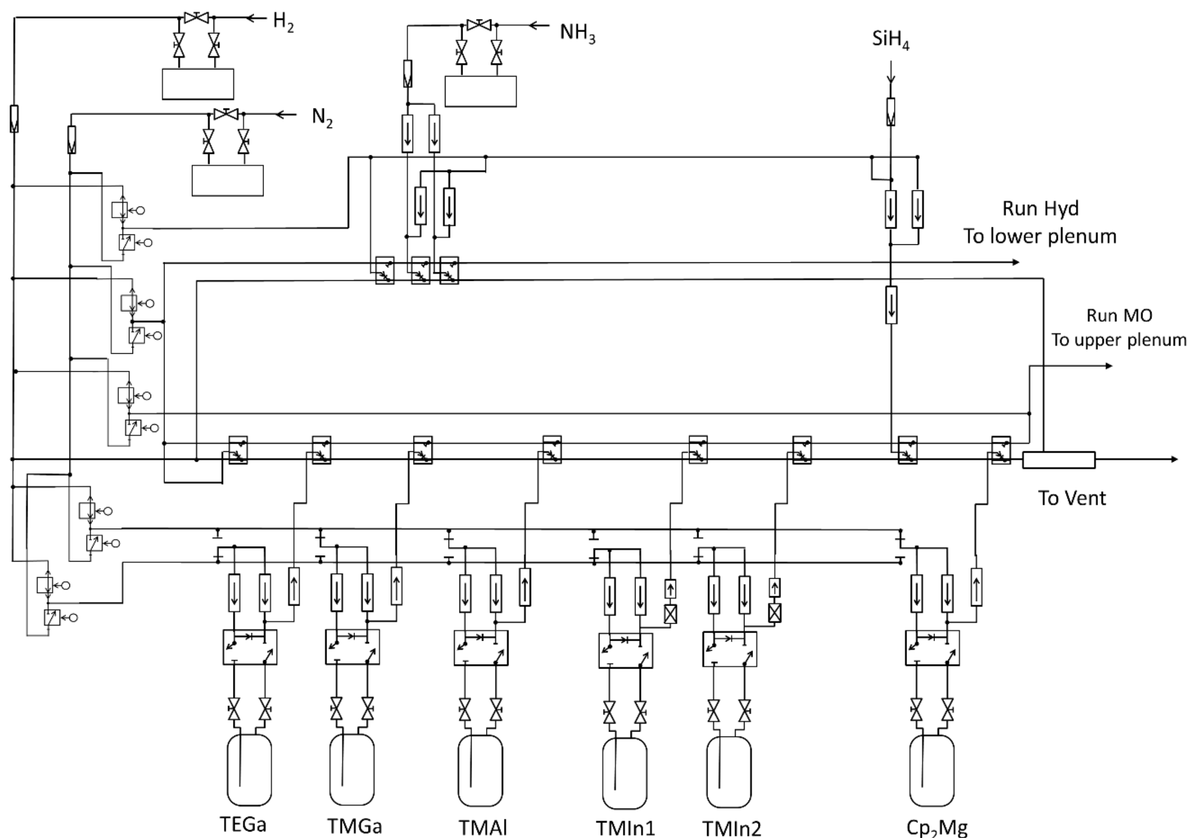

Figure 2.16 Schematic drawing of the gas circuit diagram in an MOCVD system.

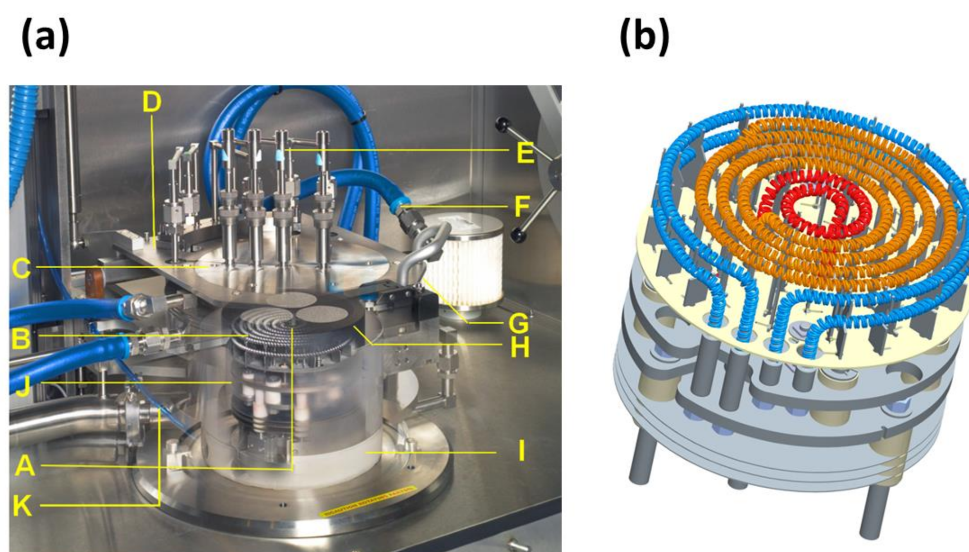

Figure 2.17 MOCVD reactor and heating coils: (a) A photo of the Aixtron 3×2FT close-coupled showerhead MOCVD reactor. A: Thermocouple, B: Tungsten heater, C: Showerhead, D:Reactor lid, E: Optical probe, F: Showerhead water cooling, G: Double O-ring seal, H: Susceptor, I: Quartz liner, J: Susceptor support, K: Exhaust (adapted from [114]). (b) A drawing of heater coils - the center area is Zone A (red), the middle area is Zone B (orange), and the outer area is Zone C (blue) (adapted from [114]).

The reaction chamber is heated by a set of three resistive tungsten coils inside the susceptor as shown in figure 2.17 (b). Each zone is controlled individually with its own power supply. Through balancing the power supply setting, we are able to achieve uniform temperature distribution across the susceptor surface. The susceptor also rotates during the growth to improve uniformity during growth.

A schematic drawing of the reaction process in the reactor is depicted in figure 2.18 and could be divided into 7 steps: (1) precursors introduced into the chamber through the two separated plenum to minimize pre-reaction and transported to the substrate by the carrier gas, (2) molecules diffusing through the boundary layer, (3) molecules adsorb onto the substrate, (4) molecules diffusing to the crystallization area. (5) chemical deposition of the crystal, (6) by-product desorb and diffuse out of the boundary layer, and (7) by-products transported out of the reactor.

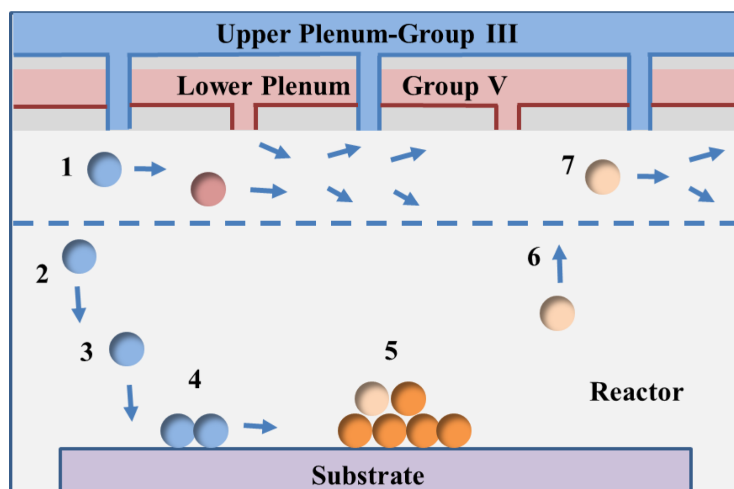

Figure 2.18 Schematic drawing of precursors reaction inside the MOCVD chamber.

The reactor is connected with the pumping and pressure control system. Before leaving the system, the effluents need to pass through the two-stage particle filters and the toxic gases would be absorbed in the scrubber to minimize the impact on the environment.

2.3.2 Thermal evaporation

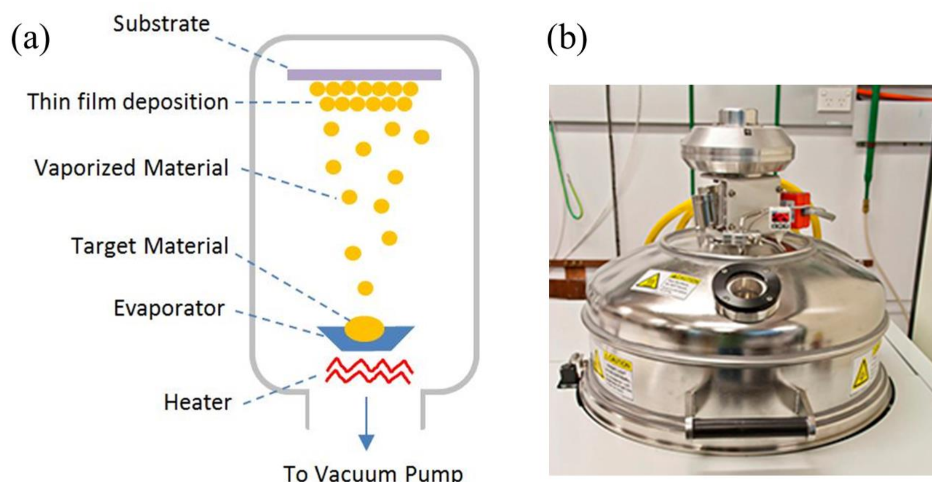

Figure 2.19 Schematic drawing and a photo of the thermal evaporator system: (a) Schematic drawing of the thermal evaporation process. (b) Photo of the Temescal BJD-2000 electron beam/thermal evaporator system.

Due to the poor conductivity of GaN and sapphire, a metal layer is needed to enhance the SEM imaging quality and to improve the accuracy during TEM sample preparation by the FIB milling process. Thermal evaporation is used to deposit 10-100 nm of gold onto the nanorod and substrate surface.

The schematic drawing of the thermal evaporation system is shown in figure 2.19 (a). Under a high vacuum environment, the target material in the resistive boat is heated to evaporation point by joule heating. The vapourized material would travel from the source to the substrate and would nucleate and form into a thin film onto the substrate. A wide range of materials is available for the thermal evaporation process, such as Al, Au, Ni and etc.

A high vacuum is essential for evaporation processes [115]. Firstly, during the travel from the source to the substrate, the vapour molecule might collide with the gas molecule and change its travel direction, which will affect the substrate coverage homogeneity. A high vacuum is required to reduce the collision chance and achieve straight travel from the source to the substrate. Secondly, the background gases in the chamber such as oxygen and moisture would reduce film purity. Under a high vacuum, when the partial pressure of these gases is reduced to less than 10^{-6} Torr, the purity of the deposited films is largely improved [115]. A photo of the Temescal BJD-2000 electron beam/thermal evaporator system used is shown in figure 2.19 (b). This system

consists of a scroll pump and a cryo-pump allowing for a vacuum range down to the mid-10^{-7} torr, which ensured a high purity of the evaporated films.

2.3.3 Scanning electron microscopy

The nanorods are characterized by scanning electron microscopy (SEM) for their diameter, length, and orientation relationship with the substrate. A schematic drawing of the SEM is shown in figure 2.20. The electron beam is produced by an electron gun and focused by a set of condenser lens and objective lens into a fine probe (1-10 nm in diameter). When the electron probe is irradiated on the sample, various signals are emitted from the sample surface (figure 2.21). This information is collected by different types of detectors and converted into electric signals for imaging and elemental analysis.

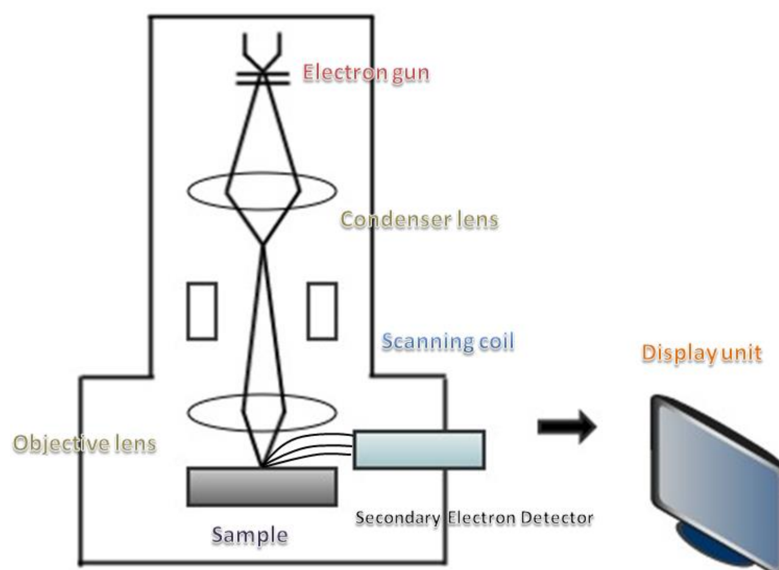

Figure 2.20 Schematic drawing of an SEM system.

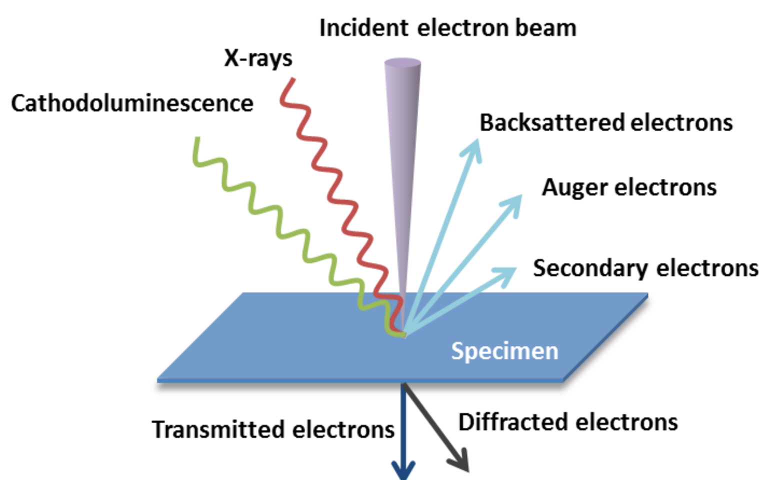

Figure 2.21 Different signals produced when an electron beam impinges on a sample.

The main signal sources of imaging are secondary and backscatter electrons. Secondary electrons are produced by valence electrons emission with low energy. This means only the electrons generated at the surface are emitted, while those generated deeper in the sample would be absorbed by the sample. Therefore, secondary electrons are very sensitive to the surface and used for imaging the surface topography. Backscattered electrons are incident electrons that are scattered backward when hitting the sample. Backscattered electrons have higher energy and provide information from a deeper region of the sample. As the energy and yield of the backscattered electrons depend on the atomic number of the atoms in the sample, they are very sensitive to the sample composition. Two types of instruments were used in this work: a FEI Verios 460 SEM system and a FEI Helios 600 Nanolab system. The acceleration voltage used was 1-5 kV.

2.3.4 Energy-dispersive X-ray spectroscopy

Energy-dispersive X-ray spectroscopy (EDX) is an analytical technique that probes the composition of the material using electron beams. As discussed in section 2.3.2, X-ray is among one of the signals produced when a high energy electron beam impinges on a sample. The primary energy electrons excite the core electrons to higher energy states, creating a low-energy vacancy in the electronic structure. This leads to the electrons from higher energy levels filling the vacancies and characteristic X-rays are emitted as shown in figure 2.22 (a). The energy of the X-rays is equal to the energy difference between the two electron shells where the transition took place. Due to the unique atomic structure of each element, the X-ray emission spectrum is also unique for different elements, which enables the identification of the elemental composition.

EDX measurements could be carried out in SEM or TEM systems equipped with EDX detectors. The EDX spectra could be obtained from a specific spot (spot scan), a line of spots (line scan), and a raster scan across the imaging area (EDX map). EDX maps are collected under STEM mode where the electron beam is raster-scanned and the EDX spectrum is collected at each pixel. EDX map at the edge of a GaN nanorod cross-section is shown in figure 2.22 (b) where Ga element is clearly visible in the nanorod area with high contrast.

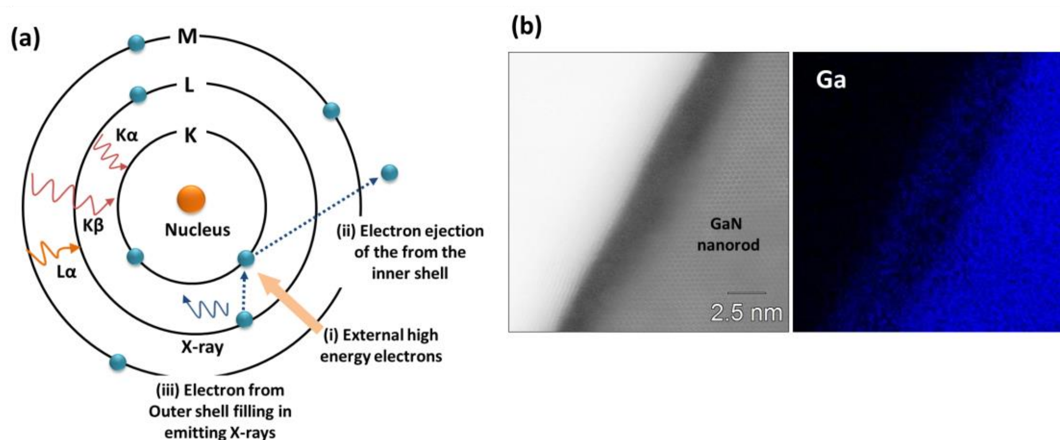

Figure 2.22 Schematic drawing of EDX process and an example of GaN STEM/EDX map: (a) X-ray emission process when high energy electrons impinge on the sample. (b) STEM image and EDX map of Ga element using JEOL ARM 200F.

2.3.5 Cathodoluminescence

Cathodoluminescence (CL) is a photon emission process caused by electron beam irradiation on a sample. Under electron beam irradiation, free carriers are generated by promoting the electrons from the valence band to the conduction band. Then the excited electrons recombine with holes and emit photons through a radiative recombination process.

A schematic drawing of the collection section of a CL system, which is usually housed in a scanning electron microscope, is shown in figure 2.23 (a). The electron beam passes through an aperture in the parabolic mirror and impinged on the sample. Photons generated are focused and reflected by the mirror into a spectrometer-detector system that could switch between parallel mode (charge-coupled device) and monochromatic mode (photomultiplier). When conducting the spatial resolved CL, the parallel mode collects a full CL spectrum at each pixel of the imaging area, while the monochromatic mode only collects a greyscale image

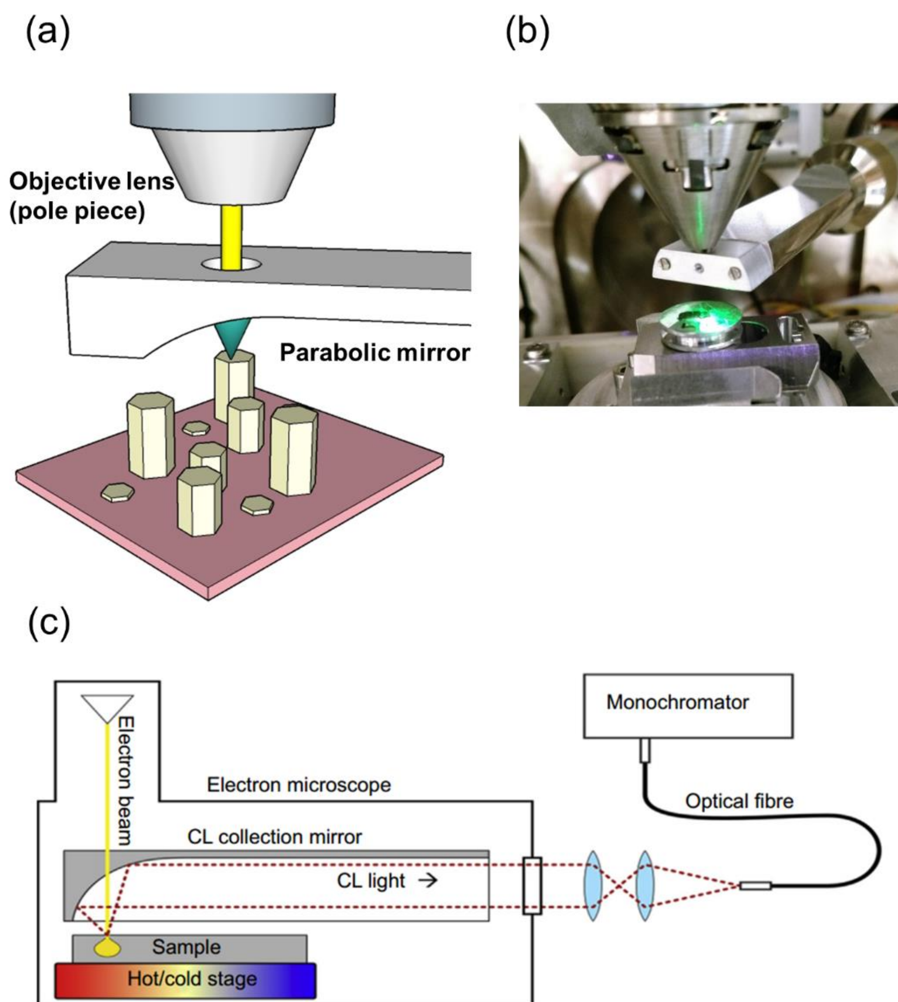

Figure 2.23 Schematic drawings and photo of a CL system: (a) Schematic drawing and (b) photograph of the collection section of a CL system. (c) Schematic drawing of a CL system with the parabolic mirror for light collection (adapted from [116]).

Compared with other luminescence techniques such as PL, CL has several advantages such as (i) high spatial resolution. The spatial resolution (<50 nm) of CL is much higher than PL (<200 nm), which offers the opportunity to link the optical properties of the nanostructure with its morphology and composition. Furthermore, by combining CL imaging with SEM imaging, the spatial location of luminescence could be mapped to provide spatial-spectral information. (ii) Application in large bandgap materials. The electron beam could excite electrons in large bandgap materials ($E_g > 6$ eV) which are not easily accessible by lasers in the PL technique. (iii) Control the depth of excitation. The electron beam in SEM could be tuned from 1 to 30 kV that offers

depth information from tens to a few hundred nanometers based on the material property. The equipment used in this thesis is FEI Verios 460 SEM equipped with a Gatan MonoCL4 Elite cathodoluminescence (CL) detector.

2.3.6 Transmission electron microscopy

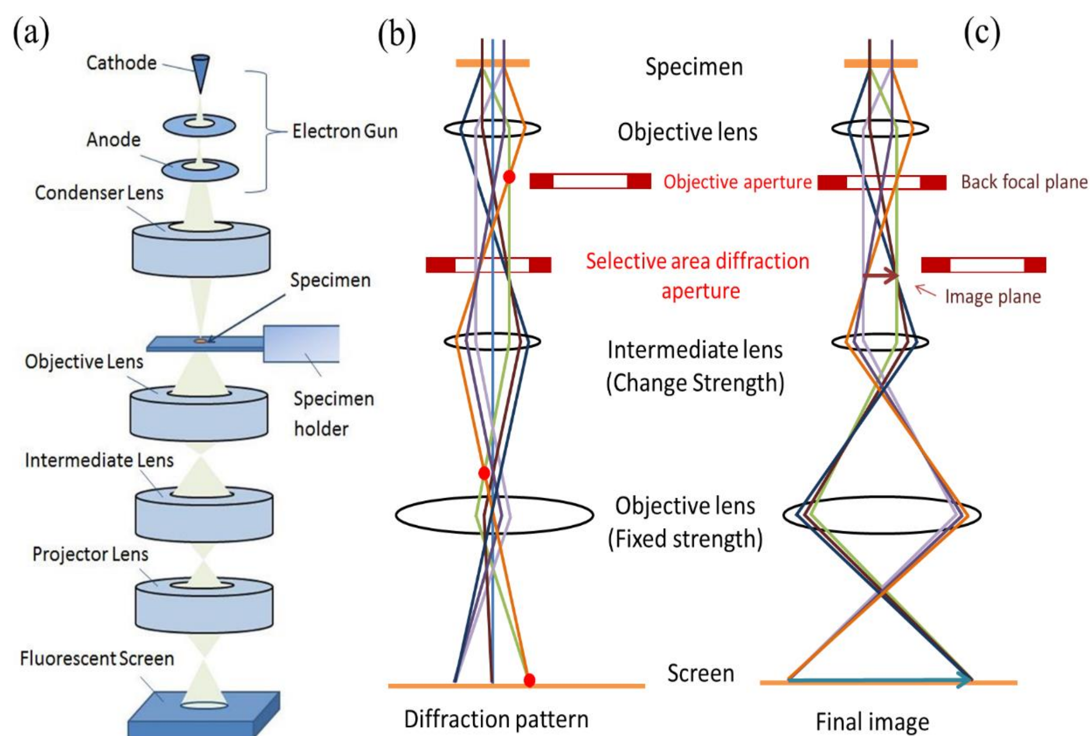

Figure 2.24 Schematic drawings of the imaging system in TEM: (a) Schematic drawing of the main components in a TEM. (b, c)Electron beam paths to form diffraction patterns (*b*) and imaging (*c*) in TEM.

Transmission electron microscopy (TEM) mostly used transmitted electrons and diffracted electrons for imaging. Furthermore, by increasing the electron beam energy (100-300 kV), higher magnification can be achieved which allows the imaging of the atomic planes, and crystalline defects in the sample. TEM in this thesis was performed using a JOEL 2100F in the center of microscopy at ANU.

The TEM contains an electron gun, a set of condenser lens, objective lens, intermediate lens and projector lens, and a fluorescent screen (figure 2.24 *a*). Two basic operations of TEM include diffraction mode (figure 2.24 *b*) and imaging mode (figure 2.24 *c*). In diffraction mode, the selective area diffraction (SAD) aperture is inserted and projector lens is used to select the back focal plane of the intermediate lens as the object. The diffraction patterns are then projected onto the screen. The diffraction spots

represent the inter-plane spacing of different atomic planes, which helps to determine the crystal phases such as zinc-blende and wurtzite structure. In imaging mode, the objective aperture is inserted and the projector lens is used to select the image plane of the objective lens as the object. By using the objective aperture to select the transmitted beam or diffracted beam, imaging mode could be switched between bright field and dark field.

2.3.7 Scanning transmission electron microscope

In this thesis, apart from traditional TEM, we additionally used an aberration-corrected scanning transmission electron microscope (STEM) with a sub-Angstrom resolution to determine the polarity of the GaN nanorods.

Compared with conventional TEM, STEM is equipped with a scanning coil and detector. The beam in STEM is focused into a fine probe that scans over the sample in a raster pattern. The detector collects the scattered electrons and the images are formed by plotting the electron intensity as a function of the probe position. Because of the extremely thin sample used in the system, the spatial resolution is controlled by the size of the probes. The probe size is able to reach below the interatomic spacings in many materials. To form a small and intense probe, field emission guns are used as electron sources such as the cold field-emission gun or the Schottky thermally assisted field-emission gun [117].

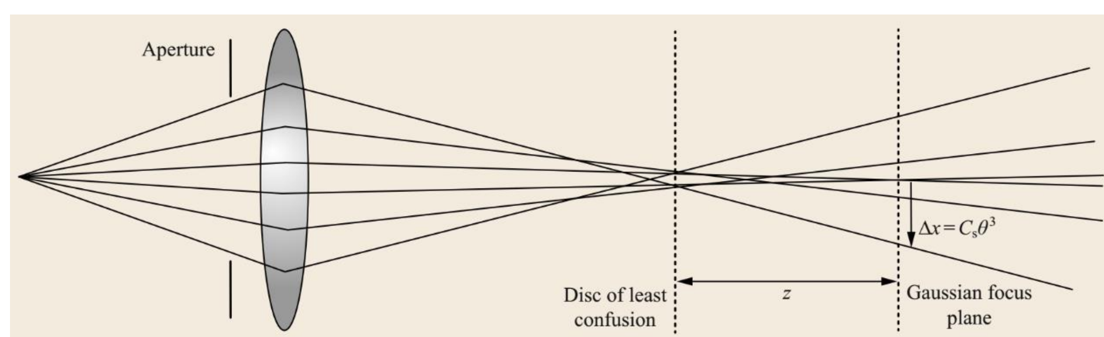

Figure 2.25 Schematic drawing of the effect of spherical aberration in a geometrical optics view (adapted from [117]).

The size of the probe is also affected by inherent aberrations, such as chromatic and spherical aberrations. As shown in figure 2.25, the beam is supposed to focused at the Gaussian plane, but spherical aberration would cause an overfocusing of the high angle rays. The distance is proportional to the ray's cube angle and the proportionality

constant is Cs. To correct the aberrations in the lenses, special lenses are used to provide negative spherical aberrations. Nowadays, the aberration correctors with multipole and additional windings could diagnose and rapidly correct the aberrations by adjusting the multipole power supplies.

Several different detectors could be equipped on STEM such as electron energy EELS, EDX, annual dark-field imaging, and annular bright-field (ABF) imaging. Under the ABF imaging mode, the atomic 'dumb-bells' could be distinguished based on the atomic number (Z) contrast. Compared with other methods such as Kelvin probe force microscopy (KPFM), and CBED, the advantages of this method include high accuracy and the areas of interest could be examined more precisely down to high spatial resolution. The STEM imaging in this thesis was conducted in the University of Wollongong using a JEOL ARM 200F.

2.3.8 Focused ion beam for TEM sample preparation

TEM sample preparation methods are usually chosen based on the types of samples, sample size, and area of interest. Nanorods with a diameter less than 200 nm have good electron beam transparency, so they could be directly transferred onto the carbon-coated copper grid. For nanorods with larger diameters, lamella is required and can be prepared by the focused ion beam (FIB).

FIB milling is a technique that selectively thins down a target region of the sample with desired shapes while monitoring and controlling the milling region by SEM. Here we used a FEI Helios 600 Nanolab dual-beam FIB/SEM system equipped with an electron beam column (direct monitoring) and a liquid Ga ion beam column (milling). A schematic drawing of the dual-beam column and chamber is shown in figure 2.26 (a) [118]. The angle between the two columns is 52°, so the sample stage needs to be raised to an eucentric point (a height that field of view is maintained when tilting) where the two beams cross and the sample is tilted to achieve desired beam incidence angle.

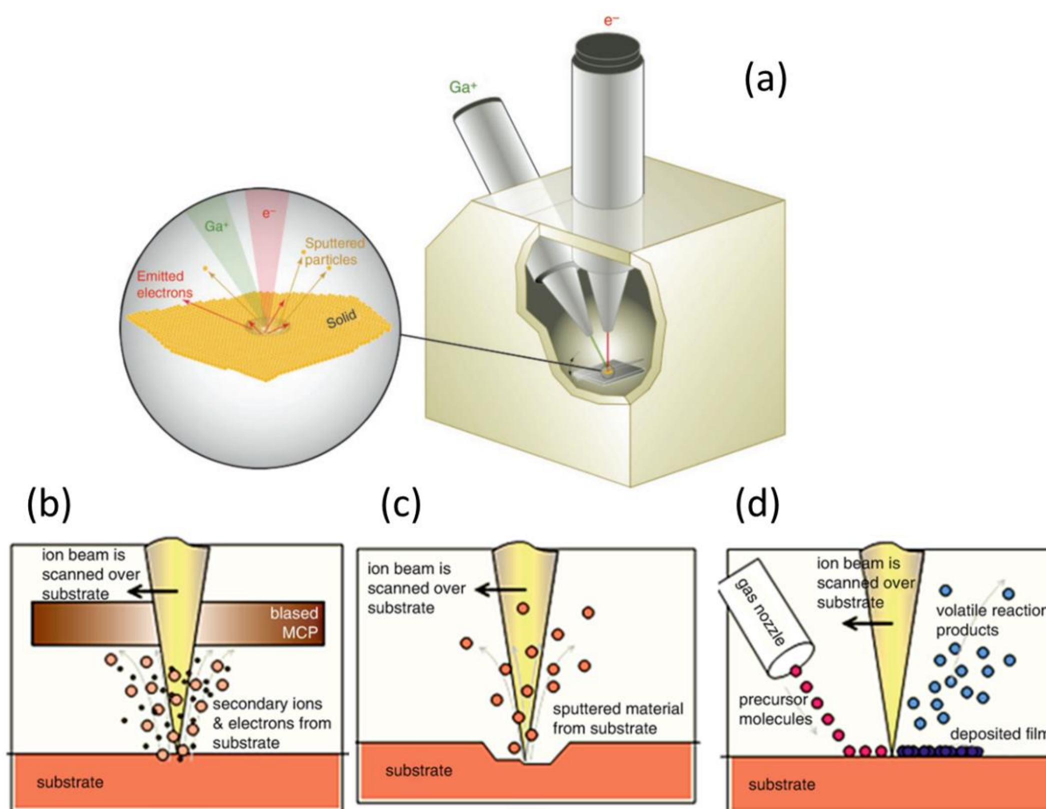

Figure 2.26 Schematic drawings of a dual FIB-SEM system and related-process: (a) Schematic drawing of a dual-beam FIB-SEM system. An enlarged view shows the interaction between the two beam sources and the sample (adapted from [118]). (b-d) Schematic illustration of ion beam imaging, milling, and deposition process (adapted from [119]).

The imaging, milling, and deposition capability of the FIB system are illustrated in figure 2.26 (b) to (d). As shown in figure 2.26 (c), arbitrary shapes could be milled by scanning the ion beam over the sample. The ion beam assisted deposition process is illustrated in figure 2.26 (d), where both metal (Pt, Au) and insulator material (SiO_2) could be deposited. A gas nozzle is inserted into the chamber to inject precursors onto the surface. Then, the ion beam decomposes the precursors into the desired deposition layer and the volatile reaction materials are removed from the chamber at the same time. The deposited layer also contains C and Ga because of the organic precursors and Ga ion beam used in the process.

The detailed procedure for the preparation of a nanorod lamella in FIB is illustrated in figure 2.27. Firstly, the nanorod is transferred onto a conductive substrate and the area of interest is marked as a guide for cutting (figure 2.27 *a*). Then, a Pt layer is in-situ deposited over the nanorod to avoid the milling of the target region. Next, the

surrounding of the nanorod is milled in a staircase-like profile as shown in figure 2.27 b with a 30 kV Ga ion-beam to prepare a section of a thickness of a few μm or less. For in-situ TEM sample preparation, the thin section is first welded onto a manipulator and then welded onto the half-ring TEM grid (figure 2.27 *c*) for finally thinning down. Finally, the fixed specimen is milled with a Ga ion beam at a lower accelerating voltage of about 5-15 kV (for decreasing damages to the specimen) to create a lamella around 50 to 80 nm that is suitable for high-resolution TEM and STEM imaging.

There are challenges in FIB lamella preparation, such as Ga-ion implantation during the milling process. The implanted Ga-ions under high voltage (30 kV) could leave a thin 'dead layer' on the surface of the sample, or crystalline sample could become defective or amorphous due to ion bombardment. To remove the 'dead layer', typically a low-voltage (5 kV) cleaning process is used after the main milling process.

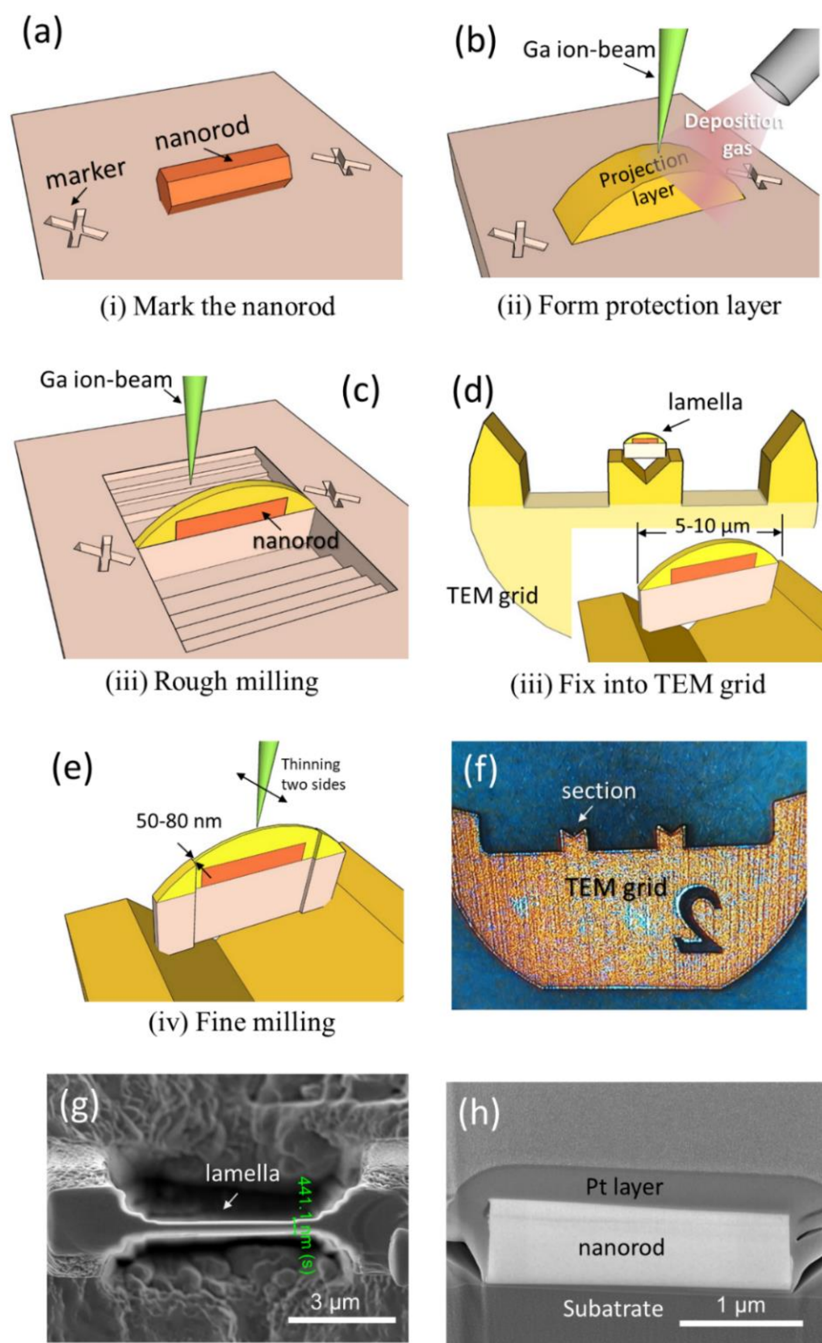

Figure 2.27 Schematic drawings, photo and SEM images of the FIB-lamella preparation process: (a-e) Schematic illustration for nanorod FIB-lamella process. a: A nanorod lying down on the substrate with two 'X' markers made by FIB; b: Coating a Pt layer for protection; c: Roughly milling the surroundings of the target area with Ga ion-beam to prepare a section; d: Fix a section onto the TEM grid (inset: enlarged lamella area); e: Fine milling to thinning the lamella (thickness: 10 to 100 nm). (f) The milled sample is mounted on a half-ring holder after in-situ lift-out. (g) SEM image for a lamella sample before fine milling. (h) the SEM image of the sample shown in figure *g* before fine milling.

2.3.9 Nanoscale secondary ion mass spectrometry

Secondary ion mass spectrometry is a technique that uses ion beams to bombard the sample surface to extract secondary ions for analysis. The technique of nanoscale secondary ion mass spectrometry (nano-SIMS) is a technique based on the SIMS using chemical imaging mass spectrometer to reach the nanoscale resolution of the sample [120].

The ion bombardment process [121] is illustrated in figure 2.28 where the elastic and inelastic collision would lead to the ejection of a variety of radiation and particles including electrons, neutral/ionized atoms, molecules, and clusters. Apart from the original chemical composition of the sample, the composition of the ejected particle flux could be affected by the oxygen or other electronegative atoms adsorbed or incorporated on the surface of the sample [122].

In nano-SIMS, the continuous ion beam bombardment sputters the sample surface and consequent secondary ions are ejected [120]. The secondary ions are first sorted inside an electrostatic sector based on their energy level. Then in the mass spectrometer, they would be separated physically under the Lorentz force induced by the magnetic field based on different mass-to-charge ratios [123].

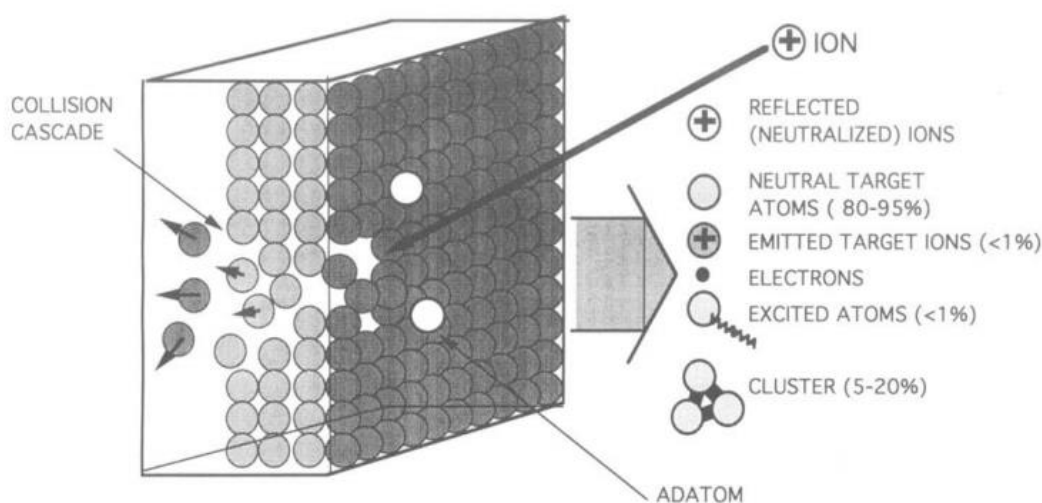

Figure 2.28 Schematic drawing of the ion bombardment process at a metal surface. The percentage values are given under approximate contributions on a clean metal surface (adapted from [121]).

The schematic illustration of the Cameca Nano-SIMS machine used in this thesis is

shown in figure 2.29 where two reactive ion-sources, Cs^+ and O^- are used. The resolution is around 50 nm using the Cs^+ beam and 150 nm for the O^- beam. A co-axial design of the primary beam and the secondary beam is used to achieve smaller beam sizes and higher collecting efficiency. Using Cs^+ as primary ions would enhance the ionization yield of electro-negative elements (such as H, C, O, N, F, Cl) compared with non-reactive species (such as Ga and Au). The Cameca Nano-SIMS 50/50L machine is equipped with 5 to 7 detectors to acquire 5 to 7 mass maps in parallel and has the capability for high mass resolution and isotopic identification.

Nano-SIMS possesses many merits [124] making it suitable for analyzing the chemical composition of micro- and nano-scale materials such as (i) Large analytical range covering the whole periodic table (starting from hydrogen) and high sensitivity down to parts per billion level. (ii) Variable depth resolution by changing ion-beam energy, which makes three-dimension compositional maps possible. (iii) Different sputtering ions (Cs^+, O^-, etc.) for different purposes and could be focused into a fine ion-beam to conduct analysis on a small material volume. These characteristics make it widely used in the research of thin films and nanomaterials to investigate doping and impurities concentration, crystallographic information, and phase separation [124]. The nano-SIMS could be also combined with TEM for the correlated mineralogic and isotopic studies at the sub-micrometer scale. However, nano-SIMS is a destructive measurement, the target area would be seriously damaged after the analysis. Also, it is only qualitative to semi-qualitative and to determine the absolute concentration of the various elements and impurities in the material, reference targets are required [124].

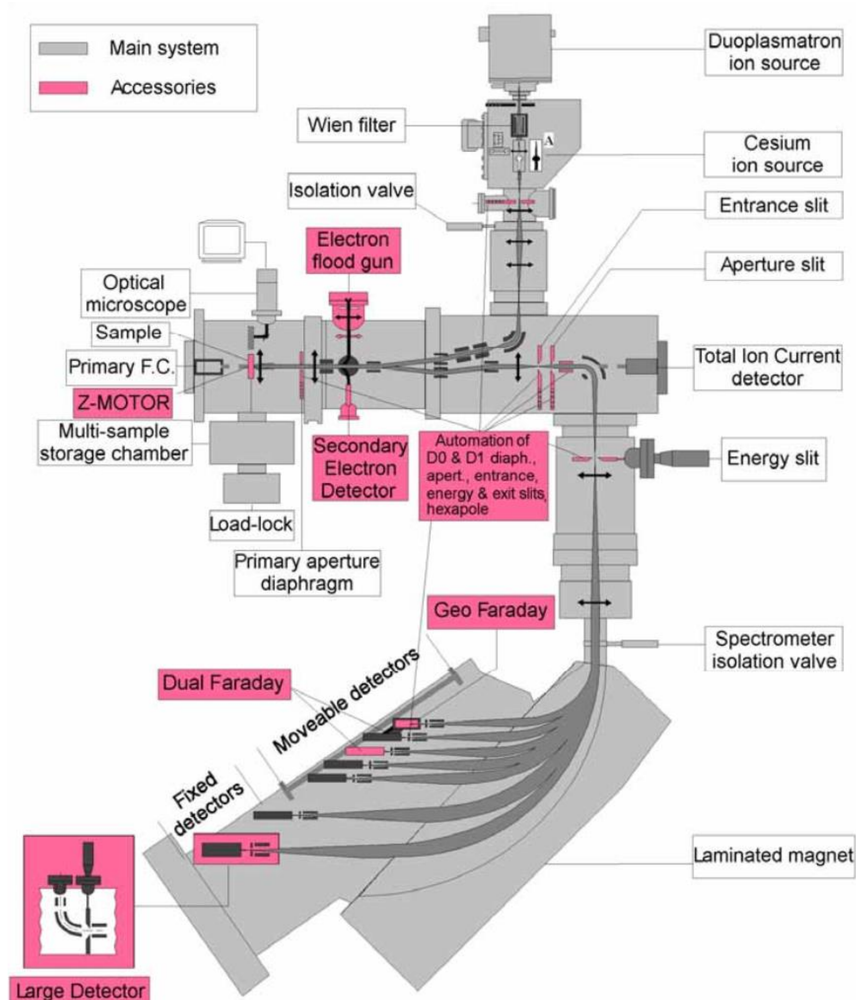

Figure 2.29 Schematic drawing of the Cameca Nano-SIMS 50/50L machine (adapted from [125]).

References

1. H. Okumura, K. Ohta, G. Feuillet, K. Balakrishnan, S. Chichibu, H. Hamaguchi, P. Hacke and S. Yoshida, *Growth and characterization of cubic GaN.* Journal of Crystal Growth, 1997. **178**(1): p. 113-133.

2. S. Strite and H. Morkoç, *GaN, AlN, and InN: A review.* Journal of Vacuum Science & Technology B: Microelectronics and Nanometer Structures, 1992. **10**: p. 1237-1266.

3. F. Tuomisto, K. Saarinen, B. Lucznik, I. Grzegory, H. Teisseyre, T. Suski, S. Porowski, P. R. Hageman and J. Likonen, *Effect of growth polarity on vacancy defect and impurity incorporation in dislocation-free GaN.* Applied Physics Letters, 2005. **86**(3): p. 031915.

4. Q. Sun, Y. S. Cho, I. H. Lee, J. Han, B. H. Kong and H. K. Cho, *Nitrogen-polar GaN growth evolution on c-plane sapphire.* Applied Physics Letters, 2008. **93**(13): p. 131912.

5. N. Shuji, *GaN growth using GaN buffer layer.* Japanese Journal of Applied Physics, 1991. **30**(10A): p. L1705.

6. H. Amano, N. Sawaki, I. Akasaki and Y. Toyoda, *Metalorganic vapor phase epitaxial growth of a high quality GaN film using an AlN buffer layer.* Applied Physics Letters, 1986. **48**(5): p. 353-355.

7. S. Mohn, N. Stolyarchuk, T. Markurt, R. Kirste, M. P. Hoffmann, R. Collazo, A. Courville, R. Di Felice, Z. Sitar, P. Vennéguès and M. Albrecht, *Polarity control in group-III nitrides beyond pragmatism.* Physical Review Applied, 2016. **5**(5): p. 054004.

8. B. Alloing, S. Vezian, O. Tottereau, P. Vennegues, E. Beraudo and J. Zuniga-Perez, *On the polarity of GaN micro- and nanowires epitaxially grown on sapphire (0001) and Si(111) substrates by metal organic vapor phase epitaxy and ammonia-molecular beam epitaxy.* Applied Physics Letters, 2011. **98**(1): p. 011914.

9. M. Hetzl, M. Kraut, T. Hoffmann and M. Stutzmann, *Polarity control of heteroepitaxial GaN nanowires on diamond.* Nano Letters, 2017. **17**(6): p. 3582-3590.

10. X. J. Chen, G. Perillat-Merceroz, D. Sam-Giao, C. Durand and J. Eymery, *Homoepitaxial growth of catalyst-free GaN wires on N-polar substrates.* Applied Physics Letters, 2010. **97**(15): p. 151909.

11. M. D. Brubaker, A. Roshko, P. T. Blanchard, T. E. Harvey, N. A. Sanford and K. A. Bertness, *Spontaneous growth of GaN nanowire nuclei on N- and Al-polar AlN: A piezoresponse force microscopy study of crystallographic polarity.* Materials Science in Semiconductor Processing. **55**: p. 67-71.

12. F. Dwikusuma and T. F. Kuech, *X-ray photoelectron spectroscopic study on sapphire nitridation for GaN growth by hydride vapor phase epitaxy: Nitridation mechanism.* Journal of Applied Physics, 2003. **94**(9): p. 5656.

13. P. M. Coulon, M. Mexis, M. Teisseire, M. Jublot, P. Vennéguès, M. Leroux and J. Zuniga-Perez, *Dual-polarity GaN micropillars grown by metalorganic vapour phase epitaxy: Cross-correlation between structural and optical properties.* Journal of Applied Physics, 2014. **115**(15): p. 153504.

14. M. de la Mata, C. Magen, J. Gazquez, M. I. B. Utama, M. Heiss, S. Lopatin, F. Furtmayr, C. J. Fernández-Rojas, B. Peng, J. R. Morante, R. Rurali, M. Eickhoff, A. Fontcuberta i Morral, Q. Xiong and J. Arbiol, *Polarity assignment in ZnTe, GaAs, ZnO, and GaN-AlN nanowires from direct dumbbell analysis.* Nano Letters, 2012. **12**(5): p. 2579-2586.

15. V. Purushothaman and K. Jeganathan, *Investigations on the role of Ni-catalyst*

for the VLS growth of quasi-aligned GaN nanowires by chemical vapor deposition. Journal of Nanoparticle Research, 2013. **15**(7): p. 1789.

16. R. E. Diaz, R. Sharma, K. Jarvis, Q. L. Zhang and S. Mahajan, *Direct observation of nucleation and early stages of growth of GaN nanowires.* Journal of Crystal Growth, 2012. **341**(1): p. 1-6.

17. C. Chèze, L. Geelhaar, O. Brandt, W. M. Weber, H. Riechert, S. Münch, R. Rothemund, S. Reitzenstein, A. Forchel and T. Kehagias, *Direct comparison of catalyst-free and catalyst-induced GaN nanowires.* Nano Research, 2010. **3**(7): p. 528-536.

18. X. F. Duan and C. M. Lieber, *Laser-assisted catalytic growth of single crystal GaN nanowires.* Journal of the American Chemical Society, 2000. **122**(1): p. 188-189.

19. J. P. Ahl, H. Behmenburg, C. Giesen, I. Regolin, W. Prost, F. J. Tegude, G. Z. Radnoczi, B. Pecz, H. Kalisch, R. H. Jansen and M. Heuken, *Gold catalyst initiated growth of GaN nanowires by MOCVD.* Physica Status Solidi C: Current Topics in Solid State Physics, 2011. **8**(7-8): p. 2315-2317.

20. V. Dobrokhotov, D. N. McIlroy, M. G. Norton, A. Abuzir, W. J. Yeh, I. Stevenson, R. Pouy, J. Bochenek, M. Cartwright, L. Wang, J. Dawson, M. Beaux and C. Berven, *Principles and mechanisms of gas sensing by GaN nanowires functionalized with gold nanoparticles.* Journal of Applied Physics, 2006. **99**(10): p. 104302.

21. T. Y. Kim, S. H. Lee, Y. H. Mo, H. W. Shim, K. S. Nahm, E. K. Suh, J. W. Yang, K. Y. Lim and G. S. Park, *Growth of GaN nanowires on Si substrate using Ni catalyst in vertical chemical vapor deposition reactor.* Journal of Crystal Growth, 2003. **257**(1-2): p. 97-103.

22. T. Kuykendall, P. Pauzauskie, S. K. Lee, Y. F. Zhang, J. Goldberger and P. D. Yang, *Metalorganic chemical vapor deposition route to GaN nanowires with triangular cross sections.* Nano Letters, 2003. **3**(8): p. 1063-1066.

23. T. Kuykendall, P. J. Pauzauskie, Y. Zhang, J. Goldberger, D. Sirbuly, J. Denlinger and P. Yang, *Crystallographic alignment of high-density gallium nitride nanowire arrays.* Nature Materials, 2004. **3**(8): p. 524-528.

24. F. Qian, Y. Li, S. Gradečak, D. Wang, C. J. Barrelet and C. M. Lieber, *Gallium nitride-based nanowire radial heterostructures for nanophotonics.* Nano Letters, 2004. **4**(10): p. 1975-1979.

25. Z. Xiang, C. Jordan, C. Samuel and G. Silvija, *Using seed particle composition to control structural and optical properties of GaN nanowires.* Nanotechnology, 2012. **23**(28): p. 285603.

26. B. Alloing and J. Zúñiga-Pérez, *Metalorganic chemical vapor deposition of GaN nanowires: From catalyst-assisted to catalyst-free growth, and from self-assembled to selective-area growth.* Materials Science in Semiconductor

Processing. **55**: p. 51-58.

27. D. Tham, C. Y. Nam and J. E. Fischer, *Defects in GaN nanowires.* Advanced Functional Materials, 2006. **16**(9): p. 1197-1202.

28. S. Y. Bae, K. Lekhal, H. J. Lee, J. W. Min, D. S. Lee, Y. Honda and H. Amano, *Selective-area growth of doped GaN nanorods by pulsed-mode MOCVD: Effect of Si and Mg dopants.* Physica Status Solidi B, 2017. **254**(8): p. 1600722.

29. K. Choi, M. Arita and Y. Arakawa, *Selective-area growth of thin GaN nanowires by MOCVD.* Journal of Crystal Growth, 2012. **357**: p. 58-61.

30. J. E. Kruse, L. Lymperakis, S. Eftychis, A. Adikimenakis, G. Doundoulakis, K. Tsagaraki, M. Androulidaki, A. Olziersky, P. Dimitrakis, V. Ioannou-Sougleridis, P. Normand, T. Koukoula, T. Kehagias, P. Komninou, G. Konstantinidis and A. Georgakilas, *Selective-area growth of GaN nanowires on SiO_2-masked Si (111) substrates by molecular beam epitaxy.* Journal of Applied Physics, 2016. **119**(22): p. 224305.

31. S. D. Hersee, X. Y. Sun and X. Wang, *The controlled growth of GaN nanowires.* Nano Letters, 2006. **6**(8): p. 1808-1811.

32. S. F. Li, S. Fuendling, X. Wang, S. Merzsch, M. A. M. Al-Suleiman, J. D. Wei, H. H. Wehmann, A. Waag, W. Bergbauer and M. Strassburg, *Polarity and its influence on growth mechanism during MOVPE growth of GaN sub-micrometer rods.* Crystal Growth & Design, 2011. **11**(5): p. 1573-1577.

33. B. O. Jung, S. Y. Bae and Y. Kato, *Morphology development of GaN nanowires using a pulsed-mode MOCVD growth technique.* CrystEngComm, 2014. **16**(11): p. 2273-2282.

34. J. E. Northrup and J. Neugebauer, *Strong affinity of hydrogen for the GaN(000-1) surface: Implications for molecular beam epitaxy and metalorganic chemical vapor deposition.* Applied Physics Letters, 2004. **85**(16): p. 3429-3431.

35. R. M. Feenstra, Y. Dong, C. D. Lee and J. E. Northrup, *Recent developments in surface studies of GaN and AlN.* Journal of Vacuum Science & Technology B, 2005. **23**(3): p. 1174-1180.

36. B. L. VanMil, H. Guo, L. J. Holbert, K. Lee, T. H. Myers, T. Liu and D. Korakakis, *High temperature limitations for GaN growth by RF-plasma assisted molecular beam epitaxy: Effects of active nitrogen species, surface polarity, hydrogen, and excess Ga-overpressure.* Journal of Vacuum Science & Technology B: Microelectronics and Nanometer Structures Processing, Measurement, and Phenomena, 2004. **22**(4): p. 2149-2154.

37. A. Kelly, G. W. Groves and P. Kidd, *Crystal interfaces.* Crystallography and Crystal Defects, 2012: p. 391-433.

38. Y. T. Lin, T. W. Yeh, Y. Nakajima and P. D. Dapkus, *Catalyst-free GaN nanorods synthesized by selective area growth.* Advanced Functional Materials, 2014. **24**(21): p. 3162-3171.

39. X. Wang, S. Li, M. S. Mohajerani, J. Ledig, H. H. Wehmann, M. Mandl, M. Strassburg, U. Steegmüller, U. Jahn, J. Lähnemann, H. Riechert, I. Griffiths, D. Cherns and A. Waag, *Continuous-flow MOVPE of Ga-polar GaN column arrays and core–shell LED structures.* Crystal Growth & Design, 2013. **13**(8): p. 3475-3480.

40. J. Hartmann, X. Wang, H. Schuhmann, W. Dziony, L. Caccamo, J. Ledig, M. S. Mohajerani, T. Schimpke, M. Bähr, G. Lilienkamp, W. Daum, M. Seibt, M. Straßburg, H. H. Wehmann and A. Waag, *Growth mechanisms of GaN microrods for 3D core–shell LEDs: The influence of silane flow.* Physica Status Solidi A, 2015. **212**(12): p. 2830-2836.

41. L. Rigutti, M. Tchernycheva, A. De Luna Bugallo, G. Jacopin, F. H. Julien, L. F. Zagonel, K. March, O. Stephan, M. Kociak and R. Songmuang, *Ultraviolet photodetector based on GaN/AlN quantum discs in a single nanowire.* Nano Letters, 2010. **10**(10): p. 4284-4284.

42. M. A. Sanchez-Garcia, E. Calleja, E. Monroy, F. J. Sanchez, F. Calle, E. Muñoz and R. Beresford, *The effect of the III/V ratio and substrate temperature on the morphology and properties of GaN- and AlN-layers grown by molecular beam epitaxy on Si(111).* Journal of Crystal Growth, 1998. **183**(1): p. 23-30.

43. R. Koester, J. S. Hwang, C. Durand, S. Dang Dle and J. Eymery, *Self-assembled growth of catalyst-free GaN wires by metal-organic vapour phase epitaxy.* Nanotechnology, 2010. **21**(1): p. 015602.

44. H. M. Kim, D. S. Kim, D. Y. Kim, T. W. Kang, Y. H. Cho and K. S. Chung, *Growth and characterization of single-crystal GaN nanorods by hydride vapor phase epitaxy.* Applied Physics Letters, 2002. **81**(12): p. 2193-2195.

45. R. K. Debnath, R. Meijers, T. Richter, T. Stoica, R. Calarco and H. Luth, *Mechanism of molecular beam epitaxy growth of GaN nanowires on Si(111).* Applied Physics Letters, 2007. **90**(12): p. 123117.

46. C. H. Liao, W. M. Chang, Y. F. Yao, H. T. Chen, C. Y. Su, C. Y. Chen, C. Hsieh, H. S. Chen, C. G. Tu, Y. W. Kiang, C. C. Yang and T. C. Hsu, *Cross-sectional sizes and emission wavelengths of regularly patterned GaN and core-shell InGaN/GaN quantum-well nanorod arrays.* Journal of Applied Physics, 2013. **113**(5): p. 054315.

47. J. Ristić, E. Calleja, S. Fernández-Garrido, L. Cerutti, A. Trampert, U. Jahn and K. H. Ploog, *On the mechanisms of spontaneous growth of III-nitride nanocolumns by plasma-assisted molecular beam epitaxy.* Journal of Crystal Growth, 2008. **310**(18): p. 4035-4045.

48. K. A. Bertness, A. Roshko, N. A. Sanford, J. Barker and A. Davydov, *Spontaneously grown GaN and AlGaN nanowires.* Journal of Crystal Growth, 2006. **287**(2): p. 522-527.

49. C. Tessarek and S. Christiansen, *Self-catalyzed, vertically aligned GaN rod-structures by metal-organic vapor phase epitaxy.* Physica Status Solidi C, 2012.

9(3-4): p. 596-600.

50. C. Tessarek, M. Bashouti, M. Heilmann, C. Dieker, I. Knoke, E. Spiecker and S. Christiansen, *Controlling morphology and optical properties of self-catalyzed, mask-free GaN rods and nanorods by metal-organic vapor phase epitaxy.* Journal of Applied Physics, 2013. **114**(14): p. 144304.

51. W. Xue, L. Shunfeng, F. Sönke, H. W. Hergo, S. Martin, L. Hans-Jürgen, S. Ulrich and W. Andreas, *Mechanism of nucleation and growth of catalyst-free self-organized GaN columns by MOVPE.* Journal of Physics D: Applied Physics, 2013. **46**(20): p. 205101.

52. C. Tessarek, M. Heilmann, E. Butzen, A. Haab, H. Hardtdegen, C. Dieker, E. Spiecker and S. Christiansen, *The role of Si during the growth of GaN micro- and nanorods.* Crystal Growth & Design, 2014. **14**(3): p. 1486-1492.

53. M. Heilmann, G. Sarau, M. Göbelt, M. Latzel, S. Sadhujan, C. Tessarek and S. Christiansen, *Growth of GaN micro- and nanorods on graphene-covered sapphire: Enabling conductivity to semiconductor nanostructures on insulating substrates.* Crystal Growth & Design, 2015. **15**(5): p. 2079-2086.

54. M. Heilmann, A. M. Munshi, G. Sarau, M. Göbelt, C. Tessarek, V. T. Fauske, A. T. J. van Helvoort, J. Yang, M. Latzel, B. Hoffmann, G. Conibeer, H. Weman and S. Christiansen, *Vertically oriented growth of GaN nanorods on Si using graphene as an atomically thin buffer layer.* Nano Letters, 2016. **16**(6): p. 3524-3532.

55. C. Durand, C. Bougerol, J. F. Carlin, G. Rossbach, F. Godel, J. Eymery, P. H. Jouneau, A. Mukhtarova, R. Butté and N. Grandjean, *M-plane GaN/InAlN multiple quantum wells in core–shell wire structure for UV emission.* ACS photonics, 2013. **1**(1): p. 38-46.

56. A. Bugallo, L. Rigutti, G. Jacopin, F. Julien, C. Durand, X. Chen, D. Salomon, J. Eymery and M. Tchernycheva, *Single-wire photodetectors based on InGaN/GaN radial quantum wells in GaN wires grown by catalyst-free metal-organic vapor phase epitaxy.* Applied Physics Letters, 2011. **98**(23): p. 3107.

57. G. Jacopin, A. D. Bugallo, P. Lavenus, L. Rigutti, F. H. Julien, L. F. Zagonel, M. Kociak, C. Durand, D. Salomon, X. J. Chen, J. Eymery and M. Tchernycheva, *Single-wire light-emitting diodes based on GaN wires containing both polar and nonpolar InGaN/GaN quantum wells.* Applied Physics Express, 2012. **5**(1): p. 014101.

58. X. Dai, A. Messanvi, H. Zhang, C. Durand, J. Eymery, C. Bougerol, F. H. Julien and M. Tchernycheva, *Flexible light-emitting diodes based on vertical nitride nanowires.* Nano Letters, 2015. **15**(10): p. 6958-6964.

59. V. Neplokh, A. Messanvi, H. Zhang, F. H. Julien, A. Babichev, J. Eymery, C. Durand and M. Tchernycheva, *Substrate-free InGaN/GaN nanowire light-emitting diodes.* Nanoscale research letters, 2015. **10**(1): p. 1-6.

60. P. P. Paskov and B. Monemar, *2 - point defects in group-III nitrides*, in *Defects in advanced electronic materials and novel low dimensional structures*, J. Stehr, I. Buyanova and W. Chen, Editors. 2018, Woodhead Publishing. p. 27-61.

61. C. G. Van de Walle and J. Neugebauer, *First-principles calculations for defects and impurities: Applications to III-nitrides.* Journal of Applied Physics, 2004. **95**(8): p. 3851-3879.

62. S. Fritze, A. Dadgar, H. Witte, M. Bügler, A. Rohrbeck, J. Bläsing, A. Hoffmann and A. Krost, *High Si and Ge n-type doping of GaN doping-limits and impact on stress.* Applied Physics Letters, 2012. **100**(12): p. 122104.

63. L. T. Romano, C. G. Van de Walle, J. W. Ager, W. Götz and R. S. Kern, *Effect of Si doping on strain, cracking, and microstructure in GaN thin films grown by metalorganic chemical vapor deposition.* Journal of Applied Physics, 2000. **87**(11): p. 7745-7752.

64. A. Romanov and J. Speck, *Stress relaxation in mismatched layers due to threading dislocation inclination.* Applied Physics Letters, 2003. **83**(13): p. 2569-2571.

65. I. Manning, X. Weng, J. Acord, M. A. Fanton, D. W. Snyder and J. M. Redwing, *Tensile stress generation and dislocation reduction in Si-doped $Al_xGa_{1-x}N$ films.* Journal of Applied Physics, 2009. **106**(2): p. 023506.

66. H. Wang and A.-B. Chen, *Calculations of acceptor ionization energies in GaN.* Physical Review B, 2001. **63**(12): p. 125212.

67. B. Monemar, P. Paskov, G. Pozina, C. Hemmingsson, J. Bergman, S. Khromov, V. Izyumskaya, V. Avrutin, X. Li and H. Morkoç, *Properties of the main Mg-related acceptors in GaN from optical and structural studies.* Journal of Applied Physics, 2014. **115**(5): p. 053507.

68. W. Götz, R. Kern, C. Chen, H. Liu, D. Steigerwald and R. Fletcher, *Hall-effect characterization of III–V nitride semiconductors for high efficiency light emitting diodes.* Materials Science and Engineering: B, 1999. **59**(1-3): p. 211-217.

69. P. Kozodoy, H. Xing, S. P. DenBaars, U. K. Mishra, A. Saxler, R. Perrin, S. Elhamri and W. Mitchel, *Heavy doping effects in Mg-doped GaN.* Journal of Applied Physics, 2000. **87**(4): p. 1832-1835.

70. S. Brochen, J. Brault, S. Chenot, A. Dussaigne, M. Leroux and B. Damilano, *Dependence of the Mg-related acceptor ionization energy with the acceptor concentration in p-type GaN layers grown by molecular beam epitaxy.* Applied Physics Letters, 2013. **103**(3): p. 032102.

71. J. L. Lyons, A. Janotti and C. G. Van de Walle, *Effects of carbon on the electrical and optical properties of InN, GaN, and AlN.* Physical Review B, 2014. **89**(3): p. 035204.

72. R. Armitage, W. Hong, Q. Yang, H. Feick, J. Gebauer, E. R. Weber, S.

Hautakangas and K. Saarinen, *Contributions from gallium vacancies and carbon-related defects to the "yellow luminescence" in GaN.* Applied Physics Letters, 2003. **82**(20): p. 3457-3459.

73. O. Toshio and A. Masaharu, *Mechanism of yellow luminescence in GaN.* Japanese Journal of Applied Physics, 1980. **19**(12): p. 2395.

74. C. H. Seager, A. F. Wright, J. Yu and W. Götz, *Role of carbon in GaN.* Journal of Applied Physics, 2002. **92**(11): p. 6553-6560.

75. H. Liao, J. Li, T. Wei, P. Wen, M. Li and X. Hu, *First-principles study of CN point defects on sidewall surface of [0001]-oriented GaN nanowires.* Applied Surface Science, 2019. **467-468**: p. 293-297.

76. S. G. Christenson, W. Xie, Y. Y. Sun and S. B. Zhang, *Carbon as a source for yellow luminescence in GaN: Isolated CN defect or its complexes.* Journal of Applied Physics, 2015. **118**(13): p. 135708.

77. D. O. Demchenko, I. C. Diallo and M. A. Reshchikov, *Yellow luminescence of gallium nitride generated by carbon defect complexes.* Physical Review Letters, 2013. **110**(8): p. 087404.

78. M. A. Reshchikov, D. O. Demchenko, A. Usikov, H. Helava and Y. Makarov, *Carbon defects as sources of the green and yellow luminescence bands in undoped GaN.* Physical Review B, 2014. **90**(23): p. 235203.

79. M. Reshchikov, J. D. McNamara, F. Zhang, M. Monavarian, A. Usikov, H. Helava, Y. Makarov and H. Morkoç, *Zero-phonon line and fine structure of the yellow luminescence band in GaN.* Physical Review B, 2016. **94**(3): p. 035201.

80. S. Limpijumnong and d. W. C. G. Van, *Stability, diffusivity, and vibrational properties of monatomic and molecular hydrogen in wurtzite GaN.* Physical Review B, 2003. **68**(23): p. 23520.

81. N. J and V. d. W. CG, *Role of hydrogen in doping of GaN.* Applied Physics Letter, 1996. **68**(13): p. 1829-1831.

82. J. L. Lyons, A. Janotti and C. G. Van de Walle, *Shallow versus deep nature of Mg acceptors in nitride semiconductors.* Physical Review Letters, 2012. **108**(15): p. 156403.

83. S. Nakamura, T. Mukai, M. Senoh and N. Iwasa, *Thermal annealing effects on p-type Mg-doped GaN films.* Japanese Journal of Applied Physics, 1992. **31**(2B): p. L139.

84. G. Miceli and A. Pasquarello, *Energetics of native point defects in GaN: A density-functional study.* Microelectronic Engineering, 2015. **147**: p. 51-54.

85. I. C. Diallo and D. O. Demchenko, *Native point defects in GaN: A hybrid-functional study.* Physical Review Applied, 2016. **6**(6): p. 064002.

86. M. A. Reshchikov, D. O. Demchenko, J. D. Mcnamara, S. Fernandezgarrido and R. Calarco, *Green luminescence in Mg-doped GaN.* Physical Review B,

2014. **90**(3): p. 035207.

87. Q. Yan, A. Janotti, M. Scheffler and C. G. V. De Walle, *Role of nitrogen vacancies in the luminescence of Mg-doped GaN.* Applied Physics Letters, 2012. **100**(14): p. 142110.

88. J. L. Lyons, A. Alkauskas, A. Janotti and C. G. V. De Walle, *First-principles theory of acceptors in nitride semiconductors.* Physica Status Solidi B, 2015. **252**(5): p. 900-908.

89. C. Bozdog, H. Przybylinska, G. D. Watkins, V. Harle, F. Scholz, M. Mayer, M. Kamp, R. J. Molnar, A. E. Wickenden and D. D. Koleske, *Optical detection of electron paramagnetic resonance in electron-irradiated GaN.* Physical Review B, 1999. **59**(19): p. 12479-12486.

90. G. D. Watkins, K. H. Chow, P. Johannesen, L. S. Vlasenko, C. Bozdog, A. Zakrzewski, M. Mizuta, H. Sunakawa, N. Kuroda and A. Usui, *Intrinsic defects in GaN: What we are learning from magnetic resonance studies.* Physica B-Condensed Matter, 2003. **340**: p. 25-31.

91. K. H. Chow, L. S. Vlasenko, P. Johannesen, C. Bozdog, G. D. Watkins, A. Usui, H. Sunakawa, C. Sasaoka and M. Mizuta, *Intrinsic defects in GaN. I. Ga sublattice defects observed by optical detection of electron paramagnetic resonance.* Physical Review B, 2004. **69**(4): p. 045207.

92. H. J. Von Bardeleben, J. L. Cantin, H. Vrielinck, F. Callens, L. Binet, E. Rauls and U. Gerstmann, *Nitrogen split interstitial center* $(N\text{-}N)_n$ *in GaN : High frequency EPR and ENDOR study.* Physical Review B, 2014. **90**(8): p. 085203.

93. M. Linde, S. J. Uftring, G. D. Watkins, V. Harle and F. Scholz, *Optical detection of magnetic resonance in electron-irradiated GaN.* Physical Review B, 1997. **55**(16): p. 65911.

94. B. G. Yacobi and D. B. Holt. *Cathodoluminescence microscopy of inorganic solids*. in *Springer US*. 1990.

95. K. Kojima, S. Takashima, M. Edo, K. Ueno, M. Shimizu, T. Takahashi, S. Ishibashi, A. Uedono and S. F. Chichibu, *Nitrogen vacancies as a common element of the green luminescence and nonradiative recombination centers in Mg-implanted GaN layers formed on a GaN substrate.* Applied Physics Express, 2017. **10**(6): p. 061002.

96. Y. H. Kwon, S. K. Shee, G. H. Gainer, G. H. Park, S. J. Hwang and J. J. Song, *Time-resolved study of yellow and blue luminescence in Si- and Mg-doped GaN.* Applied Physics Letters, 2000. **76**(7): p. 840-842.

97. J. H. Kim, Y. H. Ko, J. H. Cho, S. H. Gong, S. M. Ko and Y. H. Cho, *Toward highly radiative white light emitting nanostructures: A new approach to dislocation-eliminated GaN/InGaN core-shell nanostructures with a negligible polarization field.* Nanoscale, 2014. **6**(23): p. 14213-14220.

98. S. H. Lim, Y. H. Ko, C. Rodriguez, S. H. Gong and Y.-H. Cho, *Electrically*

driven, phosphor-free, white light-emitting diodes using gallium nitride-based double concentric truncated pyramid structures. Light Science & Applications, 2016. **5**(2): p. e16030.

99. J. Ledig, X. Wang, S. Fündling, H. Schuhmann, M. Seibt, U. Jahn, H. H. Wehmann and A. Waag, *Characterization of the internal properties of InGaN/GaN core–shell LEDs.* Physica Status Solidi A, 2016. **213**(1): p. 11-18.

100. X. Wang, U. Jahn, M. Mandl, T. Schimpke, J. Hartmann, J. Ledig, M. Straßburg, H. H. Wehmann and A. Waag, *Growth and characterization of mixed polar GaN columns and core–shell LEDs.* Physica Status Solidi A, 2015. **212**(4): p. 727-731.

101. T. Schimpke, M. Mandl, I. Stoll, B. Pohl Klein, D. Bichler, F. Zwaschka, J. Strube Knyrim, B. Huckenbeck, B. Max, M. Müller, P. Veit, F. Bertram, J. Christen, J. Hartmann, A. Waag, H.-J. Lugauer and M. Strassburg, *Phosphor-converted white light from blue-emitting InGaN microrod LEDs.* Physica Status Solidi A, 2016. **213**(6): p. 1577-1584.

102. Y. H. Ra, R. Navamathavan, S. Kang and C. R. Lee, *Different characteristics of InGaN/GaN multiple quantum well heterostructures grown on m- and r-planes of a single n-GaN nanowire using metalorganic chemical vapor deposition.* Journal of Materials Chemistry C, 2014. **2**(15): p. 2692-2701.

103. M. D. Brubaker, K. L. Genter, A. Roshko, P. T. Blanchard, B. T. Spann, T. E. Harvey and K. A. Bertness, *UV LEDs based on p-i-n core-shell AlGaN/GaN nanowire heterostructures grown by N-polar selective area epitaxy.* Nanotechnology, 2019. **30**(23): p. 234001.

104. Y. H. Ra, S. Kang and C. R. Lee, *Ultraviolet light-emitting diode using nonpolar AlGaN core–shell nanowire heterostructures.* Advanced Optical Materials, 2018. **6**(14): p. 1701391.

105. J. R. Chang, S. P. Chang, Y. J. Li, Y. J. Cheng, K. P. Sou, J. K. Huang, H. C. Kuo and C. Y. Chang, *Fabrication and luminescent properties of core-shell InGaN/GaN multiple quantum wells on GaN nanopillars.* Applied Physics Letters, 2012. **100**(26): p. 261103.

106. B. Radha, D. Jayaraj, G. U. Kulkarni, S. Heun, D. Ercolani and L. Sorba, *Large-area ohmic top contact to vertically grown nanowires using a free-standing Au microplate electrode.* ACS Applied Materials & Interfaces, 2012. **4**(4): p. 1860-1864.

107. H. P. T. Nguyen, K. Cui, S. Zhang, M. Djavid, A. Korinek, G. A. Botton and Z. Mi, *Controlling electron overflow in phosphor-free InGaN/GaN nanowire white light-emitting diodes.* Nano Letters, 2012. **12**(3): p. 1317-1323.

108. H.-W. Lin, Y.-J. Lu, H.-Y. Chen, H.-M. Lee and S. Gwo, *InGaN/GaN nanorod array white light-emitting diode.* Applied Physics Letters, 2010. **97**(7): p. 073101.

109. F. Qian, S. Gradečak, Y. Li, C.-Y. Wen and C. M. Lieber, *Core/multishell nanowire heterostructures as multicolor, high-efficiency light-emitting diodes.* Nano Letters, 2005. **5**(11): p. 2287-2291.

110. R. Koester, J. S. Hwang, D. Salomon, X. Chen, C. Bougerol, J. P. Barnes, D. L. S. Dang, L. Rigutti, A. de Luna Bugallo and G. Jacopin, *M-plane core–shell InGaN/GaN multiple-quantum-wells on GaN wires for electroluminescent devices.* Nano Letters, 2011. **11**(11): p. 4839-4845.

111. M. Tchernycheva, A. Messanvi, A. de Luna Bugallo, G. Jacopin, P. Lavenus, L. Rigutti, H. Zhang, Y. Halioua, F. H. Julien, J. Eymery and C. Durand, *Integrated photonic platform based on InGaN/GaN nanowire emitters and detectors.* Nano Letters, 2014. **14**(6): p. 3515-3520.

112. H. Sekiguchi, K. Kishino and A. Kikuchi, *Emission color control from blue to red with nanocolumn diameter of InGaN/GaN nanocolumn arrays grown on same substrate.* Applied Physics Letters, 2010. **96**(23): p. 231104.

113. *Closed coupled showerhead® CCS and NOVO systems for R&D; https://www.Aixtron.Com/en/products/compound-semiconductors-mocvd/ccs-ft*.

114. *Aixtron 3x2FT close-coupled showerhead system manual.*

115. *Thermal evaporation: Overview; https://angstromengineering.com/tech/resistive-thermal-evaporation/*

116. P. Dogan, C. Chèze and R. Calarco, *III–V semiconductor nanowires: Nitrides (N-based; III-N)*, in *Semiconductor nanowires*. 2015, Woodhead Publishing. p. 125-145.

117. P. D. Nellist, *Scanning transmission electron microscopy*, in *Springer handbook of microscopy*, P. W. Hawkes and J. C. H. Spence, Editors. 2019, Springer International Publishing: Cham. p. 2.

118. V. C.A. and M. A.M., *Focused ion beam microscopy and micromachining.* MRS BULLETIN, 2007. **32** (5): p. 389-399.

119. S. Reyntjens and R. Puers, *A review of focused ion beam applications in microsystem technology.* Journal of Micromechanics and Microengineering, 2001. **11**(4): p. 287–300.

120. A. M. Herrmann, K. Ritz, N. Nunan, P. L. Clode, J. Pett-Ridge, M. R. Kilburn, D. V. Murphy, A. G. O'Donnell and E. A. Stockdale, *Nano-scale secondary ion mass spectrometry — a new analytical tool in biogeochemistry and soil ecology: A review article.* Soil Biology and Biochemistry, 2007. **39**(8): p. 1835-1850.

121. G. Betz and K. Wien, *Energy and angular distributions of sputtered particles.* International Journal of Mass Spectrometry & Ion Processes. **140**(1): p. 1-110.

122. G. M. Guryanov, *Cluster ion emission from nitrogen-doped GaAs and optimization of SIMS conditions for nitrogen analysis.* Applied Surface Science,

2004. **231-232**: p. 817-820.

123. P. Hoppe, S. Cohen and A. Meibom, *Nanosims: Technical aspects and applications in cosmochemistry and biological geochemistry.* Geostandards and Geoanalytical Research, 2013. **37**(2): p. 111-154.

124. E. Chatzitheodoridis, G. Kiriakidis and I. Lyon, *Secondary ion mass spectrometry and its application to thin film characterization*, in *Handbook of thin films*. 2002, Elsevier. p. 637-683.

125. *Introduction to the instrumentation Nano-SIMS 50/50L: Secondary ion mass spectrometer for trace element and isotope analysis at sub-micron resolution.*

Chapter 3

Growth of GaN nanorods

3.1 Introduction

GaN-based nanorods, due to their direct and tuneable bandgap, have wide applications in optoelectronic devices. GaN nanorods grown by metalorganic chemical vapour deposition (MOCVD) have been achieved by catalyst-assisted growth [1-3], selective-area growth [4-7], and self-assembled growth [8-15]. However, in the catalyst-assisted growth, the introduction of the metal catalyst may cause contamination which would degrade device performance [8]. On the other hand, in selective area growth, the fabrication of the dielectric mask is complicated and time-consuming. Therefore, self-assembled nanorod growth is considered an optimal method due to its catalyst-free and minimal substrate preparation requirements. This approach already has already been shown for device applications that do not demand precise positionings, such as single nanorod LEDs [9] and flexible nanorod LED arrays [10, 11].

In this chapter, we study wafer-scale, self-assembled growth of GaN nanorods, in particular the effects of pre-growth and growth conditions. The experiment details are described in section 3.2. The nitridation treatment before growth is discussed in section 3.3. We found nitridation has a large effect on the morphology, polarity, and optical properties of the GaN nanorods. The study of growth parameters including silane injection rate, growth temperature, and growth time are discussed in section 3.4. The summary of this chapter is in section 3.5.

3.2 Experiments

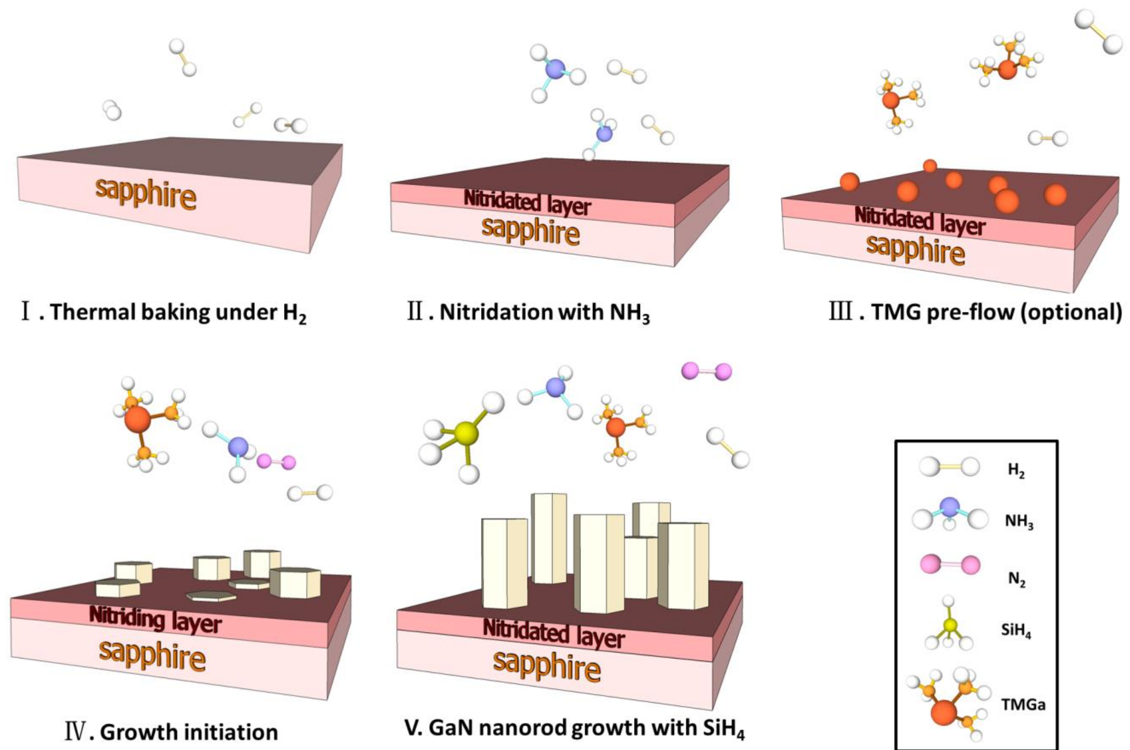

Figure 3.1 Illustration for the self-assembled growth of nanorods used in the work.

The GaN self-assembled nanorods were grown on (0001) sapphire substrates in an Aixtron MOCVD closed-coupled showerhead system. The growth process is illustrated in figure 3.1, where ammonia (NH_3), trimethylgallium (TMGa), and silane (SiH_4) were used as the nitrogen, gallium, and n-type dopant sources, respectively. The chamber pressure was maintained at 200 mbar with 10000 sccm total gas injection. (i). Prior to growth, a 20-minute substrate baking was performed under H_2 flow at 1050°C for surface decontamination. (ii). After thermal baking, nitridation was conducted for 300s using an NH_3 flow of 3000 sccm at the same temperature. (iii). Just prior to the commencement of growth, the carrier gas was switched from H_2 to an H_2/N_2 mixture with a ratio of 2:1 to achieve a higher vertical growth rate [16]. (iv). A 10 seconds initiation stage was used to start the growth through simultaneous injection of TMGa (13.65 mmol/min) and NH_3 (25 sccm) at 1050°C. (v). Subsequently, the growth continued for a further 300 s with a reduced NH_3 flow of 15 sccm and 200 nmol/min of SiH_4 flow. SiH_4 was required to promote vertical growth by forming a SiN_x layer on the nanorod sidewalls [17]. It should be noted that the V/III ratio (V/III =5) used here was very low compared with conventional planar growth.

The morphology of the nanorods was investigated using a FEI Helios 600 Nanolab scanning electron microscope (SEM). The crystal structure and polarity were investigated in aberration-corrected scanning transmission electron microscopy (STEM) using a JEOL ARM 200F. Nanorod lamellae were prepared for the TEM experiment by FIB as described in Chapter 2. The nanorod optical properties were examined through high-resolution cathodoluminescence (CL) spectroscopy using a FEI Verios 460 SEM equipped with a Gatan MonoCL4 Elite system.

3.3 Studies of surface nitridation

In planar GaN epitaxy on sapphire, nitridation and specialised buffer layer growth are developed to control the polarity of the film [12, 13]. During nitridation, ammonia reacts with sapphire such that nitrogen atoms diffuse into the surface of the sapphire substrate to form a thin $Al_xN_yO_z$ layer and may also convert the polarity of the substrate [14]. Subsequently, a thin GaN or AlN buffer layer can be successfully grown on it. The polarity of the GaN topmost layer is decided both by nitridation parameters and buffer layer growth parameters: a low growth temperature helps the layer maintain group III-polar surface adopted from the $Al_xN_yO_z$ layer; while a high growth temperature may lead to decomposition of $Al_xN_yO_z$ and result in N-polar film [15]. Without incorporating a proper nitridation process during epitaxy, the resulting film has a rough morphology, high defect densities, and polarity inversion domains [18-21].

However, the effects of nitridation are not well understood in the growth of nanostructures which happen to be more sensitive to polarity due to their size [22, 23]. To date, only a few reports studied the nitridation effects on morphology, band edge, and yellow emission properties [24]. Its effects on polarity are still unclear. To fully understand the effects of nitridation on GaN nanorods, this section presents a detailed study on how the different duration of nitridation gradually changes the morphology and related optical properties. We found that nitridation plays a strong role in determining the polarity of the nanorods and an appropriate nitridation also improves their structural and optical properties.

3.3.1 Nitridation effects on crystal morphology

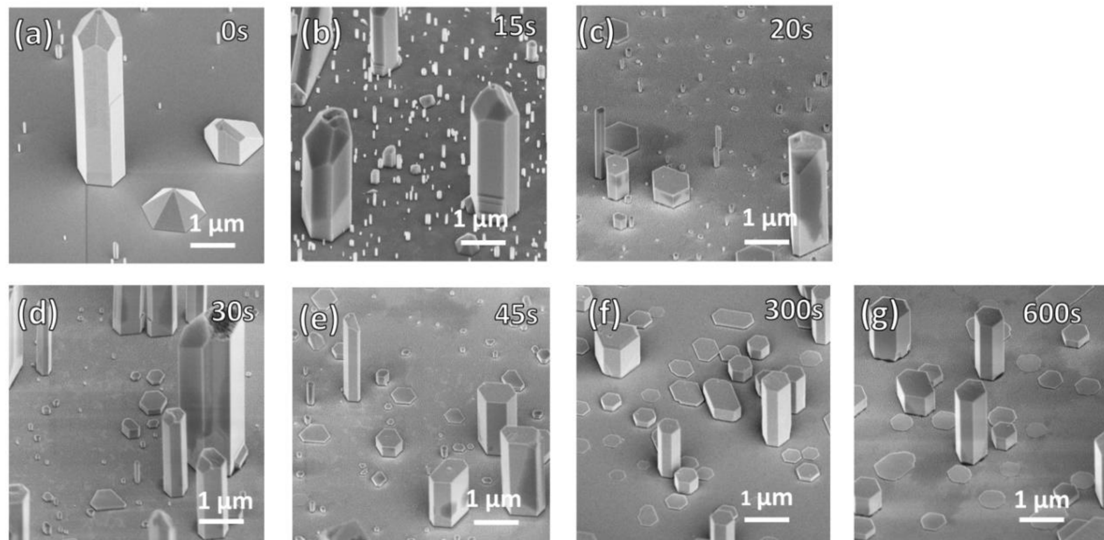

Figure 3.2 (a-g) 45° SEM images of samples with nitridation time ranging from 0 to 600 s. The nanorod morphology changes from pointed to flat tops with increasing nitridation time.

Figure 3.2 shows the SEM images of the GaN nanorods grown with nitridation duration from 0 to 600 s. With increasing nitridation time, both the nanorod morphology and size change dramatically. In samples with shorter nitridation times (figure 3.2 *a* and *b*), most nanorods have a pyramidal-top, whereas for samples that have been nitridated for longer times (figure 3.2 *f* and *g*), regular flat tops become dominant. The diameter of the nanorod is not consistent in the short nitridated sample that both very small and large diameter nanorods coexist, while in the longer nitridated sample, the diameter distribution is more uniform. This morphology transformation could be attributed to changes in polarity [25]. It has been commonly reported that pointed tops in nanorods are attributed to Ga-polar growth while flat tops are related to N-polar growth. It is also interesting to note that some nanorods have a combination of both pointed and flat tops in the sample grown with short nitridation time (figure 3.2 *d*), an indication that they may be mixed polarity.

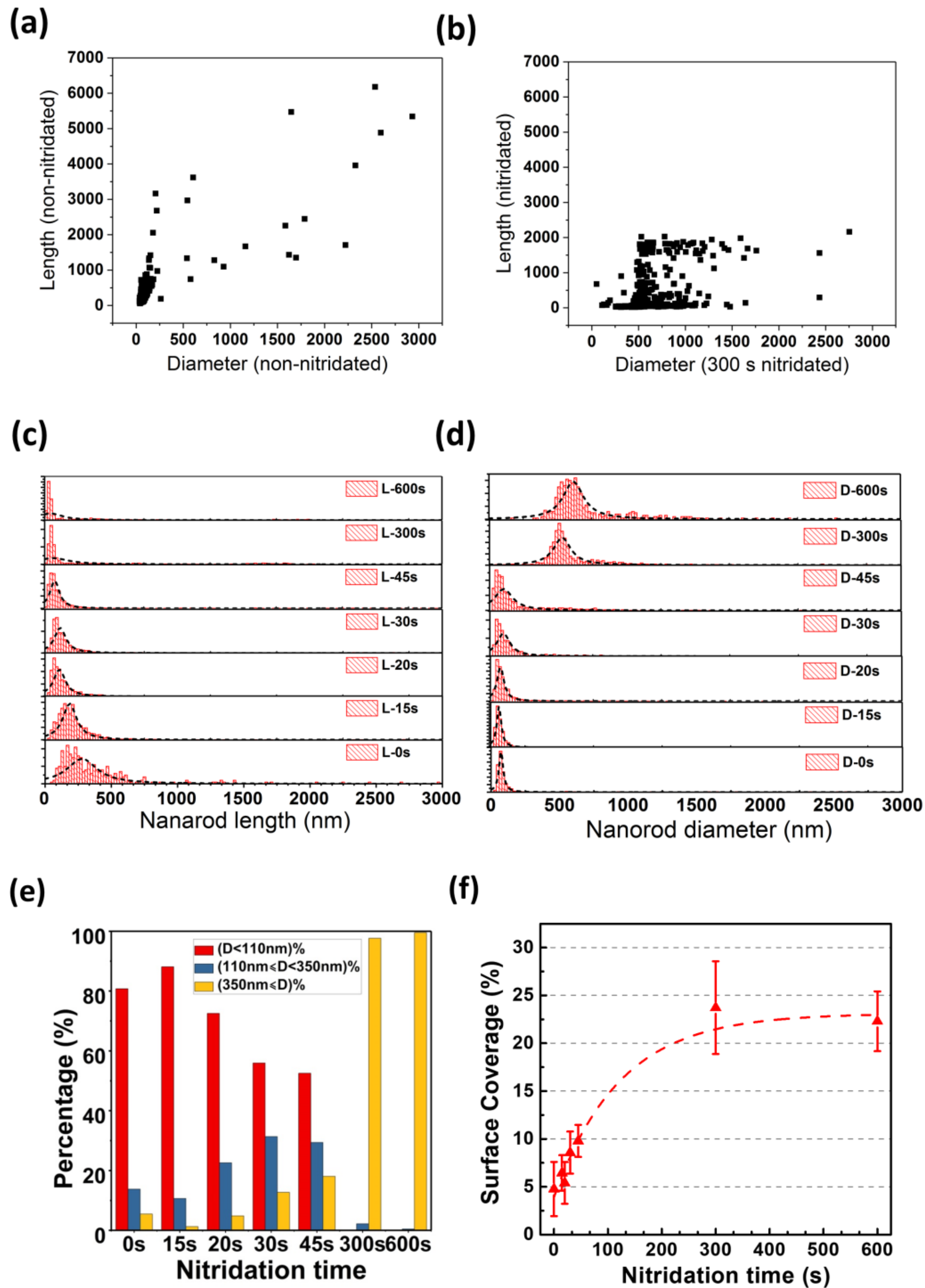

Figure 3.3 Statistical studies of nanorod morphology with varied nitridation durations: (a, b) Scatter plots showing nanorod length vs. diameter for the non-nitridated and nitridated samples, respectively. (c, d) Histogram distribution of nanorod length and diameter with different nitridation duration, respectively. (e) Histogram showing the percentage of nanorods with different diameters for various nitridation times. (f) Plot of sapphire surface coverage with nitridation time.

A statistical study of nanorod morphology was conducted to better appreciate the

results found from the SEM images. The scatter plots of both non-nitridated and nitridated samples are shown in figure 3.3 (a) and (b). The nanorod diameter and length are not correlated, i.e. thinner nanorods are not significantly taller. This suggests that the growth of nanorods under these growth conditions are not within a diffusion-limited regime where diameter and length are inversely correlated [26].

The histogram of nanorod diameter and length are shown in figure 3.3 (c) and (d), respectively. As the nitridation time increases, the nanorod length becomes shorter with narrower FWHM, whereas the diameter becomes larger. This trend is clearer when we classify them into three diameter groups. As shown in figure 3.3 (e), mostly thin rods (D<110 nm) are formed at shorter nitridation time (15 s), and shift to mid-size (110≤D<350 nm) around 30-45 s, and finally only large diameter rods (D≥350 nm) appear after 300 s of nitridation time. We also found at longer nitridation time, GaN crystals cover larger areas of the substrate surface (figure 3.3 *f*). The expansion in diameter and surface coverage could be related to the $Al_xN_yO_z$ layer, which could reduce the interfacial energy and lattice mismatch between the substrate and nanorod.

3.3.2 Nitridation effects on polarity

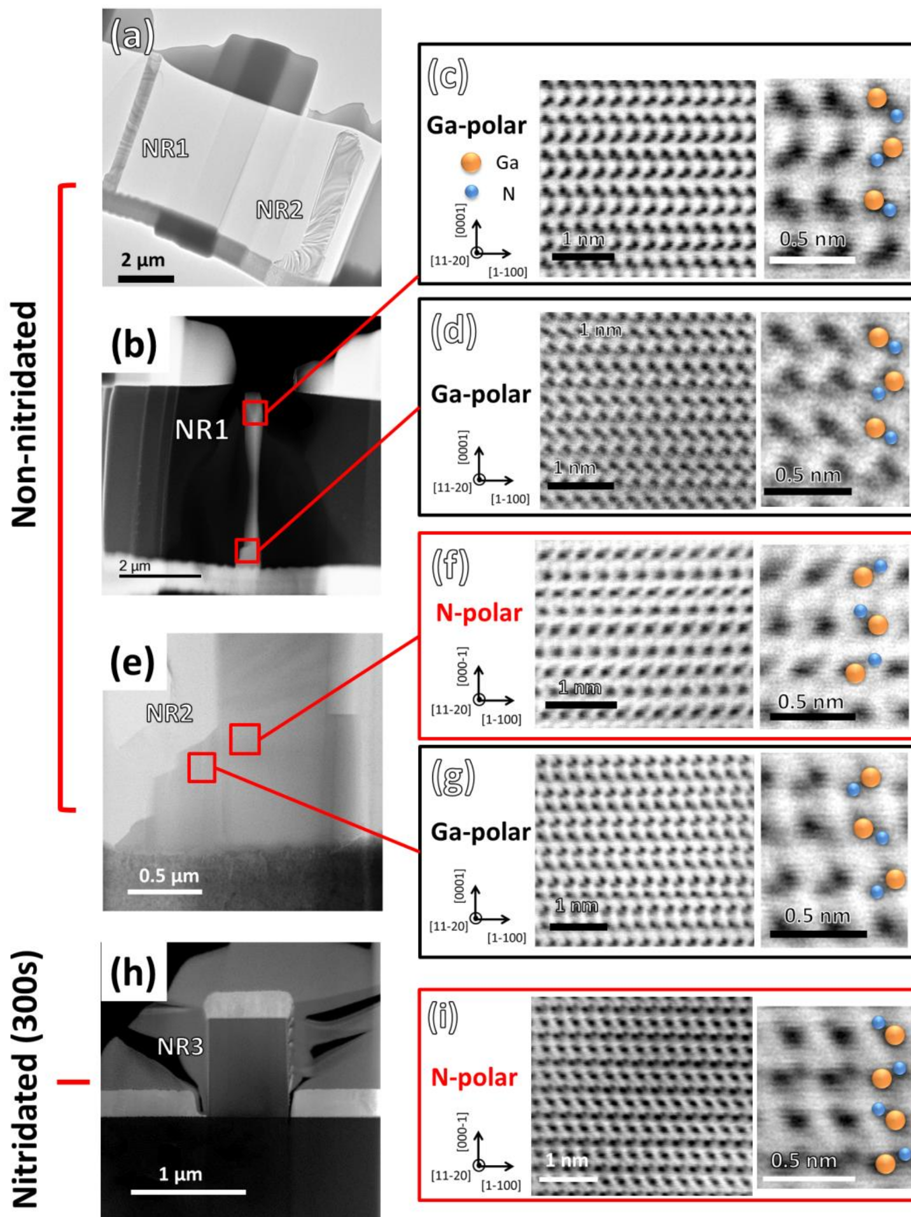

Figure 3.4 Polarity determination of nitridated and non-nitridated samples using C_S-corrected TEM: (a) STEM image of nanorods 1 and 2 from the non-nitridated sample. (b) STEM image of nanorod 1. (c, d) High magnification annular bright-field image at the top and bottom part of nanorod 1. An asymmetric atomic dumb-bell image reveals the larger Ga atoms on top of the double atom layers (Ga-polar). (e) STEM image of nanorod 2 with a pronounced lateral growth at the base region. (f) High magnification annular bright-field image of the main body region of nanorod 2 (indicated by the right red square in figure *e*) demonstrating N-polarity. (g) The lateral section of nanorod 2 (indicated by the left red square in figure *e*) demonstrating Ga-polarity. (h) STEM image of nanorod 3 (nitridated sample). (i) High magnification annular

bright-field image of nanorod 3 showing N-polarity. All STEM images are all taken along the GaN [11-20] zone axis.

To investigate the effect of nitridation on polarity, we examined several nanorods using C_S-corrected TEM. For the non-nitridated sample, the TEM lamella contains two nanorods that are in close proximity to each other. For nanorod 1 (NR1), both the tip and base are Ga-polar, as shown by the atomic dumbbells [27] in figure 3.4 (c) and (d). For nanorod 2 (NR2), the middle part is N-polar (figure 3.4 *f*), but the staircase-like footage region is Ga-polar (figure 3.4 *g*). These results show that without nitridation two types of nanorods may form: Ga-polar and mixed polarity. Nanorods that nucleate directly on the substrate would be Ga-polar, which is consistent with other reports [24, 28]. For mixed polarity nanorods, the Ga-polar domains nucleate directly on sapphire while the N-polar domains on the partially nitridated surface, which could be due to the supply of NH_3 during the growth that might still react with the sapphire substrate to form $Al_xN_yO_z$ layer even at a small flow rate (15 sccm). The $Al_xN_yO_z$ layer is not stable at high temperatures and would be converted into N-polar with Al-N bonds [15]. If the two domains with opposite polarity are in close proximity to each other, then with continuous growth, they would coalesce and form the mixed-polarity nanorod.

In contrast, for nanorod 3 (figure 3.4 *h*) that is nitridated for 300 s, no inversion domain is found. The atomic dumbbell images of this nanorod are shown in Figure 3.4 (i), indicating N-polarity, which is consistent with other reports that nanorod polarity after nitridation is N-polar [24].

3.3.3 Cathodoluminescence results

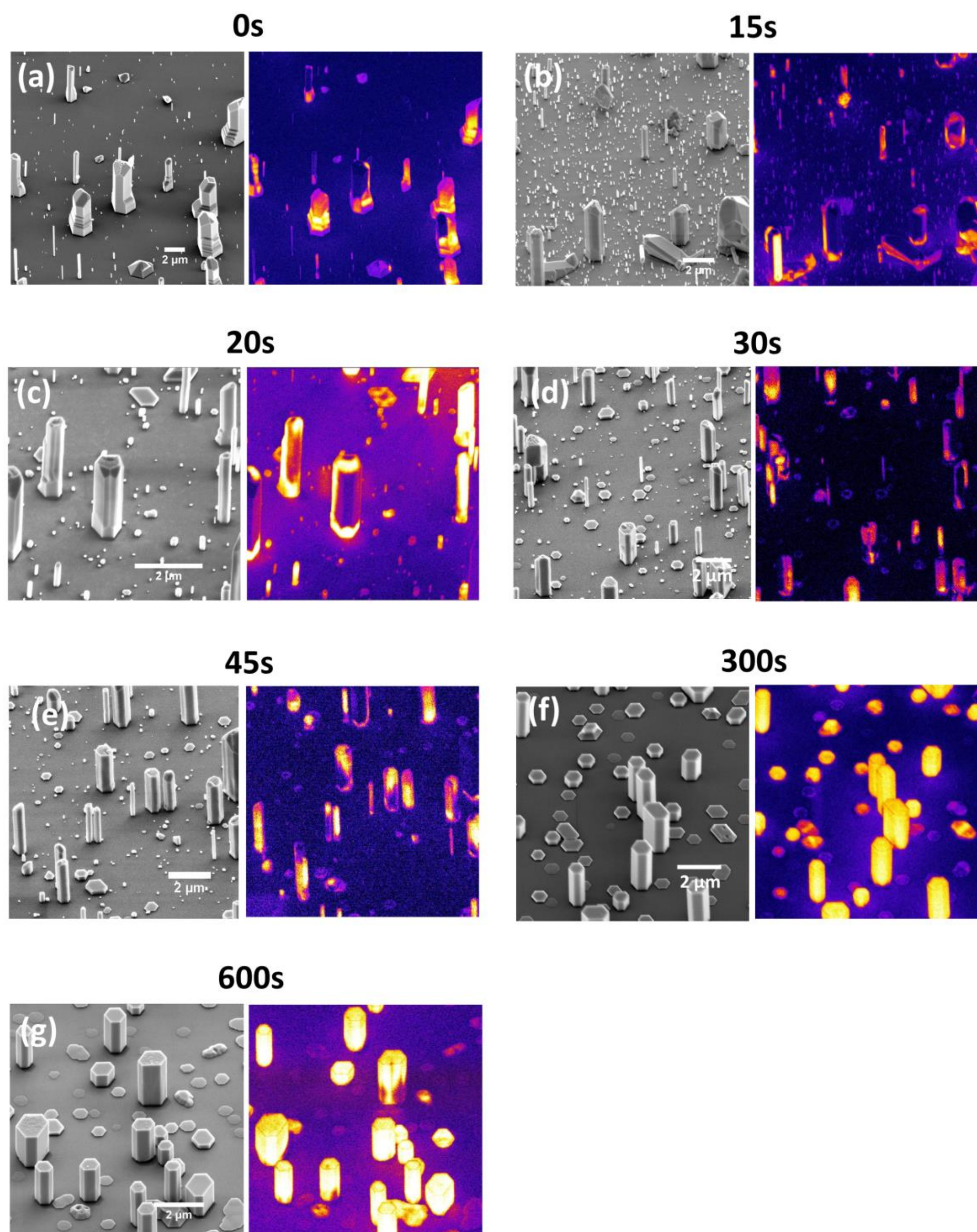

Figure 3.5 (a-g) 45° SEM and corresponding panchromatic CL images of nanorods grown on sapphire substrate with various nitridation time from 0 to 600s.

The introduction of the nitridation step also improves the nanorod optical properties. As shown in figure 3.5, the CL distribution of the nanorod has changed from non-

uniform to uniform luminescence with longer nitridation time. In a non-nitridated sample (figure 3.5 *a*), several facets are bright, while other facets are partially bright with irregular dark areas, and an indication that non-radiative defects are present. This non-uniform luminescence distribution persists in short nitridation time samples (t < 45 s), and largely improved in longer nitridation time samples (300- 600 s).

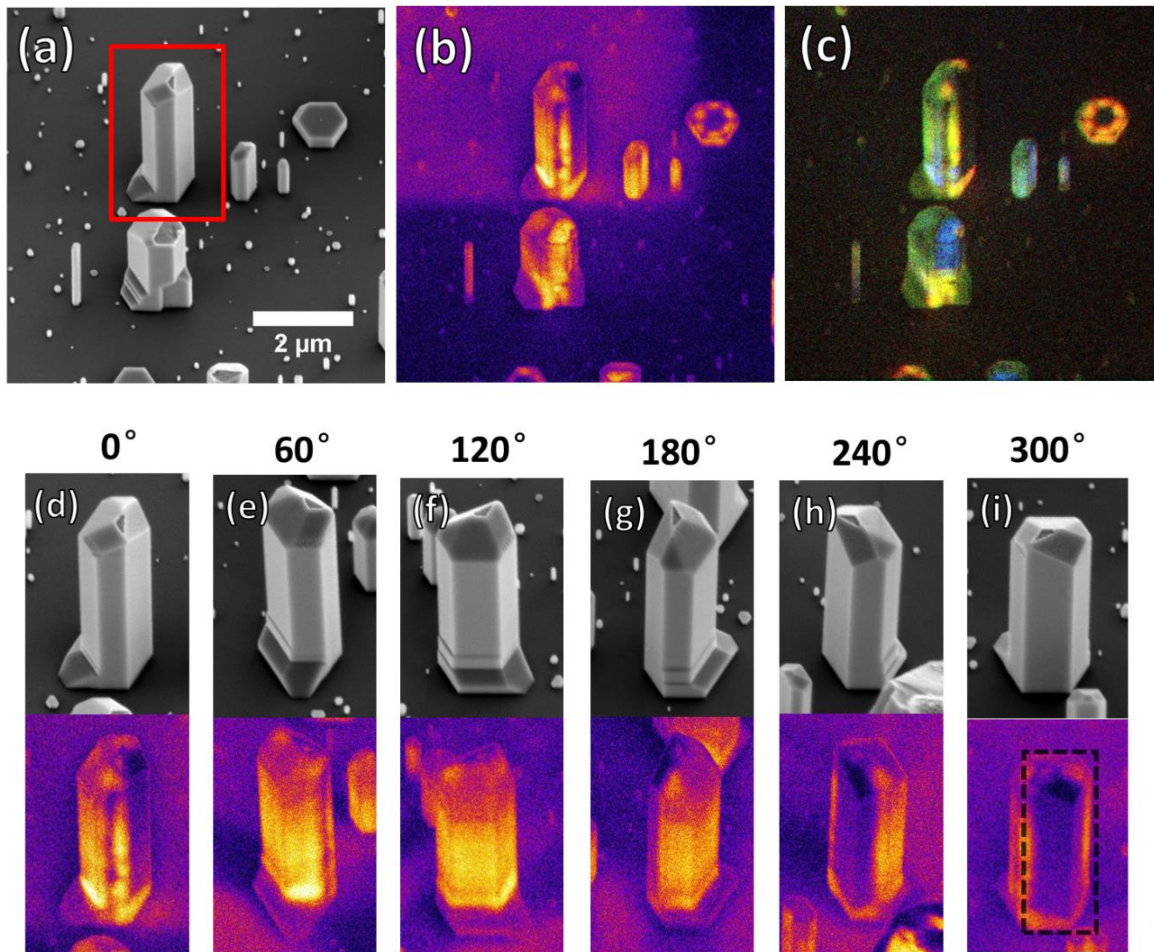

Figure 3.6 (a-c) 45° SEM, corresponding panchromatic CL, and RGB color filtered images of samples grown with 20 s nitridation time. (d-i) SEM and panchromatic CL images of a nanorod (indicated in red square in figure 3.6 *a*) viewed from different rotation angles ranging from 0 to 300 °.

In order to be able to image other facets, we rotate the samples to view the CL images from different directions. The images of a nanorod from the sample grown with 20 s nitridation duration are shown in figure 3.6 rotated from 0 to 300°. The colour filtered images show that the luminescence from the nanorod is mainly near-band emission and yellow luminescence. At 0°, the facet on the right side of the nanorod shows a lack of

luminescence (figure 3.6 *d*). With a continual 60° rotation so that we can image all the side facets, it is clear from figure 3.6 (d) to (i) that two of the six sidewalls do not have any luminescence. The top regions of these two facets are also non-luminescent and from these images, there is no clear relationship between these dark areas and specific crystal facets. The rotated CL imaging can be used in constructing a 3D CL distribution of the nanorod, which can further help to illustrate the optical properties of the single nanorod.

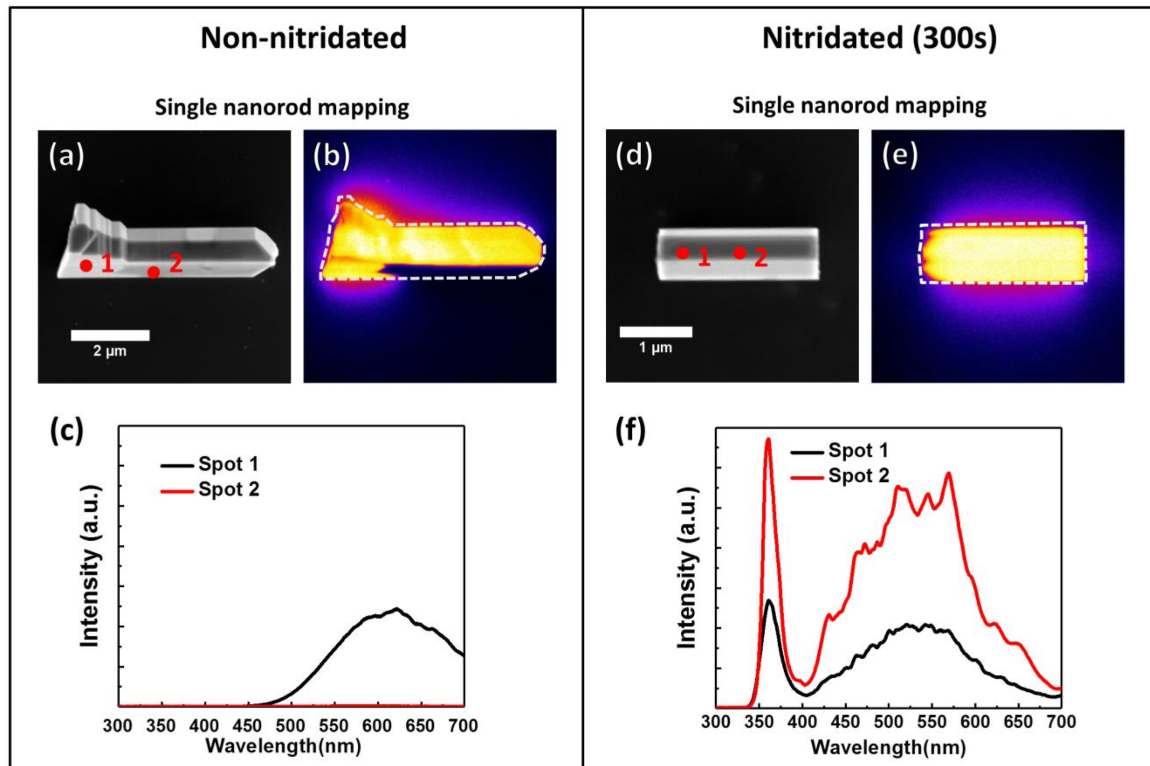

Figure 3.7 Optical properties of (a-c) a non-nitridated nanorod and (d-f) a 300 s nitridated nanorod. (a, d) SEM image of a single nanorod. (b, e) Panchromatic CL image of figure *a* and *d*, respectively. (c, f) CL spectra extracted from the two spots of each sample indicated in figure *a* and *d*.

A detailed optical properties comparison between nitridated and non-nitridated sample are shown in figure 3.7. For the non-nitridated sample (figure 3.7 *b*), the luminescence signal is unevenly distributed and some parts of the nanorods have no luminescence (figure 3.7 *a*, spot 2). The luminescence from the bottom end of the nanorod (figure 3.7 *a*, spot 1) is dominated by strong yellow luminescence centered around 600 nm, and no visible near band edge emission is observed. The lack of band edge emission could be related to enhanced carbon impurity incorporation during the

growth [29]. The deterioration of the optical property is also found on certain sidewalls (such as spot 2 shown in figure 3.7 *a*), where there is a complete lack of luminescence. This could be related to enhanced incorporation of impurities [29] or point defects that act as non-radiative recombination centers. However, more work is required to conclusively address this issue.

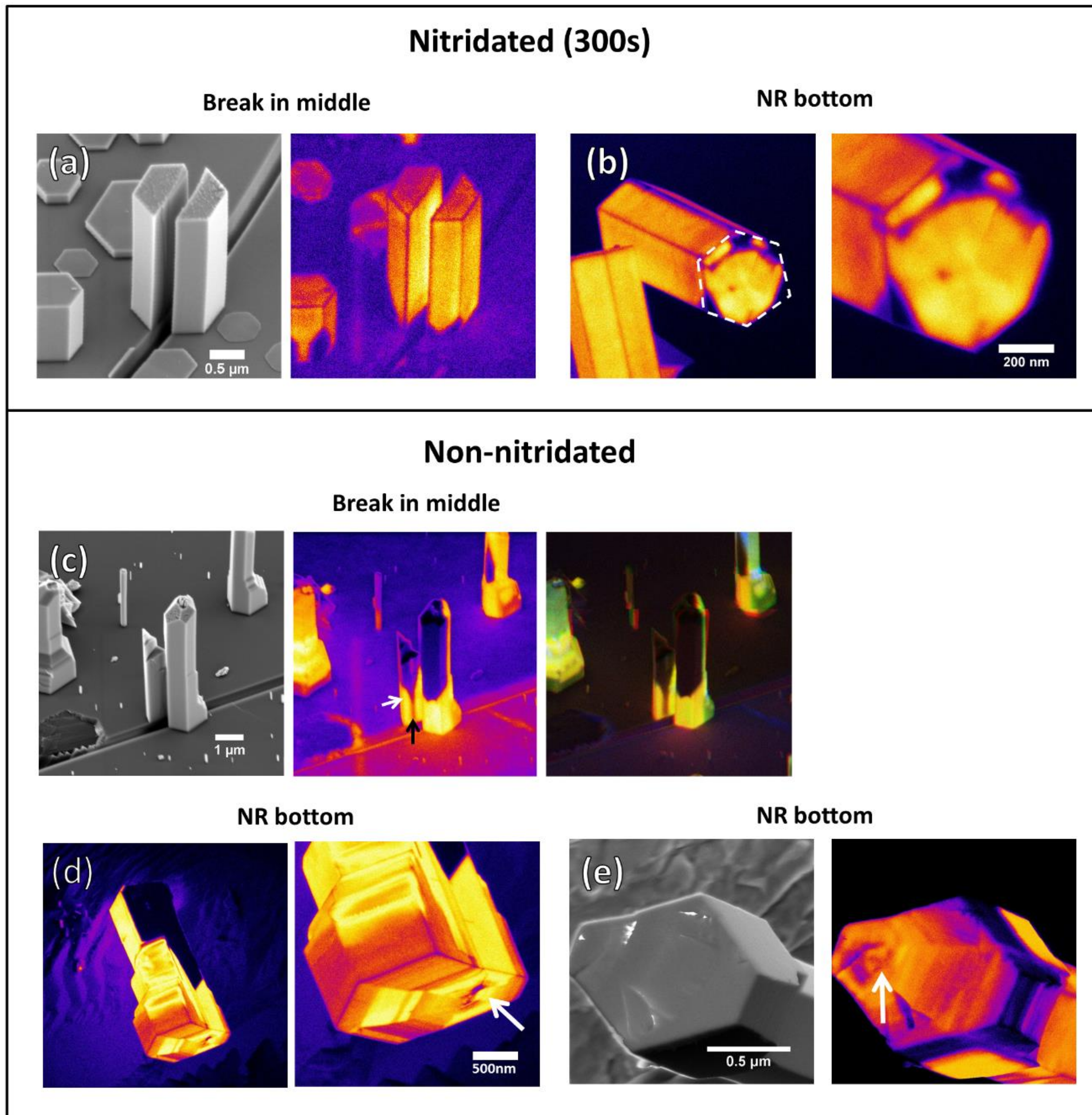

Figure 3.8 SEM and panchromatic CL images focused at the middle/bottom areas of both non-nitridated and 300 s nitridated samples. (a) SEM and panchromatic CL images of a nitridated nanorod cleaved along its length, revealing homogenous luminescence inside. (b) The bottom part of a nitridated nanorod showing homogenous luminescence, except at the bottom corners. The dotted line is a guide indicating the nanorod shape. (c) SEM image, panchromatic CL image, and integrated CL image using RGB filters of a non-nitridated nanorod cleaved along its length. The middle section of the nanorod (indicated by the black arrow) has no

luminescence surrounded by a region with relatively bright luminescence (indicated by the white arrow). (d, e) CL images of a non-nitridated nanorod, showing pronounced lateral growth facets resulting in facets with a range of different contrast. The white arrow indicates the defective nucleation area.

After a 300 s nitridation treatment, the panchromatic image of a single nanorod (figure 3.7 *e*) shows a homogenous luminescence along the nanorod length, except for a small region at the bottom of the nanorod that shows a patterned-like emission which will be discussed in the next chapter. From the spectra in figure 3.7 (f), we see that near band edge emission is enhanced along the nanorod, indicating an improvement in the crystal quality. Although yellow luminescence is still visible, its relative intensity compared to near band edge emission is reduced. Fluctuations observed in the spectra could be related to either whispering gallery or Fabry-Pérot modes supported in the nanorod, but overall, the spectra highlight an improvement in nanorod optical properties and uniformity.

To further understand the origin of the non-uniform CL signal from the non-nitridated sample, we conducted the CL imaging on nanorod cross-sections. Commonly for CL characterization [30], we only observe regions near the surface, which provide limited information related to growth. However, if we capture the CL images of the nanorod cross-sections, they can provide spatially-resolved information about the nucleation and growth. Nanorod cross-sections (figure 3.8 *a* and *c*) were prepared by cleaving the wafer using a diamond scriber.

For the 300 s nitridated sample, a nanorod that has been split from cleaving (figure 3.8 *a*) shows homogenous luminescence at both the exterior and interior, further suggesting its superior optical properties and high crystalline quality due to the nitridation process. The base of the rod also shows dark corners typical of the nitridated samples (figure 3.8 *b*) that will be discussed in chapter 4.

For the non-nitridated nanorod, as shown in figure 3.8 (c), we found an absence of luminescence from the split cross-section both inside the rod and at the surface, except for the region near the base. We attributed the dimmer CL region in the middle of the nanorod (indicated by the black arrow) to unfavorable nanorod nucleation directly on the sapphire, which leads to a higher density of defects which act as non-radiative recombination centers. The surrounding part of the rod (indicated by a white arrow in the middle image) shows strong yellow luminescence (as shown by the left image in

figure 3.8 *c*), clearly indicating a much-improved quality compared with the middle region of the nanorod. The formation of this part is related to radial growth, but the reason for its incomplete coverage over the nanorod is still unknown. The expansion of the dark-region towards the top of the nanorod also shows how the initial nucleation can affect the nanorod quality even much later in growth.

The base of other nanorods from the same sample (figure 3.8 *d* and *e*) shows a growth-ring-like distribution of luminescence or a spider web-like luminescence contrast, which may be related to faceting or polarity change resulting from radial growth. It is possible that the defective center at the base (indicated by the white arrow) starts off as the nucleation site. The non-uniform luminescence of this cross-section also coincides with the mixed-polarity phenomenon found in TEM analysis and inversion domains may form due to multiple or non-uniform radial growth. We postulate that nitridation affects the early stages of nucleation, which has dramatic influence on subsequent growth of the nanorod and its structural and optical properties. Without a proper pre-growth treatment, nucleation results in poor luminescence both at the inner and outer part of the nanorod.

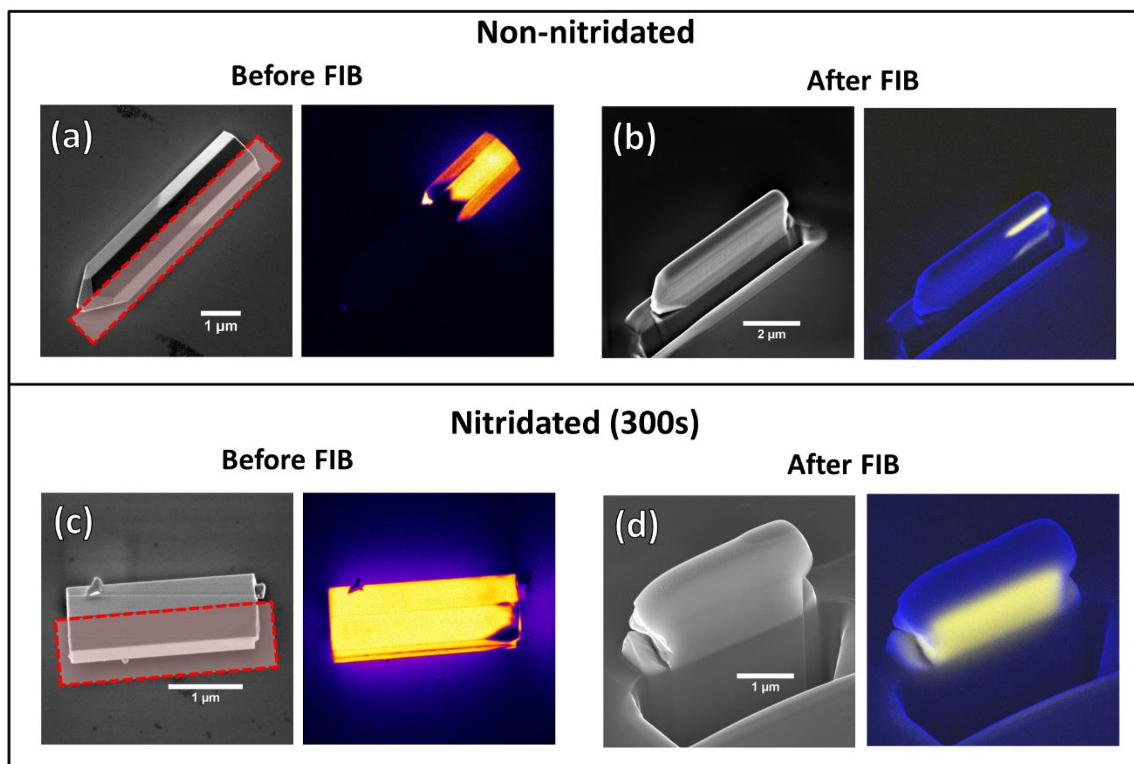

Figure 3.9 SEM and panchromatic CL images of the nanorod cross-sections sliced by FIB: (a, b) SEM and corresponding panchromatic CL of a non-nitridated nanorod before and after FIB

milling. The milling section was along the growth direction indicated by the red rectangle. (c, d) SEM and corresponding panchromatic CL of a nitridated nanorod before and FIB milling along the growth direction (red dash rectangle).

Another way to split the nanorod instead of the more random way of cleaving is through FIB milling, which will also result in more accurate control of the cleaving position. As shown in figure 3.9 (a), the non-nitridated nanorod has a pencil-like shape while the luminescence is only observed at the bottom part of the nanorod. After milling (figure 3.9 *b*), we found the luminescence is only at the surface, while the core of this nanorod is dark. In contrast, for the 300 s nitridated sample, the luminescence is homogenous both at the surface and in the nanorod core as shown in figure 3.9 (d), after milling to expose this region. Results from FIB milling corroborate that the nitridation helps to improve the optical properties of the nanorods.

3.3.4 Summary on nitridation

In conclusion, we have studied the influence of nitridation time on the morphology, optical properties, and polarity of GaN nanorods. With appropriate nitridation, the nanorod morphology transforms from a pyramidal top to a flat top accompanied by increased GaN surface coverage of the substrate. We found that mixed polarity exists in non-nitridated samples, while the nitridated nanorods have N-polarity. Nitridation process also improves the optical properties of the nanorods, where non-nitridated samples show non-luminescing regions and non-uniform yellow luminescence. With increasing nitridation time, a homogenous luminescence distribution with a strong near band edge emission could be observed from the nanorods. We also examined the cross-section of the nanorods and found that luminescence from the nitridated sample is homogenous at both their exterior and interior, while the non-nitridated ones have a non-luminous core region.

We have shown nitridation is a necessary pre-treatment for the growth of self-assembled GaN nanorods on sapphire substrates in terms of controlling their morphology, polarity, and improving their optical quality.

3.4 Studies of growth parameter

In this section, we investigate the effect of growth parameters (i.e. silane co-injection, growth temperature, and growth time) on the formation of the GaN nanorods. In all

cases, the nitridation time of 300 s was used as our results above indicate that it is the optimum condition for forming a good density of nanorods with excellent morphology.

3.4.1 Effect of silane co-injection

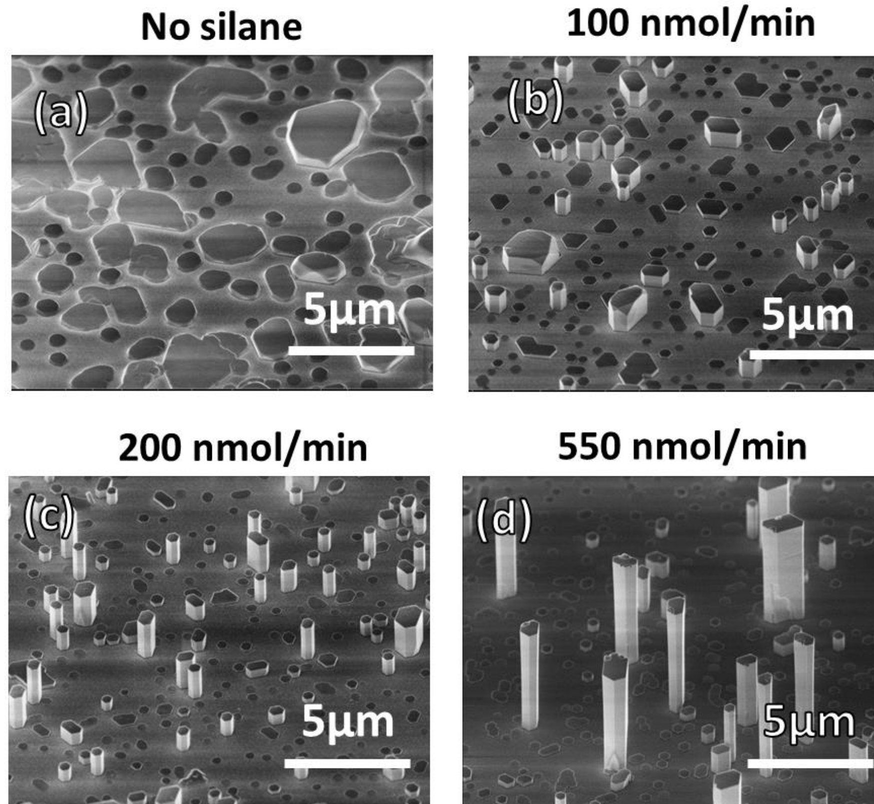

Figure 3.10 (a-d) SEM images of GaN nanorods grown with different silane co-injection flow rates ranging from 0 to 500 nmol/min.

As reported by several groups, silane injection could promote vertical growth [16, 17, 31] and enhance the thermal stability of nanorod by forming a SiN_x layer on the sidewall [32-34]. In this section, we investigate the co-injection of silane during the growth of GaN nanorods.

Silane was injected into the growth chamber simultaneously with TMGa and NH_3. As shown in figure 3.10 (a), without silane injection, GaN crystallized into irregular round shapes, rather than hexagonal shapes. Without silane injection, no vertical grown nanorod is achieved. With increasing silane flow (100-200 nmol/min), the nanorods gradually take shape and become longer. This is consistent with the finding of Tessarek *et al.* [17] that a small flux of Si would induce a dramatic change in the nanorod morphology. During the growth, Si reacts with N to form a thin SiN_x layer on the nanorod sidewall that acts as anti-surfactant and restricted the lateral growth [35].

However, at a silane flow rate of 500 nmol/min, the density of nanorod becomes less and diameters increase. This could be related to SiN_x formed on the sapphire substrate enhances the mobility of Ga atoms that lead to a larger diameter and less density [17]. The optimum flow of silane of 200 nmol/min during growth results in a good density of nanorods and is used in the next section when investigating the effect of growth temperature and time.

3.4.2 Effect of growth temperature

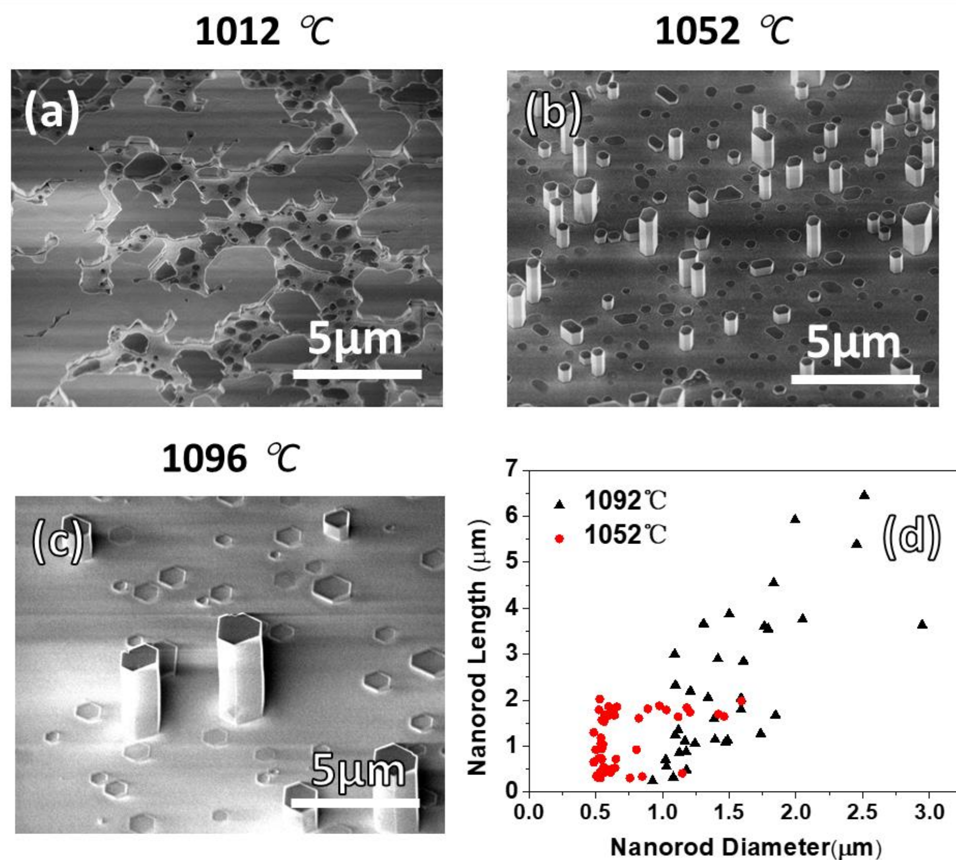

Figure 3.11 SEM images and statistical study of nanorods with different growth temperatures: (a-c) SEM images of the GaN nanorods showing the effect of growth temperature. (d) A scatter plot of nanorod height versus diameter grown at two different temperatures (1092 and 1012 °C).

Growth temperature is known to affect the growth of GaN nanorods in terms of their morphology, crystal quality and optoelectronic properties. At low temperature (1012 °C), nanorods are not formed and nucleation appears in an irregular fashion (figure 3.11 *a*). At this temperature, even with silane injection (200 nmol/min), the lateral expansion rates of the nanorods exceed their vertical growth rates and a large area of coalescence between the neighboring islands could be observed. At 1052 °C, a

good density of nanorods with excellent morphology are formed (figure 3.11 *b*). However, when the temperature is increased further to 1096 °C, the nanorod density is reduced followed by the formation of larger diameter nanorods (figure 3.11 *c*).

A statistical study of the height and diameters of the nanorods grown at 1052 and 1096 °C is shown in figure 3.11 (d). Only nanorods with heights > 300 nm are considered here. With increasing growth temperature, the nanorod diameter increases dramatically, which is consistent with a previous report [36] due to the increase in surface migration rate of adatoms, thereby leading to the easier formation of nanorods and also nanorods with larger diameters [37]. At the same time, adatom desorption rate is also increased with increasing growth temperature, which can lead to a lower density of nanorods. The temperature-dependent experiment shows that the nanorod growth window is relatively narrow, and a ± 40 °C difference from the optimum growth temperature can have a great impact on the nanorod morphology and density.

3.4.3 Effect of growth time

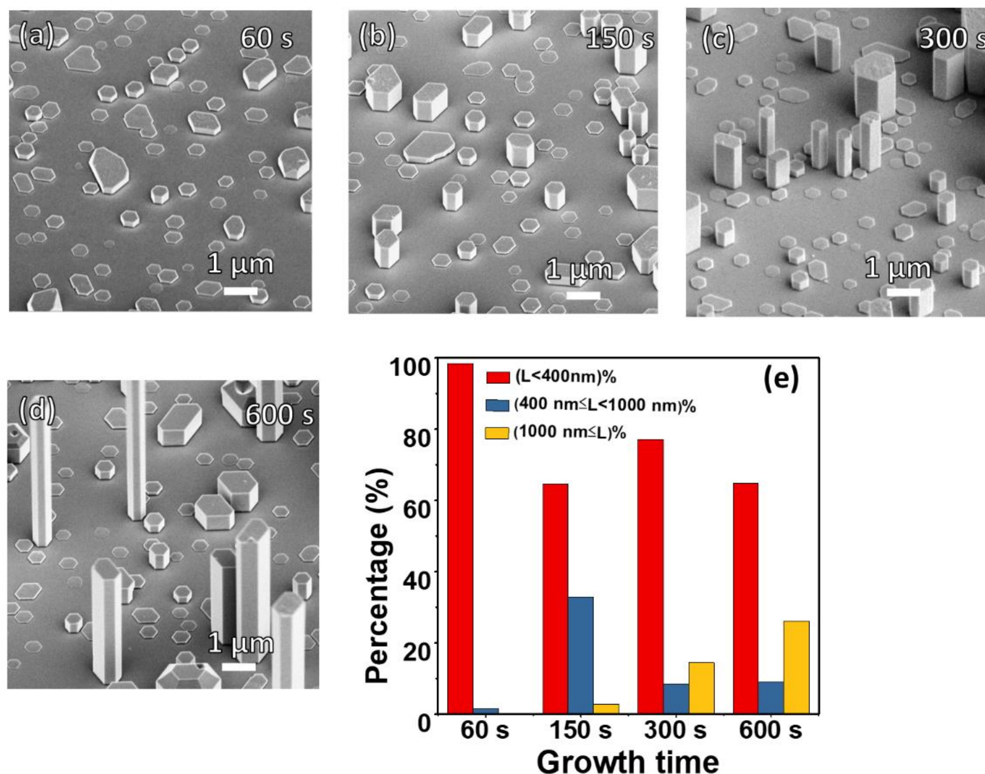

Figure 3.12 SEM images and statistical study of nanorods with different growth times: (a-d) SEM images of the GaN nanorods showing the effect of growth time. (e) Histogram showing the percentage of nanorods with different lengths for various growth times.

Figure 3.12 shows the SEM images and statistical studies of GaN nanorods with increasing growth time from 60 to 600 s. The diameter of the nanorods remains similar in all the cases studied here and a large proportion of the nanorods remains short. This trend is clearer when we classify the nanorods into three length groups. As shown in figure 3.12 (e), only short nanorods ($L<400$ nm) are formed at short growth time (60 s) and this proportion drops to 65%-75% with increasing growth time. This high proportion of short nanorods may relate to the difference in nucleation time for each nucleus. The density of medium-height nanorods ($400 \leq L<1000$ nm) peaks at 150 s of growth time with 32% of these nanorods falling into this region. At longer growth time (300 to 600 s), this number decreases to 9%. The proportion of taller nanorods ($L\geq 1000$ nm) increases from 3% (150 s) to 26% (600 s). At 600 s growth, the nanorods can reach a height of over 5.5 μm indicating a high growth speed of this type of nanorod.

No obvious tapering is found in the nanorods with increasing growth time. The diameter of nanorods remains constant from top to bottom. This result is different from some reports [36, 38], where the diameter of the top area expands with increasing growth duration. The authors attributed this tapering phenomenon to Ga accumulation at the top surface [36], which is not observed in our growth.

3.5 Summary

In this chapter, we have investigated the effects of both the pre-growth and growth parameters on the growth of self-assembled GaN nanorods. Pre-growth nitridation of the sapphire substrate by flowing NH_3 plays an important role in improving the morphology, polarity, and optical properties of the nanorods. During the nanorod growth, silane co-injection is necessary for promoting the vertical growth, and a narrow window of growth temperature (± 40 °C) is found to achieve nanorods with uniform morphology and high density.

Reference

1. C. C. Chen and C. C. Yeh, *Large-scale catalytic synthesis of crystalline gallium nitride nanowires.* Advanced Materials, 2000. **12**(10): p. 738-741.
2. C. B. Maliakkal, N. Hatui, R. D. Bapat, B. A. Chalke, A. A. Rahman and A. Bhattacharya, *The mechanism of Ni-assisted GaN nanowire growth.* Nano Letters, 2016. **16**(12): p. 7632-7638.

3. X. J. Weng, R. A. Burke and J. M. Redwing, *The nature of catalyst particles and growth mechanisms of GaN nanowires grown by Ni-assisted metal-organic chemical vapor deposition.* Nanotechnology, 2009. **20**(8): p. 085610.
4. S. D. Hersee, X. Y. Sun and X. Wang, *The controlled growth of GaN nanowires.* Nano Letters, 2006. **6**(8): p. 1808-1811.
5. Y. T. Lin, T. W. Yeh, Y. Nakajima and P. D. Dapkus, *Catalyst-free GaN nanorods synthesized by selective area growth.* Advanced Functional Materials, 2014. **24**(21): p. 3162-3171.
6. B. O. Jung, S. Y. Bae and Y. Kato, *Morphology development of GaN nanowires using a pulsed-mode MOCVD growth technique.* CrystEngComm, 2014. **16**(11): p. 2273-2282.
7. K. Choi, M. Arita and Y. Arakawa, *Selective-area growth of thin GaN nanowires by MOCVD.* Journal of Crystal Growth, 2012. **357**: p. 58-61.
8. C. Chèze, L. Geelhaar, O. Brandt, W. M. Weber, H. Riechert, S. Münch, R. Rothemund, S. Reitzenstein, A. Forchel, T. Kehagias, P. Komninou, G. P. Dimitrakopulos and T. Karakostas, *Direct comparison of catalyst-free and catalyst-induced GaN nanowires.* Nano Research, 2010. **3**(7): p. 528-536.
9. G. Jacopin, A. D. Bugallo, P. Lavenus, L. Rigutti, F. H. Julien, L. F. Zagonel, M. Kociak, C. Durand, D. Salomon, X. J. Chen, J. Eymery and M. Tchernycheva, *Single-wire light-emitting diodes based on GaN wires containing both polar and nonpolar InGaN/GaN quantum wells.* Applied Physics Express, 2012. **5**(1): p. 014101.
10. J. H. Choi, E. H. Cho, Y. S. Lee, M. B. Shim, H. Y. Ahn, C. W. Baik, E. H. Lee, K. Kim, T. H. Kim, S. Kim, K. S. Cho, J. Yoon, M. Kim and S. Hwang, *Fully flexible GaN light-emitting diodes through nanovoid-mediated transfer.* Advanced Optical Materials, 2014. **2**(3): p. 267-274.
11. X. Dai, A. Messanvi, H. Zhang, C. Durand, J. Eymery, C. Bougerol, F. H. Julien and M. Tchernycheva, *Flexible light-emitting diodes based on vertical nitride nanowires.* Nano Letters, 2015. **15**(10): p. 6958-6964.
12. N. Shuji, *GaN growth using GaN buffer layer.* Japanese Journal of Applied Physics, 1991. **30**(10A): p. L1705.
13. H. Amano, N. Sawaki, I. Akasaki and Y. Toyoda, *Metalorganic vapor phase epitaxial growth of a high quality GaN film using an AlN buffer layer.* Applied Physics Letters, 1986. **48**(5): p. 353-355.
14. S. Mohn, N. Stolyarchuk, T. Markurt, R. Kirste, M. P. Hoffmann, R. Collazo, A. Courville, R. Di Felice, Z. Sitar, P. Vennéguès and M. Albrecht, *Polarity control in group-III nitrides beyond pragmatism.* Physical Review Applied, 2016. **5**(5): p. 054004.
15. J. Song and J. Han, *Nitrogen-polar (0001) GaN grown on c-plane sapphire with a high-temperature AlN buffer.* Materials, 2017. **10**(3): p. 252.
16. X. Wang, U. Jahn, J. Ledig, H. H. Wehmann, M. Mandl, M. Straßburg and A. Waag, *The MOVPE growth mechanism of catalyst-free self-organized GaN columns in H_2 and N_2 carrier gases.* Journal of Crystal Growth, 2013. **384**: p. 61-65.
17. C. Tessarek, M. Heilmann, E. Butzen, A. Haab, H. Hardtdegen, C. Dieker, E. Spiecker and S. Christiansen, *The role of Si during the growth of GaN micro- and nanorods.* Crystal Growth & Design, 2014. **14**(3): p. 1486-1492.
18. P. Vennéguès and B. Beaumont, *Transmission electron microscopy study of the nitridation of the (0001) sapphire surface.* Applied Physics Letters, 1999. **75**(26): p. 4115-4117.

19. J. L. Rouvière, M. Arlery, R. Niebuhr, K. H. Bachem and O. Briot, *Transmission electron microscopy characterization of GaN layers grown by MOCVD on sapphire.* Materials Science and Engineering: B, 1997. **43**(1): p. 161-166.
20. S. Fuke, H. Teshigawara, K. Kuwahara, Y. Takano, T. Ito, M. Yanagihara and K. Ohtsuka, *Influences of initial nitridation and buffer layer deposition on the morphology of a (0001) GaN layer grown on sapphire substrates.* Journal of Applied Physics, 1998. **83**(2): p. 764-767.
21. K. Uchida, A. Watanabe, F. Yano, M. Kouguchi, T. Tanaka and S. Minagawa, *Nitridation process of sapphire substrate surface and its effect on the growth of GaN.* Journal of Applied Physics, 1996. **79**(7): p. 3487-3491.
22. B. Alloing, S. Vezian, O. Tottereau, P. Vennegues, E. Beraudo and J. Zuniga-Perez, *On the polarity of GaN micro- and nanowires epitaxially grown on sapphire (0001) and Si(111) substrates by metal organic vapor phase epitaxy and ammonia-molecular beam epitaxy.* Applied Physics Letters, 2011. **98**(1): p. 011914.
23. M. Hetzl, M. Kraut, T. Hoffmann and M. Stutzmann, *Polarity control of heteroepitaxial GaN nanowires on diamond.* Nano Letters, 2017. **17**(6): p. 3582-3590.
24. C. Tessarek, S. Figge, A. Gust, M. Heilmann, C. Dieker, E. Spiecker and S. Christiansen, *Optical properties of vertical, tilted and in-plane GaN nanowires on different crystallographic orientations of sapphire.* Journal of Physics D: Applied Physics, 2014. **47**(39): p. 394008.
25. B. Zhao, M. N. Lockrey, P. Caroff, N. Wang, L. Li, J. Wong-Leung, H. H. Tan and C. Jagadish, *The effect of nitridation on the polarity and optical properties of GaN self-assembled nanorods.* Nanoscale, 2018. **10**(23): p. 11205-11210.
26. R. K. Debnath, R. Meijers, T. Richter, T. Stoica, R. Calarco and H. Luth, *Mechanism of molecular beam epitaxy growth of GaN nanowires on Si(111).* Applied Physics Letters, 2007. **90**(12): p. 123117.
27. M. de la Mata, C. Magen, J. Gazquez, M. I. B. Utama, M. Heiss, S. Lopatin, F. Furtmayr, C. J. Fernández-Rojas, B. Peng, J. R. Morante, R. Rurali, M. Eickhoff, A. Fontcuberta i Morral, Q. Xiong and J. Arbiol, *Polarity assignment in ZnTe, GaAs, ZnO, and GaN-AlN nanowires from direct dumbbell analysis.* Nano Letters, 2012. **12**(5): p. 2579-2586.
28. X. J. Chen, G. Perillat-Merceroz, D. Sam-Giao, C. Durand and J. Eymery, *Homoepitaxial growth of catalyst-free GaN wires on N-polar substrates.* Applied Physics Letters, 2010. **97**(15): p. 151909.
29. C. H. Seager, A. F. Wright, J. Yu and W. Götz, *Role of carbon in GaN.* Journal of Applied Physics, 2002. **92**(11): p. 6553-6560.
30. A. Berg, P. Caroff, N. Shahid, M. N. Lockrey, X. Yuan, M. T. Borgström, H. H. Tan and C. Jagadish, *Growth and optical properties of $In_xGa_{1-x}P$ nanowires synthesized by selective-area epitaxy.* Nano Research, 2017. **10**(2): p. 672-682.
31. R. Koester, J. S. Hwang, C. Durand, S. Dang Dle and J. Eymery, *Self-assembled growth of catalyst-free GaN wires by metal-organic vapour phase epitaxy.* Nanotechnology, 2010. **21**(1): p. 015602.
32. T. Stoica, E. Sutter, R. J. Meijers, R. K. Debnath, R. Calarco, H. Luth and D. Grutzmacher, *Interface and wetting layer effect on the catalyst-free nucleation and growth of GaN nanowires.* Small, 2010. **4**(6): p. 751-754.

33. H. D. Batha and E. D. Whitney, *Kinetics and mechanism of the thermal decomposition of Si_3N_4.* Journal of the American Ceramic Society, 2006. **56**(7): p. 365-369.
34. R. Groh, G. Gerey, L. Bartha and J. I. Pankove, *On the thermal decomposition of GaN in vacuum.* Physica Status Solidi, 2010.
35. T. Markurt, L. Lymperakis, J. Neugebauer, P. Drechsel, P. Stauss, T. Schulz, T. Remmele, V. Grillo, E. Rotunno and M. Albrecht, *Blocking growth by an electrically active subsurface layer: The effect of Si as an antisurfactant in the growth of GaN.* Physical Review Letters, 2013. **110**(3): p. 036103.
36. W. Xue, L. Shunfeng, F. Sönke, H. W. Hergo, S. Martin, L. Hans-Jürgen, S. Ulrich and W. Andreas, *Mechanism of nucleation and growth of catalyst-free self-organized GaN columns by MOVPE.* Journal of Physics D: Applied Physics, 2013. **46**(20): p. 205101.
37. C. Nozaki, Y. Ohba, H. Sugawara, S. Yasuami and T. Nakanisi, *Growth temperature dependent atomic arrangements and their role on band-gap of ingaalp alloys grown by MOCVD.* Journal of Crystal Growth, 1988. **93**(1): p. 406-411.
38. A. Bugallo, L. Rigutti, G. Jacopin, F. Julien, C. Durand, X. Chen, D. Salomon, J. Eymery and M. Tchernycheva, *Single-wire photodetectors based on InGaN/GaN radial quantum wells in GaN wires grown by catalyst-free metal-organic vapor phase epitaxy.* Applied Physics Letters, 2011. **98**(23): p. 3107.

Chapter 4

Rosette-shaped cathodoluminescence pattern in GaN nanostructures

4.1 Introduction

In chapter 3, we achieved unipolar self-assembled GaN nanorods by controlling their pre-growth and growth parameters. In this chapter, we continue to study the optical properties of GaN nanorods and explore the origin of their defect emission peak. Understanding the optical properties of defects and minimizing their influence on devices are extremely important. In GaN and related materials, defect-related optical processes, such as non-radiative recombination centers and yellow luminescence (YL), would compete with the near-bandgap emission (NBE) for carrier recombination path [1-3], which could in turn reduces the device efficiency.

Non-radiative recombination in GaN has been attributed to Shockley-Read-Hall (SRH) and Auger recombination [4]. In contrast, there is still no consensus on the chemical origins of YL. It has been attributed to point defects [2, 5-7], threading dislocations [3, 8], grain boundaries [3], Ga vacancies [1, 2, 9, 10] or impurities incorporation such as carbon [9, 11-14], silicon [1, 10, 15-17] and oxygen [18, 19]. The studies in GaN nanorods may yet bring another opportunity to understand the origin [20] and spatial distribution of these defect-related optical processes. Thanks to the dislocation bending and filtering effects in nanostructures, the influence of threading dislocations and grain boundaries can be minimized [21, 22]. The unique 3D geometry of nanostructures also allows simultaneous investigation of the defect-related optical processes on both polar and non-polar planes.

For non-radiative defects, C. Zhao et al. [23] found that SRH recombination could be effectively suppressed by organic sulfide passivation in InGaN/GaN disk-in-nanowire LEDs grown on silicon. Several research groups have revealed that YL in nanorods is surface-related. Li *et al.* [24] have shown that the YL is mostly distributed

on the surface layer in $[11\overline{2}0]$ oriented nanowires with a triangular cross-section and is attributed to point defects, such as isolated Ga vacancies incorporated during growth. Huang *et al.* [25] proposed a size-related surface 'microwire' theory through first-principles calculations and attributed YL to gallium vacancies and carbon-related defects on the nanowire surface.

In this chapter, we investigated an intriguing rosette-shaped pattern through cathodoluminescence (CL) imaging at the early stages of GaN nanorod growth. This phenomenon is prevalent in the nanostructures and not affected by nanorod geometry, symmetry or size, but related to the origin of the defect-related optical process. We performed detailed investigations by CL, aberration-corrected scanning transmission electron microscopy (Cs-corrected STEM), and nanoscale secondary ion mass spectrometry (nano-SIMS). Detailed CL spatial imaging and spectral analysis will be discussed in section 4.3. The investigation of optical resonance modes and polarity inversion boundaries will be discussed in section 4.4 and section 4.5, respectively. We will discuss the strain distribution and chemical elements identification in section 4.6 and section 4.7, respectively. In section 4.8, we will present a growth model of the self-assembled GaN nanorod based on the correlation between defects distribution and CL pattern evolution. The summary of this chapter is in section 4.9.

4.2 Experiment

We conducted the growths of the GaN nanostructures on (0001) sapphire substrate in an Aixtron MOCVD close-coupled showerhead system. The detailed growth procedure was discussed in chapter 3. Briefly, growth was initiated with a 10 s nucleation stage at 1050 °C where trimethylgallium (13.65 mmol/min) and NH_3 (25 sccm) were injected. Then growth was continued for 300 s with a reduced NH_3 flow of 15 sccm and simultaneously introducing SiH_4 (200 nmol/min) to promote vertical growth. The morphology and CL properties of these nanostructures were characterized using a FEI Verios 460 scanning electron microscope (SEM) equipped with a Gatan MonoCL4 Elite system. CL measurements were conducted at both room temperature and liquid nitrogen temperature with 1-5 kV beam voltage.

We prepared TEM-lamella samples in a FEI Helios Nanolab focused ion beam (FIB) system with an ion-beam voltage of 30 kV. All cross-sectional TEM lamellae were prepared with the nanorods connected to the substrate to ensure that the growth

direction can be identified. Finally, the lamellae were analyzed by aberration-corrected scanning transmission electron microscope (Cs-corrected STEM) using a JOEL ARM200F instrument with a sub-Å resolution for polarity determination [26]. We used the relative position of the gallium and nitrogen atomic columns with respect to the growth direction for polarity determination. Other lamella samples with 1 μm thickness were also prepared by FIB for nano-SIMS measurement in CAMECA NanoSIMS 50L with Cs^+ and O^- sources.

4.3 CL observation of the rosette-shaped pattern

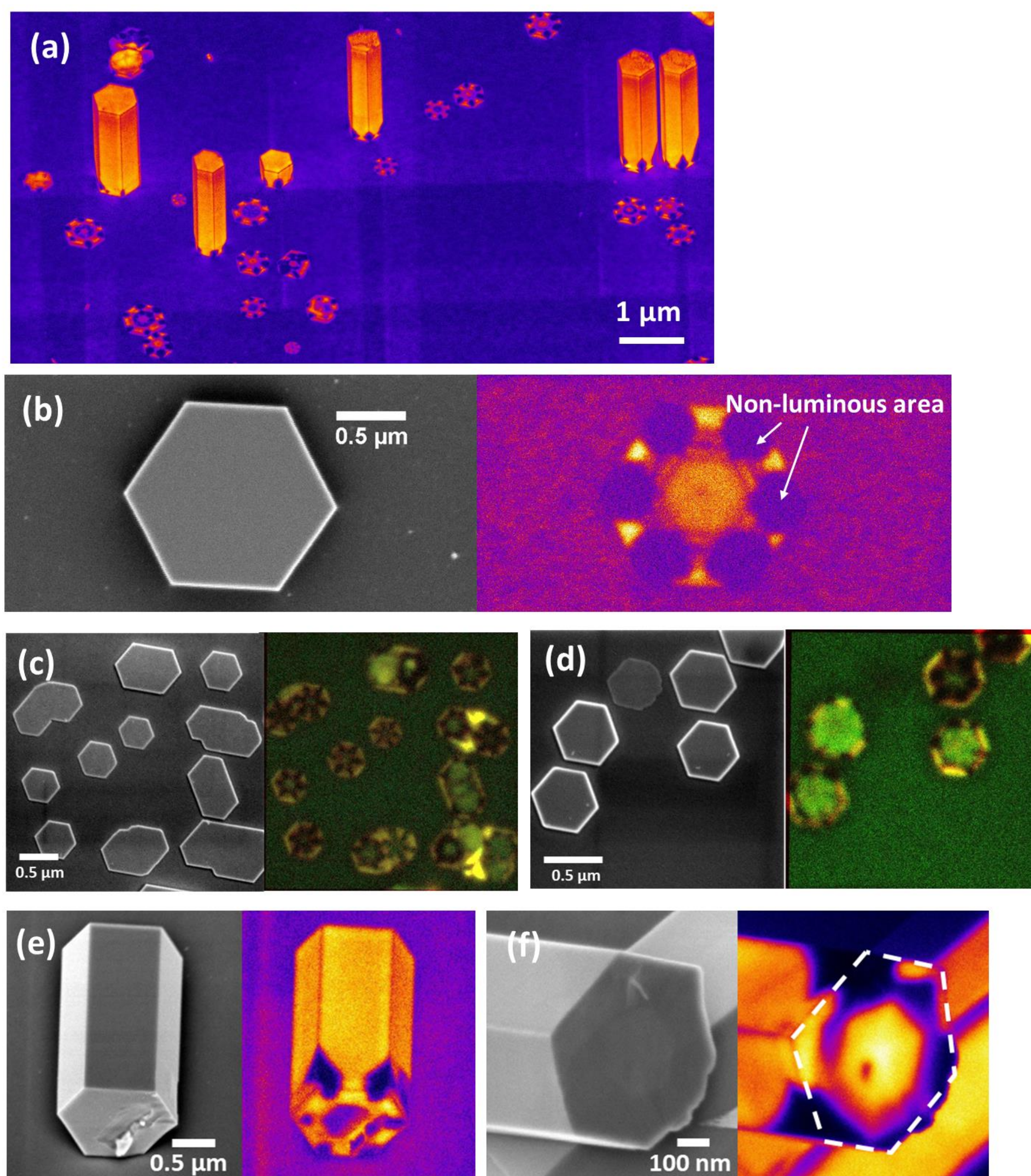

Figure 4.1 SEM and panchromatic CL images of GaN nanostructures with rosette-shaped pattern: (a) Panchromatic CL image of the rosette-shaped pattern in GaN nanostructures (45-

degree tilted view). (b) SEM and corresponding panchromatic CL image of GaN nanodisks with typical rosette-shaped luminescence. The non-luminous areas marked by white arrows. (c, d) Nanodisks with 60 s growth duration: SEM and composite images reconstructed from green and red color filters. (e, f) SEM and panchromatic CL images of nanorods lying down on the substrate with the bottom surface facing the observation direction. A white dashed hexagonal in (f) indicates the bottom area of the nanorod.

The GaN nanostructures consist of nanodisks and nanorods. We found a six-fold rosette-shaped CL pattern in the nanostructures. A typical pattern consists of three parts (figure 4.1 *b*): non-luminous regions at the corners of the hexagon acting as the 'flower petals', a slightly luminous region in the center of the hexagon acting as the 'flower core', and the rest of the hexagon (at the edges) emitting relatively strong CL signals. As could be seen in figure 4.1 (a), this pattern is especially remarkable in nanodisks with low aspect ratios. For the longer nanorods, this pattern persists at the bottom region, but with further vertical growth, the rest of the nanorods exhibits a relatively uniform luminescence.

The rosette-shaped CL pattern exists to some degree in all of the GaN nanostructures. In samples with a very short growth duration of 60 s, the rosette pattern is visible (figure 4.1 *c* and *d*). The height of these nanorods is around 100 nm, which indicates the pattern formation is closely tied to the early stage of growth. The rosette pattern is also found on the bottom surface of nanorods with higher aspect-ratios, and those patterns are still visible even after vertical growth (figure 4.1 *e* and *f*).

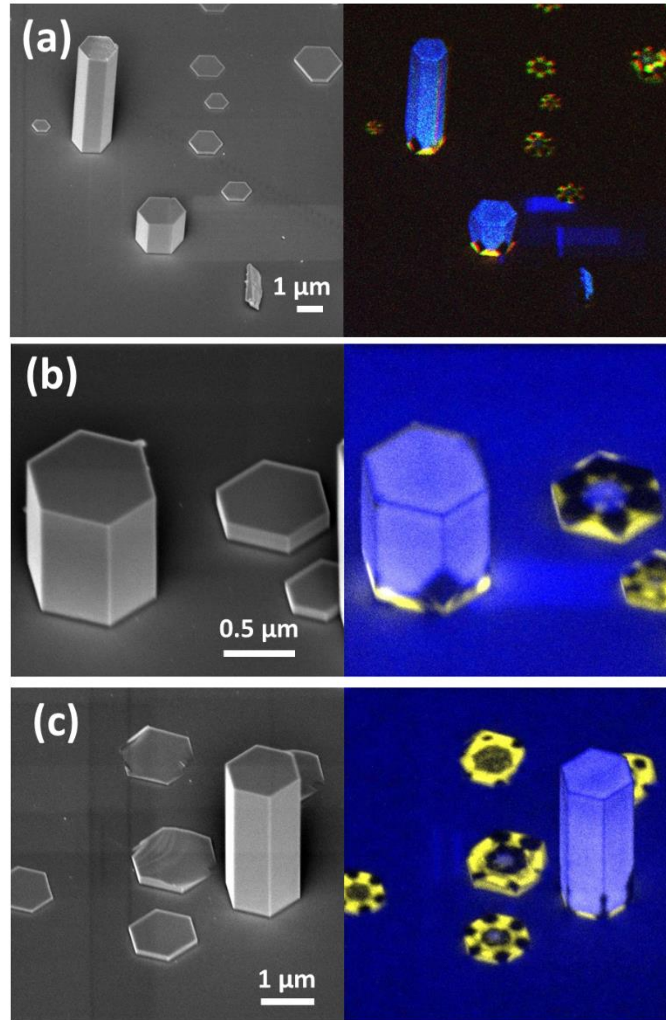

Figure 4.2 (a-c) Composite images reconstructed from red-green-blue (RGB) color filters (45-degree tilt view): yellow luminescence at the bottom of the nanorods and near-band emission for the rest of the nanorods could be clearly identified.

Figure 4.2 presents the emission wavelength distribution throughout the nanostructures. Under the RGB colour filters, the blue colour corresponds to the near-band emission (NBE), while the yellow colour corresponds to YL. YL outlines the rosette pattern of the nanodisks, while for taller nanorods, YL is confined at the bottom, and the rest of the rod emits strong NBE. A clear interface could be seen between these two types of emissions at just above the 'rosette region'. The appearance of the pattern is different in nanorods with different heights, and this phenomenon will be discussed later in the chapter.

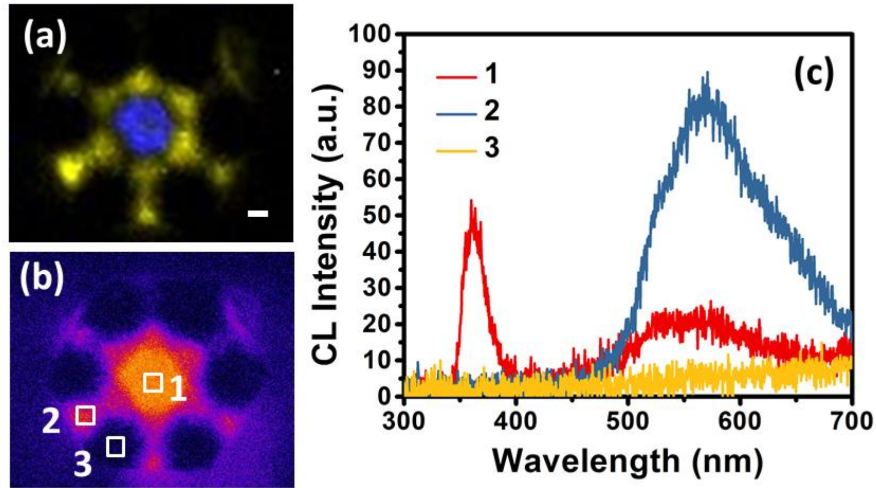

Figure 4.3 Low-temperature (80 K) spectral imaging and spectra of GaN nanostructure: (a) Composite image reconstructed from RGB color filters (the scale bar is 100 nm); (b) Panchromatic CL image with three spots selected for spectral measurements; (c) CL spectra extracted from the spots indicated in (b).

To further analyze the CL emission spatially and spectrally, we carried out spatially-resolved CL mapping at liquid nitrogen temperature. In figure 4.3 (a), the hexagonal-shaped NBE is confined to the center of the nanodisk, while the rest of the nanodisk emits strong YL, except for the six non-luminous regions at the vertices of the nanodisks. Three points are analyzed in the panchromatic image of figure 4.3 (b). As shown in the spectral plot in figure 4.3 (c), point 1 (center) emits strong NBE (peak at 360 nm) and a relatively weak YL; point 2 (edge of the hexagon) emits YL only; point 3 (vertex of the hexagon) does not emit at all.

4.4 Optical modes inside the hexagonal cavity

The rosette-pattern in the GaN nanostructure is an interesting and curious observation that has not been reported in the literature. A similar flower-shaped CL pattern was reported in ZnO nanorods [27], in which the authors attributed the phenomenon to changes in surface roughness. The phenomenon we found in GaN may be related to several factors: optical modes inside the hexagonal cavity, formation of polarity inversion domains, strain relaxation, and defect/impurity accumulation at the corners of the hexagons. We will analyze all these possible causes in this chapter.

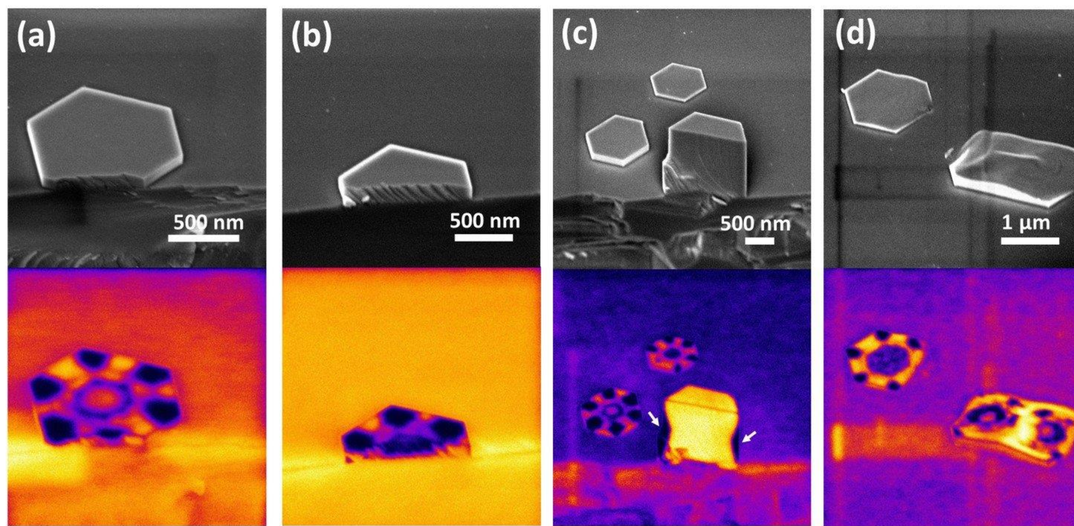

Figure 4.4 (a-c) SEM images of intentionally broken GaN nanodisks (ex-situ, post-growth) and their corresponding panchromatic CL images showing the rosette-shaped luminescence still clearly visible. The white arrows in *c* indicate where the pattern exists. (d) SEM image of two nanodisks that merged during growth and their corresponding CL image showing overlap of two independent rosette patterns.

Optical modes may be supported in the cavity due to the high regularity and symmetry of the hexagonal nanodisks. Two common types of optical resonance modes are reported in GaN nanorods: whispering gallery mode [28-31] (horizontal propagation) and Fabry–Pérot mode [32, 33] (vertical propagation).

One approach that investigates whether these modes are playing a role in pattern formation is by destroying parts of the cavity, thereby suppressing certain types of optical modes [30]. Here we deliberately break the nanodisks with a diamond scribe by cleaving the wafer. Three different types of damaged cavities are shown in figure 4.4. In the first two cases (figure 4.4 *a*-*c*), the rosette pattern remains even after the nanodisk

shape is no longer hexagonal. Also, when two nanodisks merge during growth (figure 4.4 *d*), the CL pattern is still visible, but as an overlap of two independent patterns. All the above observations indicate that the rosette-pattern is not affected by shape changes after its formation and thus not due to optical modes supported by the cavity.

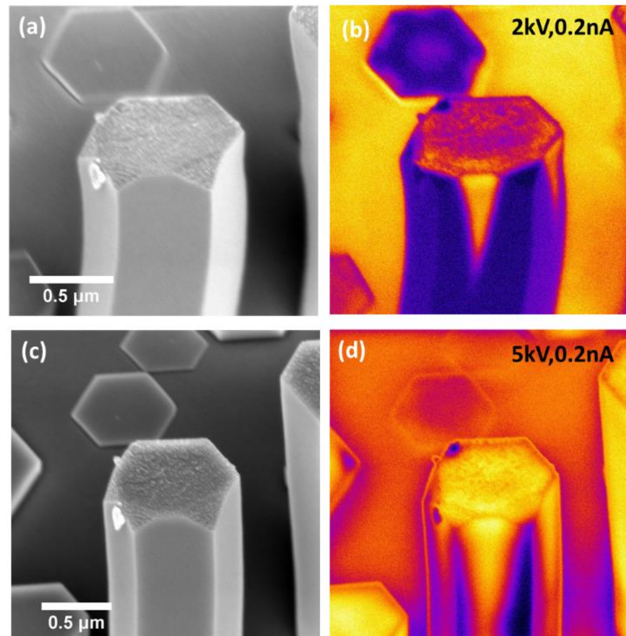

Figure 4.5 (a-d) SEM and corresponding panchromatic CL images of a nanorod at different acceleration voltages. The slight curvature of the nanorod is due to the drifting of high-resolution SEM imaging.

The results from these broken cavities also prove that the CL pattern occurs not only on the surface but also exists inside of the nanostructure, which is consistent with our acceleration voltage-dependent CL imaging shown in figure 4.5. When increasing the voltage from 2 to 5 kV, the electron beam probes further inside the nanorod. The dark diamond shape decreases in size with a higher voltage, which means that the non-luminous regions are closer to the surface of the nanorod.

4.5 Polarity determination and STEM imaging

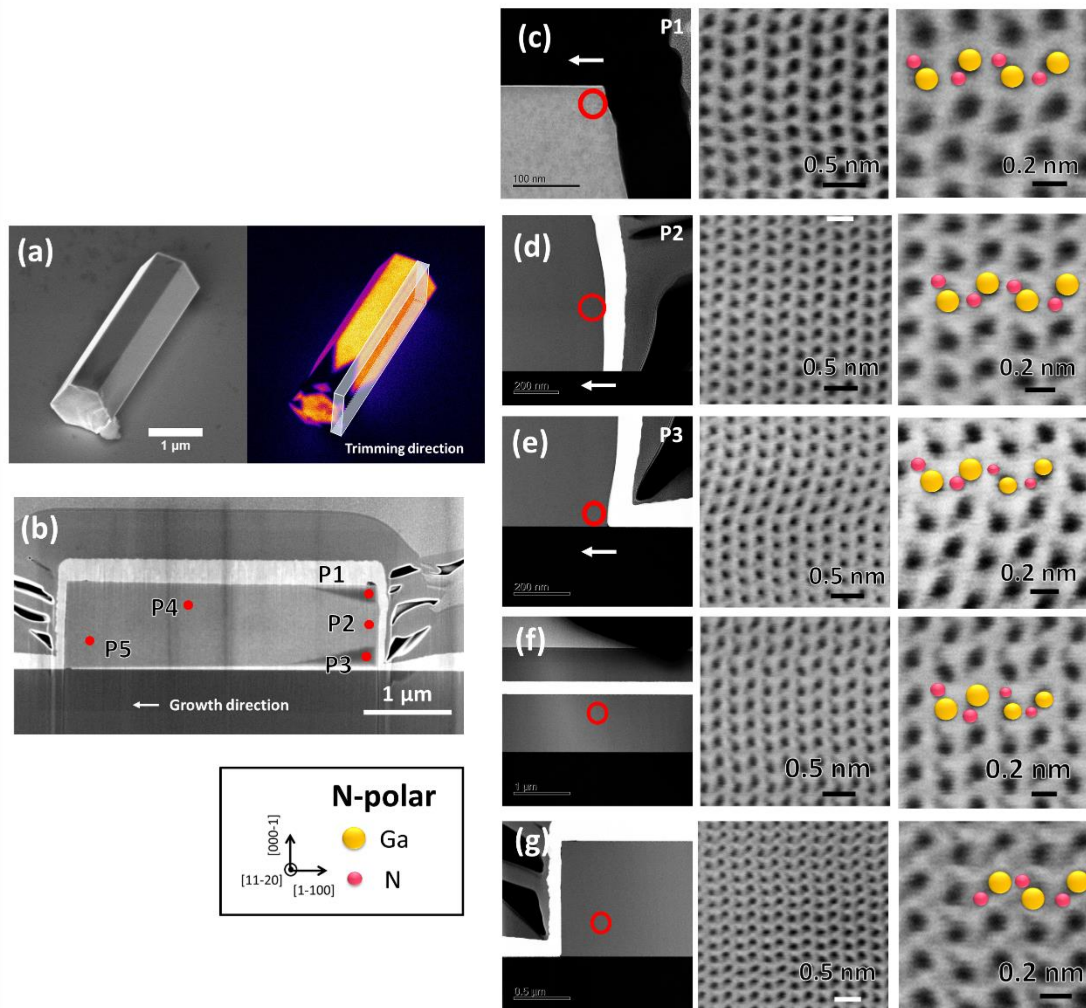

Figure 4.6 Polarity determination at various spots in a GaN nanorod lamella: (a) SEM and corresponding panchromatic CL images of a GaN nanorod with a rosette-shaped pattern at its bottom. A sketch outlining the region where a lamella was subsequently made by FIB is also shown. (b) Secondary electron image of a FIB lamella sectioned from the nanorod in *a*, showing clear contrast from the diamond-shaped regions. (c-g) Left: STEM images at different parts of the lamella as indicated in *b*. Right: High magnification annular bright-field images taken from regions indicated by the red circles are shown in the left images. Asymmetric atomic dumb-bell images reveal the smaller N atoms on top of the double atom layers (N-polar).

Next, we consider whether this unique pattern is related to crystallography variations, such as the presence of inversion domain boundaries. Coulon *et al.* [34] reported that N-polar domains exhibit stronger near-band emission compared with their Ga-polar

counterparts, and the Ga-polar domains emit only YL. These claims suggest that the formation of this CL pattern could be polarity-driven such that inversion domain boundaries are formed at the bottom area of the nanorods.

To investigate the polarity of both the luminous and non-luminous regions of the nanodisk, a lamella was prepared by FIB with the milling direction along the edge of the hexagonal prism, as indicated in figure 4.6 (a). A 200 nm-thick lamella was first lifted out from the nanorod for SEM imaging (figure 4.6 *b*), and then this lamella was thinned to 50 nm for Cs-corrected STEM.

Five spots (figure 4.6 *b*) were selected for Cs-corrected analysis, three spots from the rosette region, and two from the other areas. Spots P1 and P3 are at the non-luminous corners. The direct observation of atomic dumb-bell pairs shows that the smaller nitrogen atom is on the top of the double atomic layer, thereby confirming the N-polar nature of these two regions (figure 4.6 *c* and *e*). Spot P2 was taken in the middle part within the bright CL region and can also be identified to show N-polarity (figure 4.6 *d*). Spot P4 and P5 at the middle and top area of the rod are also characterized, showing that the nanorod is homogeneously N-polar. Therefore, these data allow us to exclude inversion domain boundaries as the cause of the rosette-shaped CL pattern.

We also found the secondary electron image showing a similar rosette contrast to the CL images (see the darker SEM contrast in figure 4.6 *b*). This contrast indicates a difference in the energy distribution of secondary electrons [35-37]. The effects of material and topography on the SEM contrast can be excluded as the analysis was performed on a flat GaN lamella. Thus, the SEM contrast is most likely related to changes in surface potential and doping level (conductivity) across the region [36].

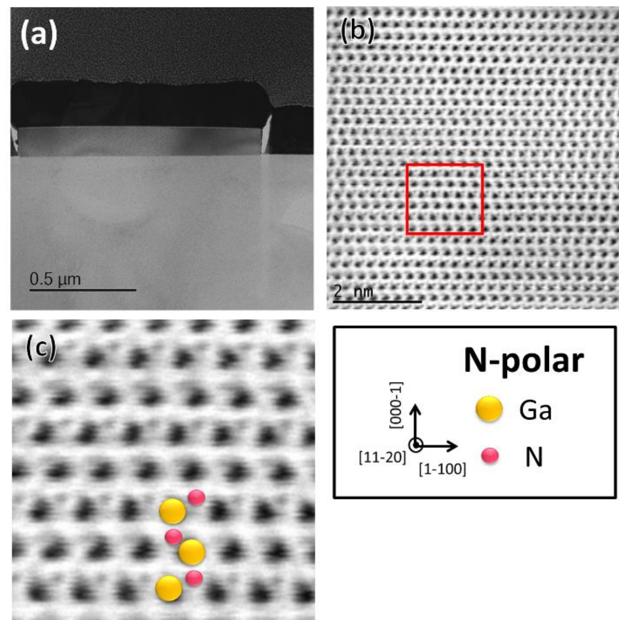

Figure 4.7 STEM images of a nanodisk lamella attached to the substrate. (a) STEM image of the nanodisk. (b, c) The polarity of the nanodisk is nitrogen polar with the smaller N atoms on top of the dumb-bell pair; image *c* is an enlarged image indicated by the red box in image *b*.

The polarity in a low aspect-ratio nanodisk is also identified. The target nanodisk attached to the sapphire substrate was sliced into lamella. A clear interface could be observed in figure 4.7 (a). Based on figure 4.7 (b) and (c), we determined the nanodisk as N-polar that is consistent with nanorods that have high aspect ratios.

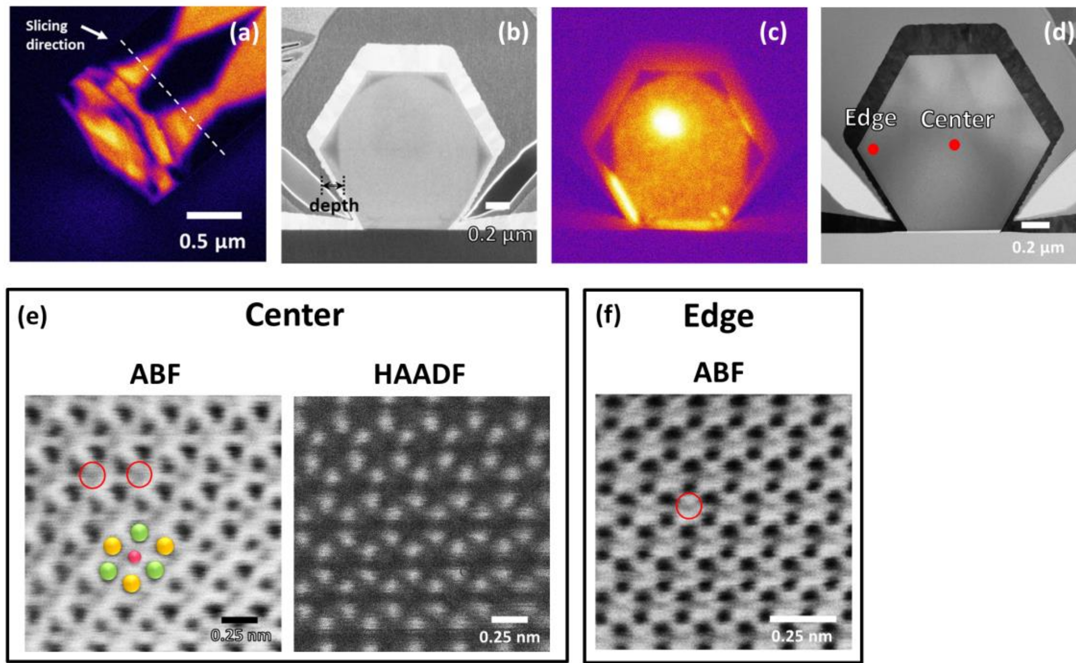

Figure 4.8 (a-c) SEM and panchromatic CL images of the lamella sliced before reaching the turning point in the diamond shape. (d) TEM lamella further thinned from figure 4.8 *b*. (e-f) Images were from the areas indicated by the red dots in (d). Dark contrast in the high magnification annular bright-field (ABF) image could be the interstitial atoms, shown by the red circles. The matrix atoms are stacked in the ABABA sequence. (green spheres indicate A atoms, yellow spheres indicate B atoms, while the pink sphere represents the interstitial atom).

Apart from the lamella sliced along the growth direction, we also sliced the lamella perpendicular to the growth direction for Cs-corrected TEM. As shown in figure 4.8 (a), the lamella is sliced before reaching the turning point in the 'diamond shape' at the rosette region. From figure 4.8 (b) and (c), we find that the contrast in SEM and CL images are correlated, and the non-luminous regions extend deep inside the surface. After the CL measurement, this lamella was further thinned down for Cs-corrected TEM, and two spots were selected to compare the structural difference between the center and edge of the cross-section. For the center spot, the dark contrast in the annular bright-field (ABF) image could be interstitial atoms, but these atoms are not visible in the high-angle annular dark-field (HAADF) image taken at the same region. Because ABF imaging is better at visualization of ultralight elements, it indicates that these missing interstitial atoms in the HAADF image are light elements. However, similar phenomenon is also visible for the spot at the edge part. Therefore, this phenomenon is not related to CL pattern formation, and further experiments are required to verify the type and distribution of the atoms.

4.6 Strain analysis

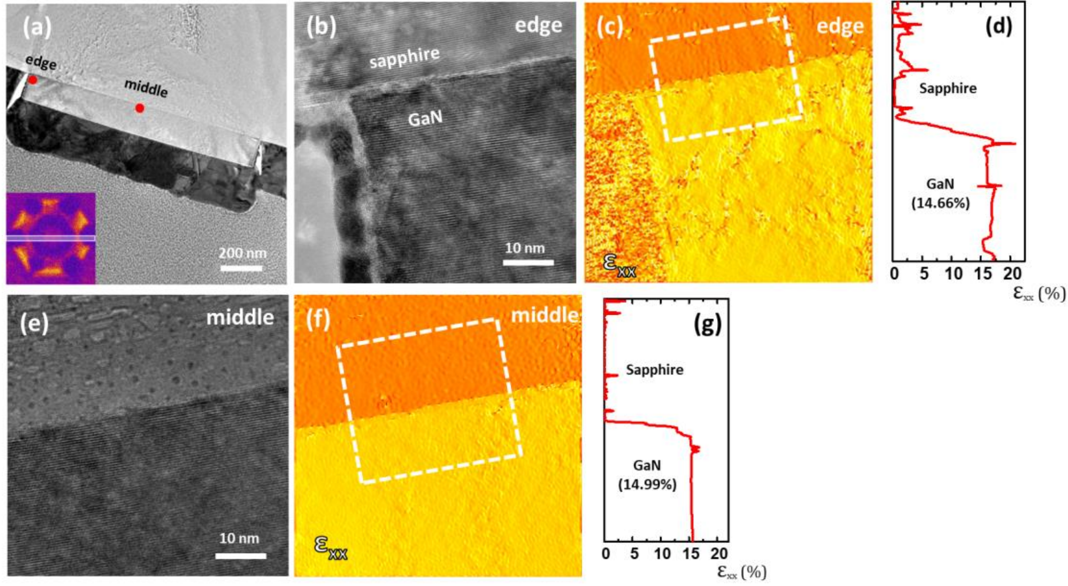

Figure 4.9 (a) TEM lamella sectioned from a GaN nanodisk. Inset: CL image of the nanodisk (cutting direction indicated by the white rectangle). (b) The TEM image at the nanodisk edge showing the interface between sapphire and GaN. (c) GPA map of radial strain ε_{xx} corresponding to the area in *b*. (d) integrated strain profile over the white-dash rectangle indicated in *c*. (e) TEM image of the middle region indicated by the red dot in *a*; (f) GPA map of radial strain ε_{xx} corresponding to the area in *e*; (g) integrated strain profiles over the white-dash rectangle indicated in *f*.

We investigated the region near the nanorod/substrate interface because the peculiar CL pattern is formed close to this area. Defects induced by strain relaxation (due to the lattice mismatch between GaN and sapphire) can act as non-radiative recombination centers. They may cause the formation of the pattern, i.e., the non-luminous regions [38-41]. We evaluated the strain at the GaN/sapphire interface using geometrical phase analysis (GPA) on high-resolution TEM images of the interface [42, 43]. The lattice displacement of the GaN nanodisk was calculated using the sapphire substrate as a reference.

A target nanodisk was sliced across the opposite vertices of the hexagon (inset image of figure 4.9 *a*) to verify the strain level. GPA maps of in-plane strain ε_{xx} (nanodisk radial growth direction) are shown in figures 4.9 (c). In figure 4.9 (c), a sharp colour-scale contrast could be seen between the GaN (yellow) and the sapphire (orange). A corresponding scan area across the interface indicates that GaN is under large

compressive strain (14.66%) with respect to sapphire (figure 4.9 *d*). However, the strain profile is uniform and does not reflect the pattern observed in the CL image. Similarly, the GPA map of the middle area of the nanorod (figure 4.9 *f*) also shows no correlation with the CL pattern. Based on the results above, we can rule out strain at the interface as the cause for this pattern formation.

4.7 Nano-SIMS studies

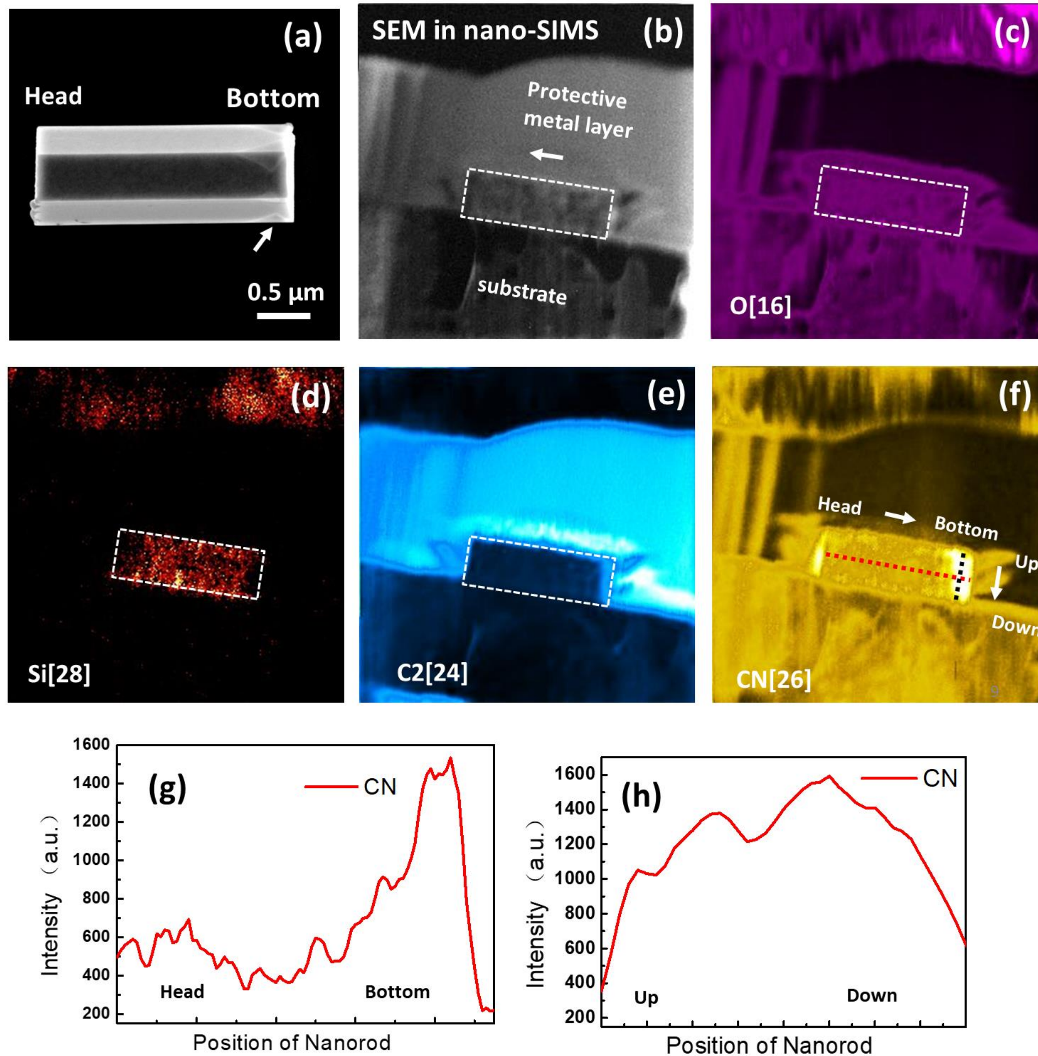

Figure 4.10 (a) SEM image of single GaN nanorod (diamond-shape contrast indicated by white arrow). (b) SEM image in the nano-SIMS system of a lamella made from nanorod shown in a. The white arrow indicates the growth direction of the nanorod. (c-f) Mass intensity map of ^{16}O, ^{28}Si, $^{24}C_2$, and $^{12}C^{14}N$. (g, h) Line scans from the $^{12}C^{14}N$ map along the length and across the bottom of the nanorod, respectively. In figure *f*, a dashed black line and a dashed red line indicate the scan positions. The white arrows indicate scanning directions.

We then carried out the nano-SIMS measurement on a FIB lamella sample to evaluate the variation of chemical composition and impurities. A target nanorod is shown in figure 4.10 (a) with a clear SEM contrast of the pattern at the bottom (indicated by white arrow).

We identified several elements from the nano-SIMS analyses, including ^{16}O, ^{28}Si,

$^{24}C_2$, and $^{12}C^{14}N$. In the ^{16}O map, not much difference could be found along the length of the nanorod, which indicates a relatively uniform distribution of oxygen throughout the nanorod. The ^{28}Si map shows the lack of Si at the bottom area, which could be related to the initial stage of the growth before the introduction of SiH_4 precursor. The $^{24}C_2$ map also shows relatively high intensity at the bottom area. In the $^{12}C^{14}N$ map, the bottom area of the nanorod has a higher intensity (indicated by the white arrow). Two-line scan plots (figure 4.10 *g* and *h*) are extracted from the $^{12}C^{14}N$ map. From the line scan plot along the growth direction, we could see the signal of the $^{12}C^{14}N$ cluster from the bottom area is significantly higher than the rest of the nanorod. For direction pedicular to the growth direction, the intensity is high at the center and drops towards the edge.

Carbon could be introduced as isolated C_N, which has been linked with YL in many reports [5, 11, 45]. Christenson *et al.* [11] predicted isolated C_N peaks at 2.18 eV with zero phonon line (ZPL) at 2.67 eV, which is in agreement with the YL emission observed in our study. The latest theoretical calculations also show YL is more related to isolated C_N rather than C_N complexes [11], such as C_N-O_N and C_N-V_{Ga} due to their instability [44-46]. Based on our growth conditions using a low V/III ratio, we believe carbon is the most likely cause of the YL. However, since we detect CN clusters in SIMS (rather than C to increase the sensitivity) [47], we cannot completely rule out the effect of N in YL. Additionally, due to the resolution limits of SIMS, we are not able to pick out the data from the specific spot in the pattern area. Nonetheless, the presence of excess C and N at the bottom region of the nanorods and their effect on the optical properties strongly suggests that the excess C and/or N incorporation is key to the CL pattern formation.

4.8 Evolution of the CL pattern

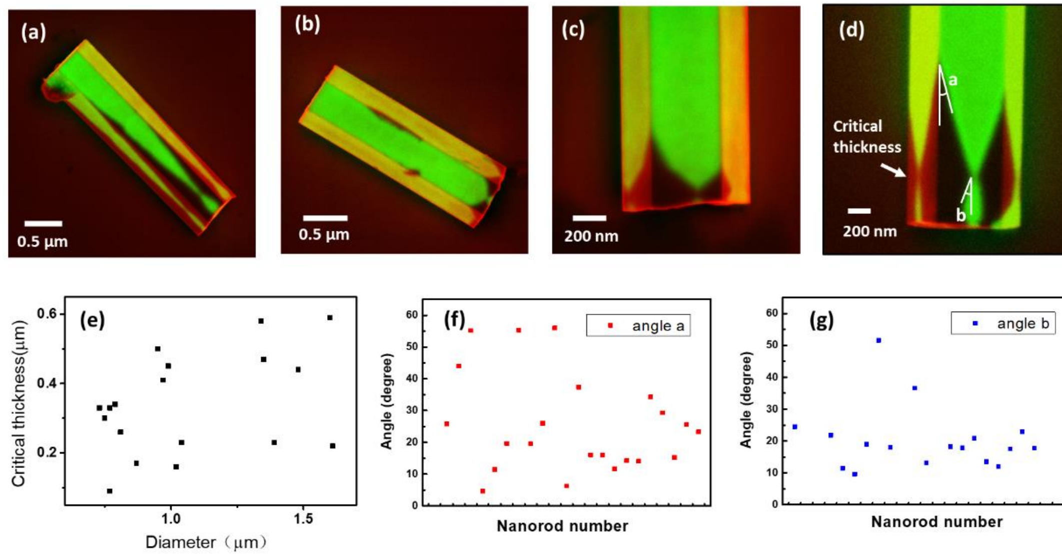

Figure 4.11 (a-d) SEM & CL composite images showing the 'diamond-shape' with different angles (SEM: red, CL: green). (e) Scatter plot of the relationship between diameter and 'critical thickness' (diamond edge). (f, g) Angles formed by the diamond vs. diameter of the nanorods.

The angles of the 'diamond shapes' of the CL pattern in the nanorods are analyzed as shown in figure 4.11. From figure 4.11 (a) to (c), we could see the 'diamond-shape' varies from rod to rod. Angle '*a*' is located at the diamond top area, while angle '*b*' is at the bottom of the diamond, as indicated in figure 4.11 (d). Statistical analyses plotted in figure 4.11 (f), (g) show the values of angles '*a*' and '*b*' are not constant. We also measured the 'critical thickness' - the height at the turning point in the diamond shape expansion. The scattered plot shown in figure 4.11 (e) indicates that the critical thickness is roughly in the range of 200 to 500 nm (average value 339 ±146 nm), and no clear relationship could be drawn between the nanorod diameter and critical thickness.

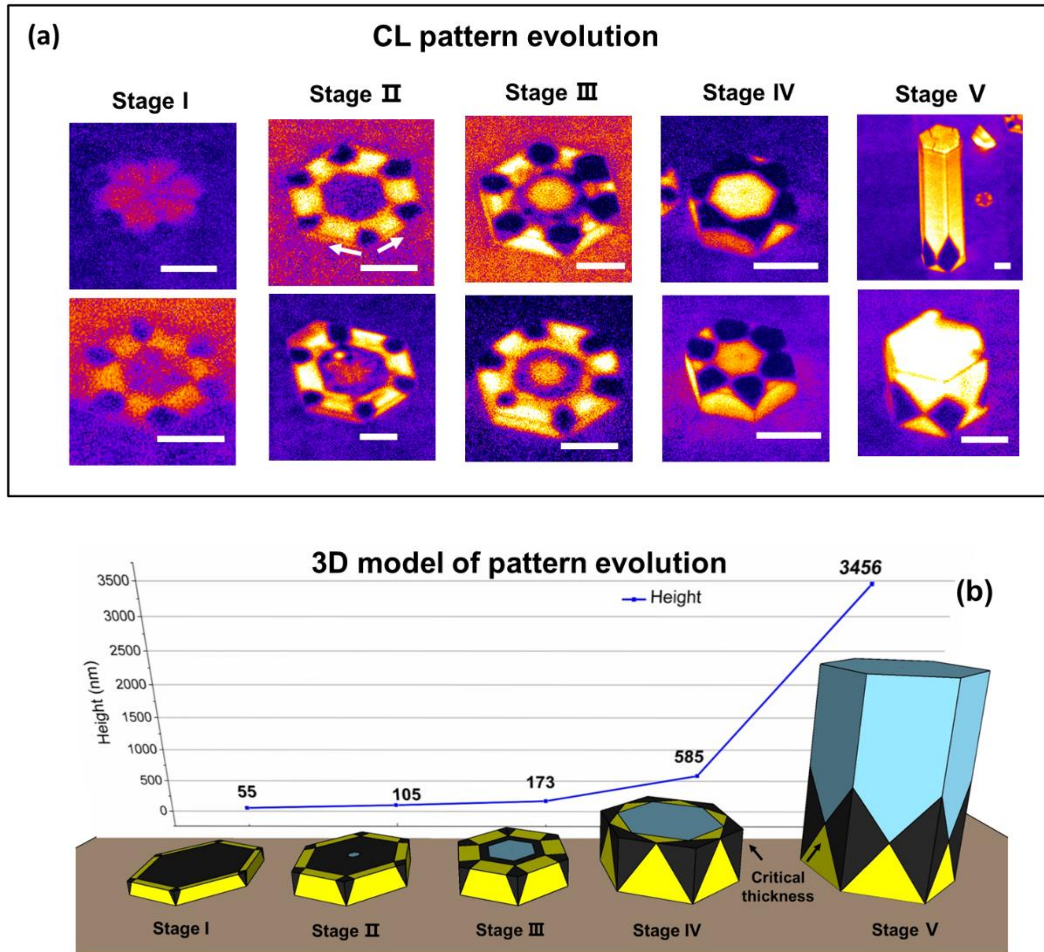

Figure 4.12 CL pattern evolution: (a) Panchromatic CL images demonstrating the evolution of GaN nanostructures categorised into five different stages during growth (scale bar: 500 nm). (b) A 3D illustration of the CL pattern evolution with the average height of each stage. We consider the height of the diamond corner at the nanorod edge area as the critical thickness (a transition height of the diamond shape). The rosette-shaped pattern changed at the critical thickness.

To further study the CL pattern variation in the nanorod, it is necessary to find out how the pattern changes during nanorod growth. Due to the fast-growing speed of the nanorods (estimated at 10 nm/s) [48], it is challenging to acquire nanorods with an extremely short growth time or pinpoint a specific nanorod using an in-situ monitoring system. However, we found nanorods at different growth stages coexisting on the wafer, which we ascribe to continuous nucleation throughout the growth time. By collecting the information of different nanorods over a large CL imaging area, we can obtain information about the various growth stages. We can roughly divide the growth of these

nanorods into five stages based on their heights and illustrate the pattern transformation in 3D in figure 4.12.

In stage I, just after the formation of the nanodisk, it shows non-luminous regions at the hexagon vertices with weak YL surrounding these dark regions, forming a clear petal pattern. The middle region of the disk, has a very weak luminescence. The low CL intensity could be attributed to its small material volume and large strain at the interface. In stage II, the YL becomes more intense at the edges of the hexagon, indicating a higher impurity incorporation in these regions. The non-luminous areas at the vertices, arising from a high density of non-radiative recombination centers, continue to grow in size and expand laterally along the edges of the hexagon (indicated by white arrows) with further growth.

In the next stage (Stage III), strong NBE is observed in the central region, indicating improved optical property compared with the former two stages. A distinct boundary between the dark and bright YL areas could be seen on the sidewall due to the non-luminous region expansion at the vertices. The depth of the dark region extends about 200 nm inside the nanorod's surface, as shown earlier in figure 4.8. On the edge of the hexagonal prism, the joining of boundaries between the bright and dark areas form a profile with a triangular shape.

The expansion of the triangular non-luminous regions could be due to the preferential distribution of non-radiative defects along certain crystallographic directions. Indeed, Zheng *et al.* [49] reported that the surface energies and surface reconstruction of different facets could lead to compositional difference along certain crystallographic directions in AlGaAs growth. However, due to the diversity of angles and shapes, there could be a complex relationship between certain crystallographic directions and the size of the nanorods.

In stage IV, the adjacent dark regions start to merge when nanorod reaches a certain height. The height varies from rod to rod, but the merging process is roughly 200-500 nm (figure 4.11). At this height, the non-radiative process dominates the recombination channels on the sidewalls. In the last stage, a contraction follows the expansion of the non-luminous region. Once the expanding non-luminous regions start to merge, the non-radiative defects are then distributed along another equivalent or other crystallographic directions, thereby ultimately forming a diamond-like pattern. The optical spectrum now shows a strong NBE luminescence with a weak YL along the rest

of the entire length of the rod. The final luminescence pattern consists of diamond-shape dark areas at the bottom section of the nanorod and the bright near-band emission for the rest of the nanorod.

The development and evolution of the rosette-shaped pattern provide a 'time-lapsed' sequence of how YL, non-radiative recombination, and NBE vary during nanorod growth.

4.9 Summary

The rosette-shaped CL pattern is a curious and complicated optical observation that requires extensive combinations of high resolution optical and structural characterization techniques to explore its origins. We found the optical resonance modes and the polarity inversion domains do not contribute to the pattern formation through cavity-shape destruction and polarity determination. Nano-scale SIMS shows a higher concentration of CN clusters and less Si in the rosette-shaped region. Therefore, the CL pattern formation may relate to facet preferential distribution of non-radiative defects, such as excess carbon/nitrogen related defects. A five-stage growth model is proposed to explain the formation and development of the pattern from nanodisks to nanorods. This work helps to extend our understanding of the defect distribution and related optical properties at different stages of GaN nanorod growth, which is useful for future device applications.

Reference

1. J. Neugebauer and C. G. Van de Walle, *Gallium vacancies and the yellow luminescence in GaN.* Applied Physics Letters, 1996. **69**(4): p. 503-505.

2. O. Toshio and A. Masaharu, *Mechanism of yellow luminescence in GaN.* Japanese Journal of Applied Physics, 1980. **19**(12): p. 2395.

3. F. A. Ponce, D. P. Bour, W. Götz and P. J. Wright, *Spatial distribution of the luminescence in GaN thin films.* Applied Physics Letters, 1996. **68**(1): p. 57-59.

4. E. F. Schubert, *Light-emitting diodes*, 2006, Cambridge University Press: Cambridge, New York.

5. H. Liao, J. Li, T. Wei, P. Wen, M. Li and X. Hu, *First-principles study of CN point defects on sidewall surface of [0001]-oriented GaN nanowires.* Applied Surface Science, 2019. **467-468**: p. 293-297.

6. S. O. Kucheyev, M. Toth, M. R. Phillips, J. S. Williams, C. Jagadish and G. Li,

Chemical origin of the yellow luminescence in GaN. Journal of Applied Physics, 2002. **91**(9): p. 5867-5874.

7. J. I. Pankove and J. A. Hutchby, *Photoluminescence of ion-implanted GaN.* Journal of Applied Physics, 1976. **47**(12): p. 5387-5390.

8. X. Li, P. W. Bohn and J. J. Coleman, *Impurity states are the origin of yellow-band emission in GaN structures produced by epitaxial lateral overgrowth.* Applied Physics Letters, 1999. **75**(26): p. 4049-4051.

9. R. Armitage, W. Hong, Q. Yang, H. Feick, J. Gebauer, E. R. Weber, S. Hautakangas and K. Saarinen, *Contributions from gallium vacancies and carbon-related defects to the "yellow luminescence" in GaN.* Applied Physics Letters, 2003. **82**(20): p. 3457-3459.

10. T. Mattila and R. M. Nieminen, *Point-defect complexes and broadband luminescence in GaN and AlN.* Physical Review B, 1997. **55**(15): p. 9571-9576.

11. S. G. Christenson, W. Xie, Y. Y. Sun and S. B. Zhang, *Carbon as a source for yellow luminescence in GaN: Isolated CN defect or its complexes.* Journal of Applied Physics, 2015. **118**(13): p. 135708.

12. M. A. Reshchikov, D. O. Demchenko, A. Usikov, H. Helava and Y. Makarov, *Carbon defects as sources of the green and yellow luminescence bands in undoped GaN.* Physical Review B, 2014. **90**(23): p. 235203.

13. D. O. Demchenko, I. C. Diallo and M. A. Reshchikov, *Yellow luminescence of gallium nitride generated by carbon defect complexes.* Physical Review Letters, 2013. **110**(8): p. 087404.

14. J. L. Lyons, A. Janotti and C. G. Van de Walle, *Carbon impurities and the yellow luminescence in GaN.* Applied Physics Letters, 2010. **97**(15): p. 152108.

15. U. Kaufmann, M. Kunzer, H. Obloh, M. Maier, C. Manz, A. Ramakrishnan and B. Santic, *Origin of defect-related photoluminescence bands in doped and nominally undoped GaN.* Physical Review B, 1999. **59**(8): p. 5561-5567.

16. C. B. Soh, S. J. Chua, H. F. Lim, D. Z. Chi, S. Tripathy and W. Liu, *Assignment of deep levels causing yellow luminescence in GaN.* Journal of Applied Physics, 2004. **96**(3): p. 1341-1347.

17. W. Götz, N. M. Johnson, C. Chen, H. Liu, C. Kuo and W. Imler, *Activation energies of Si donors in GaN.* Applied Physics Letters, 1996. **68**(22): p. 3144-3146.

18. G. A. Slack, L. J. Schowalter, D. Morelli and J. A. Freitas, *Some effects of oxygen impurities on AlN and GaN.* Journal of Crystal Growth, 2002. **246**(3): p. 287-298.

19. M. Toth, K. Fleischer and M. R. Phillips, *Direct experimental evidence for the role of oxygen in the luminescent properties of GaN.* Physical Review B, 1999. **59**(3): p. 1575-1578.

20. B. Liu, F. Yuan, B. Dierre, T. Sekiguchi, S. Zhang, Y. Xu and X. Jiang, *Origin of yellow-band emission in epitaxially grown GaN nanowire arrays.* ACS Applied Materials & Interfaces, 2014. **6**(16): p. 14159-14166.

21. P. M. Coulon, B. Alloing, V. Brändli, P. Vennéguès, M. Leroux and J. Zúñiga-Pérez, *Dislocation filtering and polarity in the selective area growth of GaN nanowires by continuous-flow metal organic vapor phase epitaxy.* Applied Physics Express, 2016. **9**(1): p. 015502.

22. R. Colby, Z. Liang and I. H. Wildeson, *Dislocation filtering in GaN nanostructures.* Nano Letters, 2010. **10**(5): p. 1568-1573.

23. C. Zhao, T. K. Ng, A. Prabaswara, M. Conroy, S. Jahangir, T. Frost, J. O'Connell, J. D. Holmes, P. J. Parbrook, P. Bhattacharya and B. S. Ooi, *An enhanced surface passivation effect in InGaN/GaN disk-in-nanowire light emitting diodes for mitigating shockley–read–hall recombination.* Nanoscale, 2015. **7**(40): p. 16658-16665.

24. Q. Li and G. T. Wang, *Spatial distribution of defect luminescence in GaN nanowires.* Nano Letters, 2010. **10**(5): p. 1554-1558.

25. P. Huang, H. Zong, J. J. Shi, M. Zhang, X. H. Jiang, H. X. Zhong, Y. M. Ding, Y. P. He, J. Lu and X. D. Hu, *Origin of 3.45 eV emission line and yellow luminescence band in GaN nanowires: Surface microwire and defect.* ACS Nano, 2015. **9**(9): p. 9276-9283.

26. M. de la Mata, C. Magen, J. Gazquez, M. I. B. Utama, M. Heiss, S. Lopatin, F. Furtmayr, C. J. Fernández-Rojas, B. Peng, J. R. Morante, R. Rurali, M. Eickhoff, A. Fontcuberta i Morral, Q. Xiong and J. Arbiol, *Polarity assignment in ZnTe, GaAs, ZnO, and GaN-AlN nanowires from direct dumbbell analysis.* Nano Letters, 2012. **12**(5): p. 2579-2586.

27. N. Wang, X. Chen, Y. Yang, J. Dong, C. Wang and G. Yang, *Diffuse reflection inside a hexagonal nanocavity.* Scientific Reports, 2013. **3**(1): p. 1-4.

28. C. Tessarek, R. Goldhahn, G. Sarau, M. Heilmann and S. Christiansen, *Carrier-induced refractive index change observed by a whispering gallery mode shift in GaN microrods.* New Journal of Physics, 2015. **17**(8): p. 083047.

29. T. Christian, D. Christel, S. Erdmann and C. Silke, *Growth of GaN nanorods and wires and spectral tuning of whispering gallery modes in tapered GaN wires.* Japanese Journal of Applied Physics, 2013. **52**(8S): p. 08JE09.

30. T. Kouno, K. Kishino and M. Sakai, *Lasing action on whispering gallery mode of self-organized GaN heagonal microdisk crystal fabricated by rf-plasma-assisted molecular beam epitaxy.* IEEE Journal of Quantum Electronics, 2011. **47**(12): p. 1565-1570.

31. A. C. Tamboli, M. C. Schmidt, A. Hirai, S. P. DenBaars and E. L. Hu, *Observation of whispering gallery modes in nonpolar m-plane GaN microdisks.* Applied Physics Letters, 2009. **94**(25): p. 251116.

32. P. M. Coulon, M. Hugues, B. Alloing, E. Beraudo, M. Leroux and J. Zuniga-Perez, *GaN microwires as optical microcavities: Whispering gallery modes vs fabry-perot modes.* Optics Express, 2012. **20**(17): p. 18707-18716.

33. H. Baek, J. K. Hyun, K. Chung, H. Oh and G. C. Yi, *Selective excitation of fabry-perot or whispering-gallery mode-type lasing in GaN microrods.* Applied Physics Letters, 2014. **105**(20): p. 201108.

34. P. M. Coulon, M. Mexis, M. Teisseire, M. Jublot, P. Vennégués, M. Leroux and J. Zuniga-Perez, *Dual-polarity GaN micropillars grown by metalorganic vapour phase epitaxy: Cross-correlation between structural and optical properties.* Journal of Applied Physics, 2014. **115**(15): p. 153504.

35. I. Volotsenko, M. Molotskii, Z. Barkay, J. Marczewski, P. Grabiec, B. Jaroszewicz, G. Meshulam, E. Grunbaum and Y. Rosenwaks, *Secondary electron doping contrast: Theory based on scanning electron microscope and kelvin probe force microscopy measurements.* Journal of Applied Physics, 2010. **107**(1): p. 014510.

36. H. Seiler, *Secondary electron emission in the scanning electron microscope.* Journal of Applied Physics, 1983. **54**(11): p. R1-R18.

37. C. P. Sealy, M. R. Castell and P. R. Wilshaw, *Mechanism for secondary electron dopant contrast in the SEM.* Journal of Electron Microscopy, 2000. **49**(2): p. 311-321.

38. S. M. Ko, J. H. Kim, Y. H. Ko, Y. H. Chang, Y. H. Kim, J. Yoon, J. Y. Lee and Y. H. Cho, *Growth mechanism of catalyst-free and mask-free heteroepitaxial GaN submicrometer- and micrometer-sized rods under biaxial strain: Variation of surface energy and adatom kinetics.* Crystal Growth & Design, 2012. **12**(8): p. 3838-3844.

39. S. Y. Bae, J. Y. Lee, J. H. Min and D. S. Lee, *Morphology evolution of pulsed-flux Ga-polar GaN nanorod growth by metal organic vapor phase epitaxy and its nucleation dependence.* Applied Physics Express, 2013. **6**(7): p. 075501.

40. X. Yuan, J. Yang, J. He, H. H. Tan and C. Jagadish, *Role of surface energy in nanowire growth.* Journal of Physics D: Applied Physics, 2018. **51**(28): p. 283002.

41. N. Thillosen, K. Sebald, H. Hardtdegen, R. Meijers, R. Calarco, S. Montanari, N. Kaluza, J. Gutowski and H. Lüth, *The state of strain in single GaN nanocolumns as derived from micro-photoluminescence measurements.* Nano Letters, 2006. **6**(4): p. 704-708.

42. B. Gil, F. Hamdani and H. Morkoç, *Oscillator strengths for optical band-to-band processes in GaN epilayers.* Physical Review B, 1996. **54**(11): p. 7678-7681.

43. M. J. Hÿch, E. Snoeck and R . Kilaas, *Quantitative measurement of displacement and strain fields from hrem micrographs.* Ultramicroscopy, 1998. **74**(3): p. 131-146.

44. J. L. Lyons, A. Janotti and C. G. Van de Walle, *Effects of carbon on the electrical and optical properties of InN, GaN, and AlN.* Physical Review B, 2014. **89**(3): p. 035204.

45. A. F. Wright, *Substitutional and interstitial carbon in wurtzite GaN.* Journal of Applied Physics, 2002. **92**(5): p. 2575-2585.

46. P. P. Paskov and B. Monemar, *2 - point defects in group-III nitrides*, in *Defects in advanced electronic materials and novel low dimensional structures*, J. Stehr, I. Buyanova and W. Chen, Editors. 2018, Woodhead Publishing. p. 27-61.

47. C. Takakuwa-Hongo and M. Tomita, *High-sensitivity SIMS analysis of carbon in GaN films by molecular ion detection.* Surface and Interface Analysis, 1997. **25**(13): p. 966-969.

48. B. Zhao, M. N. Lockrey, P. Caroff, N. Wang, L. Li, J. Wong-Leung, H. H. Tan and C. Jagadish, *The effect of nitridation on the polarity and optical properties of GaN self-assembled nanorods.* Nanoscale, 2018. **10**(23): p. 11205-11210.

49. C. Zheng, J. Wong-Leung, Q. Gao, H. H. Tan, C. Jagadish and J. Etheridge, *Polarity-driven 3-fold symmetry of GaAs/AlGaAs core multishell nanowires.* Nano Letters, 2013. **13**(8): p. 3742-3748.

Chapter 5

Growth and characterisation of $In_xGa_{1-x}N$ quantum wells and quantum dots in GaN nanorods

5.1 Introduction

In this chapter, we further explored the growth of $In_xGa_{1-x}N$ quantum wells (QWs) and quantum dots (QDs) on the self-assembled GaN nanorods that have been achieved in previous chapters. Nanowires and nanorods incorporated QWs and multiple QWs (MQWs) have been already used in light-emitting diodes [1-4], solar cells [5-7] and photovoltaic devices [8, 9]. One of the advantages of QWs grown on non-polar m-plane GaN is that the layers are free from quantum-confined Stark effect (QCSE) caused by internal piezoelectric field in c-planes GaN [10]. The natural geometry of GaN nanorods allows this to be achieved by growing InGaN QWs and QDs on their sidewalls to form a core-shell structure. Furthermore, the large surface-area-to-volume ratio of the nanorods provides more area to reduce current overcrowding in the active layers, which in turn resolves the efficiency droop problem. Thick InGaN QWs [11] can also be grown on the m-planes thereby allowing higher indium incorporation to push the emission wavelength towards the longer region beyond the green-gap.

Under certain growth conditions [12], QWs grown on self-assembled GaN nanorods can be accompanied by spontaneous formation of $In_xGa_{1-x}N$ QDs. The formation mechanism of the QDs may be attributed to a large miscibility gap between the InN and GaN material systems. InGaN QDs grown in the core-shell MQWs nanowires have been demonstrated to act as good single-photon emitters with ultrafast radiative lifetimes and polarized emission [12]. $In_xGa_{1-x}N$ QDs could also offer high band offsets, good stability, fast switching rates and large exciton binding energies [13, 14], making them suitable for future applications in quantum technology such as quantum cryptography and quantum computing.

In this chapter, we discuss the growth of $In_xGa_{1-x}N$ MQWs and related QW- and QD-

emission on GaN self-assembled nanorods. The detailed growth process and growth parameters are discussed in section 5.2. In section 5.3, the structural details of the core-shell MQWs are characterized by transmission electron microscopy (TEM). We present a detailed study on spatial distribution and optical properties of the QD emission through high-resolution CL imaging. We also studied the effect of indium injection and barrier growth temperature on the optical properties of the MQWs. A summary of the chapter is then presented in section 5.5.

5.2 Experimental Details

5.2.1 Growth of $In_xGa_{1-x}N$ MQWs on GaN nanorods

The $In_xGa_{1-x}N$/GaN MQWs were grown on GaN self-assembled nanorods. The detailed growth process of the nanorods has already been discussed in chapter 3. The nanorod core contains two segments: the Si-doped (SiH_4 injection) segment was grown first, then followed by an unintentionally doped segment (without SiH_4). Both segments have been grown for 300 s. Before the MQWs growth, the carrier gas was switched from hydrogen to nitrogen and the chamber pressure was increased from 200 to 400 mbar.

Unlike the extremely low V/III ratio used for GaN nanorod growth, the growth conditions for MQWs were quite different. A single loop of the QW and barrier consisted of the following steps: (i) $In_xGa_{1-x}N$ QW was grown at 710°C by simultaneously injecting TEGa (2.31 μmol/min), TMIn (1.68 μmol/min) and NH_3 (5000 sccm) for 120 s. (ii) GaN barrier was grown at 810 °C with increased TEGa flow (20.13 μmol/min) and NH_3 (5000 sccm) for 300 s. This loop was then repeated three times throughout the entire MQW growth including the steps of reheating and cooling, during which group III precursors were removed from the growth chamber.

5.2.2 Optical and structural characterisations

The morphology and optical properties were characterised using a FEI Verios 460 scanning electron microscope (SEM) equipped with a Gatan MonoCL4 Elite CL system. All the CL measurements were conducted at room temperature with 1-5 kV beam voltage and 0.2 nA beam current.

TEM-lamella samples were prepared in a FEI Helios Nanolab focused ion beam (FIB) system, with an ion beam voltage of 30 kV for milling and a voltage of 5 kV for cleaning/polishing any damaged layer caused during the milling. The lamellae were

analysed by TEM using a JOEL 2100F instrument for structural information.

5.3 $In_xGa_{1-x}N$/GaN MQWs and $In_xGa_{1-x}N$ QDs

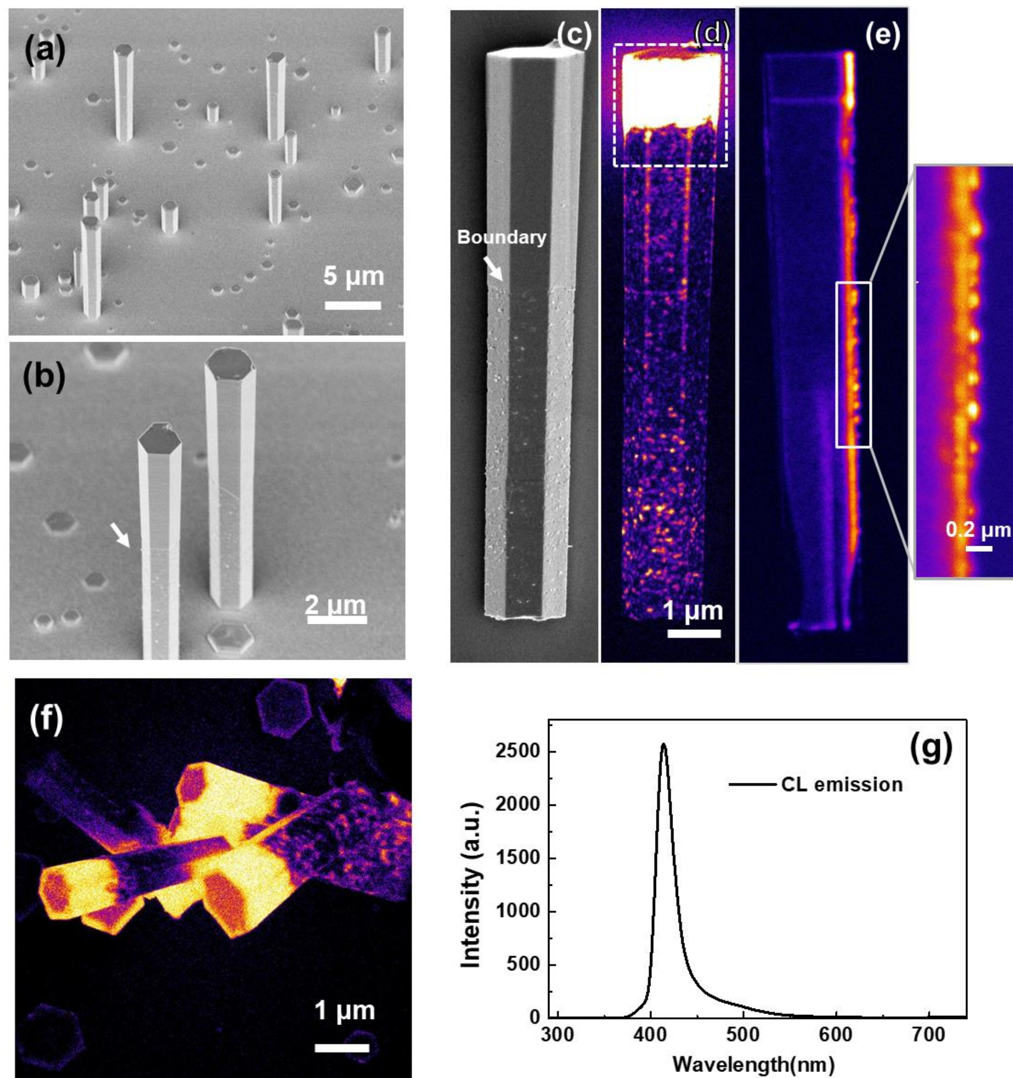

Figure 5.1 SEM, panchromatic CL images and CL spectrum of GaN nanorods with MQW structure: (a, b) 45-degree tilted SEM image of GaN nanorods with MQW structure. A white arrow in figure *b* indicates the boundary between smooth and rough area. (c, d) SEM and corresponding panchromatic CL images of a single GaN nanorod with MQW structure. A white arrow indicates the boundary between the smooth and rough area. (e) The panchromatic CL of the lamella made from the nanorod shown in figure *c* (sliced along the growth direction) (f) Panchromatic image of laying down nanorod on the sapphire substrate. (g) CL spectrum of the QW emission collected from the area indicated in a white dashed box in figure *c*.

SEM images of the GaN nanorods grown with $In_xGa_{1-x}N$/GaN MQWs are shown in figures 5.1 (a) and (b), where the hexagonal morphology of the nanorods are clearly maintained. However, the surface of the bottom segment (Si-doped) of the nanorod appears to be rough with dots formation (figure 5.1 *c*). A clear boundary between the rough and the smooth segments demarcates where the SiH_4 precursor was removed during growth (indicated by a white arrow). The rough surface could be related to the thin layer of SiN_x formed on the sidewalls with the use of SiH_4 precursor during GaN core growth [12].

The nanorod emits two kinds of luminescence: the top region emits strong QW-like emission, while the rest shows bright QD-like emission (figure 5.1 *d*). This could also be seen in the lamella sliced in FIB along the growth direction (figure 5.6 *e*) that the QD emission is less than 50 nm in diameter and well-separated. The spectrum collected from top QW region peaks at 415 nm (region marked by a white dashed box). In this area, the surrounding sidewalls of the nanorod emit stronger CL luminescence compared with the top surface as could be seen in figure 5.1 (f) of some nanorods that have been knocked down from their substrate.

To reveal the structural difference between the top area and the rest of the rod, the TEM and STEM were conducted on a nanorod lamella with the MQW structure. As shown in figure 5.2 (b), three $In_xGa_{1-x}N$/GaN MQWs can be clearly seen to form around the nanorod, forming not only radially on the sidewalls but also axially on the top surface. The thicknesses of QWs and barriers grown on the top and sidewalls are different, which could be related to different growth rates on c- and m-planes, respectively [15].

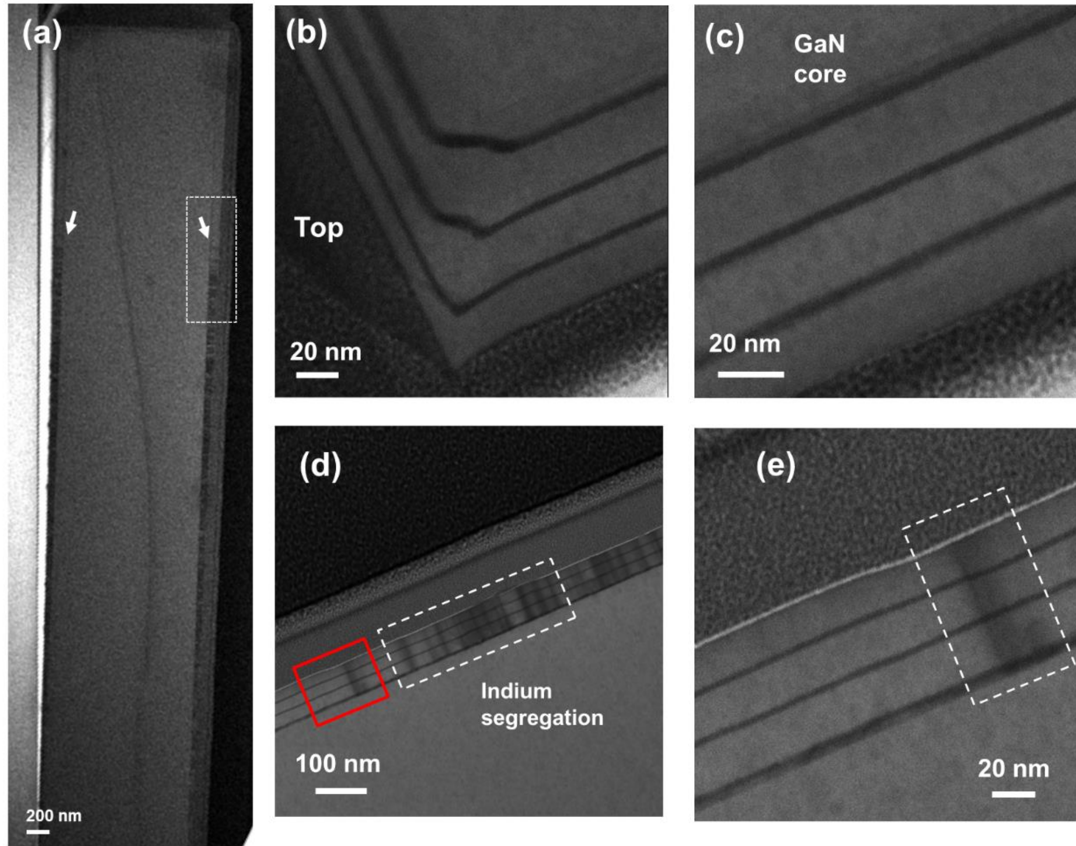

Figure 5.2 (a) STEM bright field image of the MQW cross-section lamella. The white arrows roughly point out where the indium segregation starts. (b, c). STEM bright field image of the MQW cross-section lamella, focusing on the top & sidewall area, zone axis [11-20]. (d, e) STEM bright field image of the indium segregation area (as marked by a white dashed box). Figure e is a zoomed-in image of the red box area in figure d.

The interfaces of the MQWs could be clearly identified from the top section of the nanorod (which corresponds to the bright emission region). However, this is not so for the rest of the nanorod, where the MQWs have darker contrast between QWs as shown in figure 5.2 (e) and (f). Since STEM contrast is related to Z-contrast, this dark regions in the MQWs could be related to indium segregation. Indium segregation has been reported and debated since the late 1990s [16-19], which is mainly attributed to the low miscibility between GaN and InN [20]. The indium segregation could have been resulted from high indium content in the $In_xGa_{1-x}N$ QW (25- 65% Indium) [21], QW thickness exceeding the critical thickness [21-23] and inhomogeneous strain distribution in the QW [24]. The structural difference in the nanorod may correspond to the CL emission distribution: the top QW region emits the bright CL signal, while the indium segregation region emits isolated dot-like emission.

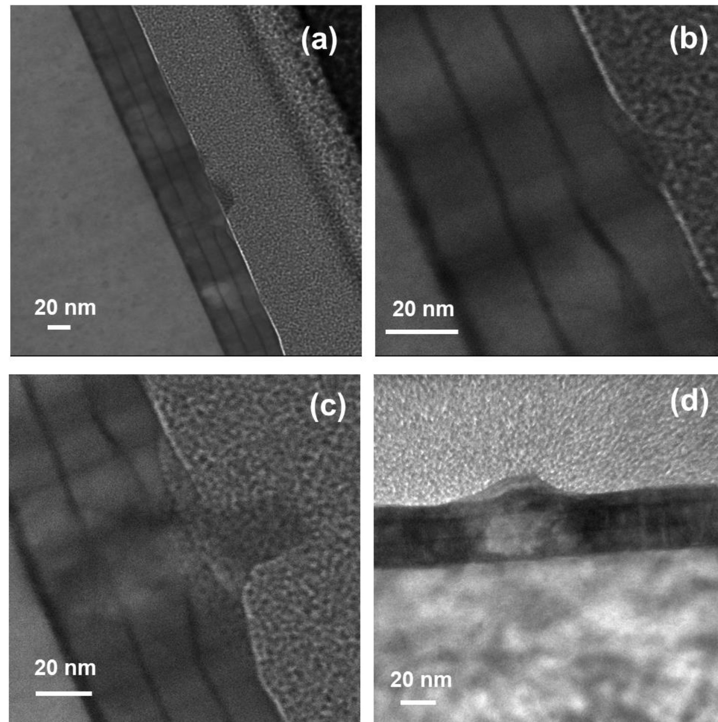

Figure 5.3 (a-d) TEM images of the dot-like formation on the surface of the InxGa1-xN MQWs.

The TEM images of QDs forming on the side facets of the MQW structure are shown in figure 5.3. The size of the QDs is around 20 nm and appear to nucleate only on the sidewalls of the nanorod and not in the QWs. Most of them have a truncated pyramid shape. The dots have a higher density towards the bottom half of the nanorod, suggesting that Si incorporation during the first stage of nanorod growth results in a rougher surface that promotes nucleation of the dots.

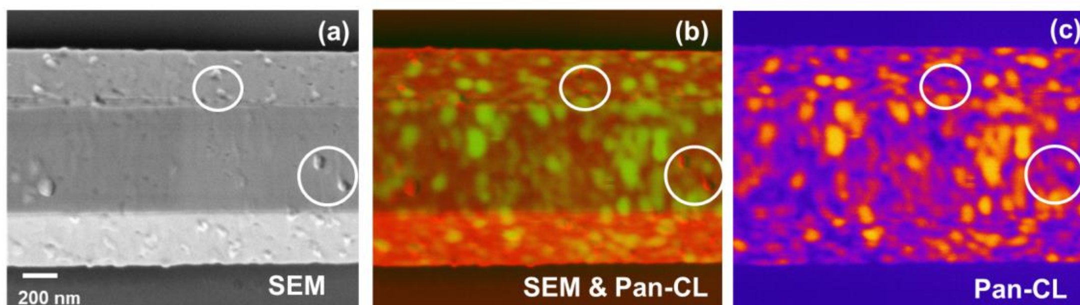

Figure 5.4 SEM and panchromatic CL images of the QDs: (a) SEM, SEM (red) & panchromatic CL (green) composite image and panchromatic CL image, respectively. The dots

are highlighted with white circles.

To get a better clarification on the QD emission, we compared the SEM and CL images from the nanorod, as shown in figure 5.4. In the SEM image, QDs can be clearly seen as indicated by the white circles. However, the SEM & CL composite image (figure 5.4 b) shows that emissions (green regions) are scattered all over the nanorods but does not coincide with the locations of the QDs. Therefore, it is believed that emission is actually coming from the underlying QW regions, rather than the surface QDs. QD-like emission from inside InGaN QWs has been reported in previous studies [17, 18, 25]. The formation of the QD-like emissions were attributed to the restricted indium solubility in GaN [25] and they may be related to compositional modulation in the InGaN ternary system due to phase separation [16, 18].

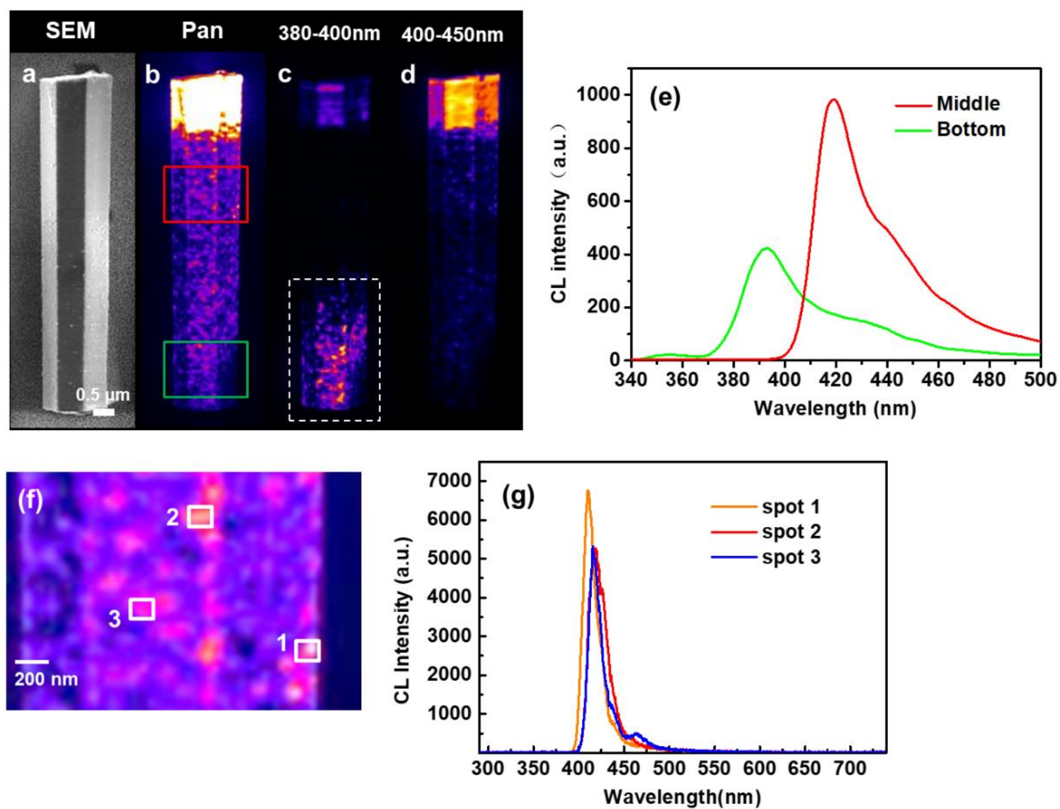

Figure 5.5 SEM, panchromatic CL images and CL spectra of the MQW and QDs: (a, b) SEM and corresponding panchromatic CL images of a GaN nanorod with MQW structure. Two boxes (red and green) mark out the spectral collection region in figure *c*. (c, d) CL images reconstructed from the spectral mapping, 380-400 nm and 400-450 nm, respectively. (e) CL

spectra collected at the middle and bottom area of the nanorod (marked by red and green dashed boxes in figure b). (f, g) CL spectra extracted from three quantum dots as marked in the magnified image in figure f.

The spatial and spectral distributions of CL emission from the MQWs and QDs are also investigated. As shown in figure 5.5 (e), there is a shift around 25 nm in emission peak between the top (centered at 419 nm) and the bottom (centered at 393 nm) areas of the nanorod. This also reflects in the spatial distribution of CL emission in figure 5.5 (c) and (d). The bottom area is bright at shorter wavelength (380 nm to 400 nm), while the middle and top area is brighter at longer wavelengths ranging from 450 nm to 500 nm. These results show that QDs at the bottom on average, have less indium incorporation compared to the ones closer to top of the nanorod. This higher indium incorporation may be related to the direct impinging [26, 27] of indium atoms towards the top areas.

We picked out three spots (figure 5.5 *f*) for spectral analysis. We found each spot have slightly different peaks: 416 nm at spot 1, 410 nm at spot 2 and 418 nm at spot 3. All the peaks are sharp with low full width at half maximum around 20 nm, which means after further optimizing the growth process, they may have potential for the applications in single-photon emitters [12].

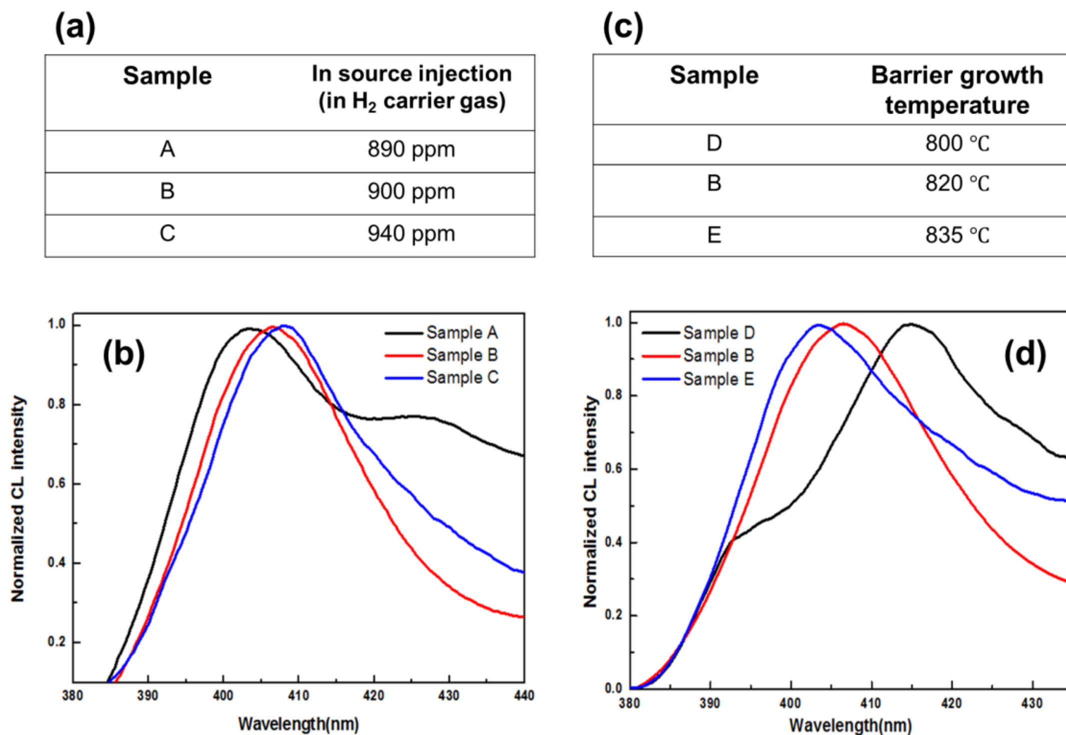

(a)

Sample	In source injection (in H_2 carrier gas)
A	890 ppm
B	900 ppm
C	940 ppm

(c)

Sample	Barrier growth temperature
D	800 ℃
B	820 ℃
E	835 ℃

Figure 5.6 CL spectra studies of MQW with indium injection concentration and barrier growth

temperature variations: (a) $In_xGa_{1-x}N$/GaN single quantum well growth with indium injection concentration variation. (b) The CL spectra correspond to the variation of indium injection concentration. (c) $In_xGa_{1-x}N$/GaN single quantum well growth with different barrier growth temperature. (d) The CL spectra correspond to the variation of barrier growth temperature.

We studied the effect of the barrier growth temperature and TMIn flow rate on the optical properties of the $In_xGa_{1-x}N$/GaN QWs. In order not to complicate the results, only one QW was grown in this set of samples and the CL spectra were collected from the whole nanorod. With the increase of TMIn flow from 1.66 to 1.75 µmol/min, a shift to longer wavelength in the QW emission is observed (figure 5.6 *b*), as expected due to an increase in indium concentration which reduces the effective bandgap of the QW.

When the growth temperature of the barriers is increased from 800 to 835 °C, a shift to shorter wavelength is observed due to the decreased indium incorporation in the QW. Because of the miscibility gap between GaN and InN, the solubility of indium in the $In_{1-x}Ga_xN$ alloy is extremely sensitive to the temperature during or after the QW growth [28, 29]. The increased barrier growth temperature could result in the out-diffusion and evaporation of indium from the QWs, resulting in a reduced indium content in the QW and/or reduction in the thickness of the QW [29], and therefore a blueshift in the emission spectrum of the QW.

5.4 Summary

We have successfully grown GaN nanorods with $In_xGa_{1-x}N$/GaN MQW core-shell structures, which show strong emission from the MQWs, especially in the top section of the nanorods. Detailed CL and TEM studies show that MQWs grown at the top region of the nanorod have better crystalline and optical qualities. From the CL mapping, we found $In_xGa_{1-x}N$ QD-like emission on the sidewalls of the nanorods, which originated from indium phase segregation in the QWs. We also investigated the effects of MQW growth parameters on their optical properties that we found increasing indium source injection and decreasing barrier growth temperature would lead to an emission shift to longer wavelength.

Reference

1. C. Zhao, T. K. Ng, R. T. ElAfandy, A. Prabaswara, G. B. Consiglio, I. A. Ajia,

I. S. Roqan, B. Janjua, C. Shen, J. Eid, A. Y. Alyamani, M. M. El-Desouki and B. S. Ooi, *Droop-free, reliable, and high-power InGaN/GaN nanowire light-emitting diodes for monolithic metal-optoelectronics.* Nano Letters, 2016. **16**(7): p. 4616-4623.

2. B. O. Jung, S. Y. Bae, S. Lee, S. Y. Kim, J. Y. Lee, Y. Honda and H. Amano, *Emission characteristics of InGaN/GaN core-shell nanorods embedded in a 3D light-emitting diode.* Nanoscale Research Letters, 2016. **11**(1): p. 1-10.
3. X. Dai, A. Messanvi, H. Zhang, C. Durand, J. Eymery, C. Bougerol, F. H. Julien and M. Tchernycheva, *Flexible light-emitting diodes based on vertical nitride nanowires.* Nano letters, 2015. **15**(10): p. 6958-6964.
4. J. R. Riley, S. Padalkar, Q. Li, P. Lu, D. D. Koleske, J. J. Wierer, G. T. Wang and L. J. Lauhon, *Three-dimensional mapping of quantum wells in a GaN/InGaN core–shell nanowire light-emitting diode array.* Nano Letters, 2013. **13**(9): p. 4317-4325.
5. M. Ebaid, J. H. Kang and S. H. Lim, *Enhanced solar hydrogen generation of high density, high aspect ratio, coaxial InGaN/GaN multi-quantum well nanowires.* Nano Energy, 2015. **12**: p. 215-223.
6. S. L. Howell, S. Padalkar, K. Yoon, Q. Li, D. D. Koleske, J. J. Wierer, G. T. Wang and L. J. Lauhon, *Spatial mapping of efficiency of GaN/InGaN nanowire array solar cells using scanning photocurrent microscopy.* Nano Letters, 2013. **13**(11): p. 5123-5128.
7. A. T. M. Golam Sarwar and R. C. Myers, *Exploiting piezoelectric charge for high performance graded InGaN nanowire solar cells.* Applied Physics Letters, 2012. **101**(14): p. 143905.
8. S. Mokkapati and C. Jagadish, *Review on photonic properties of nanowires for photovoltaics.* Optics Express, 2016. **24**(15): p. 17345-17358.
9. L. Redaelli, A. Mukhtarova, A. Ajay, A. Núñez-Cascajero, S. Valdueza-Felip, J. Bleuse, C. Durand, J. Eymery and E. Monroy, *Effect of the barrier thickness on the performance of multiple-quantum-well InGaN photovoltaic cells.* Japanese Journal of Applied Physics, 2015. **54**(7): p. 072302.
10. H. Sekiguchi, K. Kishino and A. Kikuchi, *Emission color control from blue to red with nanocolumn diameter of InGaN/GaN nanocolumn arrays grown on same substrate.* Applied Physics Letters, 2010. **96**(23): p. 231104.
11. K. C. Kim, M. C. Schmidt, H. Sato, F. Wu, N. Fellows, Z. Jia, M. Saito, S. Nakamura, S. P. DenBaars and J. S. Speck, *Study of nonpolar m-plane InGaN/GaN multiquantum well light emitting diodes grown by homoepitaxial metal-organic chemical vapor deposition.* Applied Physics Letters, 2007. **91**(18): p. 181120.
12. T. J. Puchtler, T. Wang, C. X. Ren, F. Tang, R. A. Oliver, R. A. Taylor and T. Zhu, *Ultrafast, polarized, sngle-photon emission from m-plane InGaN quantum dots on GaN nanowires.* Nano Letters, 2016. **16**(12): p. 7779-7785.
13. B. Monemar, *Fundamental energy gap of GaN from photoluminescence excitation spectra.* Physical Review B, 1974. **10**(2): p. 676-681.
14. M. J. Holmes, K. Choi, S. Kako, M. Arita and Y. Arakawa, *Room-temperature triggered single photon emission from a III-nitride site-controlled nanowire quantum dot.* Nano Letters, 2014. **14**(2): p. 982-986.
15. Y. H. Ra, R. Navamathavan, S. Kang and C. R. Lee, *Different characteristics of InGaN/GaN multiple quantum well heterostructures grown on m- and r-planes of a single n-GaN nanowire using metalorganic chemical vapor deposition.* Journal of Materials Chemistry C, 2014. **2**(15): p. 2692-2701.

16. I. h. Ho and G. B. Stringfellow, *Solid phase immiscibility in GaInN.* Applied Physics Letters, 1996. **69**(18): p. 2701-2703.
17. S. Chichibu, T. Azuhata, T. Sota and S. Nakamura, *Luminescences from localized states in InGaN epilayers.* Applied Physics Letters, 1997. **70**(21): p. 2822-2824.
18. Y. Narukawa, Y. Kawakami, M. Funato, S. Fujita, S. Fujita and S. Nakamura, *Role of self-formed InGaN quantum dots for exciton localization in the purple laser diode emitting at 420 nm.* Applied Physics Letters, 1997. **70**(8): p. 981-983.
19. R. Singh, D. Doppalapudi, T. D. Moustakas and L. T. Romano, *Phase separation in InGaN thick films and formation of InGaN/GaN double heterostructures in the entire alloy composition.* Applied Physics Letters, 1997. **70**(9): p. 1089-1091.
20. B. N. Pantha, J. Li, J. Y. Lin and H. X. Jiang, *Single phase $In_xGa_{1-x}N$ ($0.25 \leq x \leq 0.63$) alloys synthesized by metal organic chemical vapor deposition.* Applied Physics Letters, 2008. **93**(18): p. 182107.
21. Y. T. Moon, D. J. Kim, K. M. Song, C. J. Choi, S. H. Han, T. Y. Seong and S. J. Park, *Effects of thermal and hydrogen treatment on indium segregation in InGaN/GaN multiple quantum wells.* Journal of Applied Physics, 2001. **89**(11): p. 6514-6518.
22. A. Sohmer, J. Off, H. Bolay, V. Härle, V. Syganow, J. Seo Im, V. Wagner, F. Adler, A. Hangleiter, A. Dörnen, F. Scholz, D. Brunner, O. Ambacher and H. Lakner, *GaInN/GaN-heterostructures and quantum wells grown by metalorganic vapor-phase epitaxy.* MRS Internet Journal of Nitride Semiconductor Research, 2014. **2**: p. e14.
23. M. D. McCluskey, L. T. Romano, B. S. Krusor, D. P. Bour, N. M. Johnson and S. Brennan, *Phase separation in InGaN/GaN multiple quantum wells.* Applied Physics Letters, 1998. **72**(14): p. 1730-1732.
24. H. K. Cho, J. Y. Lee, C. S. Kim and G. M. Yang, *Influence of strain relaxation on structural and optical characteristics of InGaN/GaN multiple quantum wells with high indium composition.* Journal of Applied Physics, 2002. **91**(3): p. 1166-1170.
25. K. P. O'Donnell, R. W. Martin and P. G. Middleton, *Origin of luminescence from InGaN diodes.* Physical Review Letters, 1999. **82**(1): p. 237-240.
26. R. K. Debnath, R. Meijers, T. Richter, T. Stoica, R. Calarco and H. Luth, *Mechanism of molecular beam epitaxy growth of GaN nanowires on Si(111).* Applied Physics Letters, 2007. **90**(12): p. 123117.
27. J. Ristić, E. Calleja, S. Fernández-Garrido, L. Cerutti, A. Trampert, U. Jahn and K. H. Ploog, *On the mechanisms of spontaneous growth of III-nitride nanocolumns by plasma-assisted molecular beam epitaxy.* Journal of Crystal Growth, 2008. **310**(18): p. 4035-4045.
28. S. Kim, K. Lee, K. Park and C. S. Kim, *Effects of barrier growth temperature on the properties of InGaN/GaN multi-quantum wells.* Journal of Crystal Growth, 2003. **247**(1): p. 62-68.
29. S. T. Pendlebury, P. J. Parbrook, D. J. Mowbray, D. A. Wood and K. B. Lee, *InGaN/GaN quantum wells with low growth temperature GaN cap layers.* Journal of Crystal Growth, 2007. **307**(2): p. 363-366.

Chapter 6

Conclusion

6.1 Outcomes

This thesis has investigated the wafer-scale growth of GaN self-assembled nanorods on sapphire substrates using metalorganic chemical vapour deposition (MOCVD). We studied how the pre-growth and growth conditions affected the nanorods. We observed a rosette-shape cathodoluminescence pattern in the GaN nanorods and its origin was also explored. Finally, we have grown $In_xGa_{1-x}N$/GaN multi-quantum well (MQW) structure and $In_xGa_{1-x}N$ quantum dots (QDs) on the GaN nanorods for future device applications.

We have investigated the effects of both the pre-growth and growth parameters on the GaN self-assembled nanorods in chapter 3. The nitridation process plays an important role in improving the morphology, polarity, and optical properties of the nanorods. Without appropriate nitridation, the nanorods would exhibit pyramidal top, mixed polarity, and non-uniform yellow luminescence. The introduction of the nitridation process transforms the nanorods into a hexagonal shape with a flat top, N-polarity, and homogenous luminescence distribution with a strong near-band edge emission. We also found that an appropriate silane injection rate and growth temperature are required to obtain nanorods with uniform morphology and high density. In chapter 3, we offered an insight into the relationship between pre-growth, growth conditions, and nanorod properties, which would help provide optimised nanorods for future device applications.

In chapter 4, we studied the rosette-shaped cathodoluminescence (CL) pattern from the GaN nanorods consisting of yellow luminescence (YL) and non-luminous regions. This pattern is formed at the very early stages of GaN nanorod growth and is not affected by nanorod geometry, symmetry, or size. From CL, electron microscopy and nanoscale secondary ion mass spectrometry (nano-SIMS) studies, we found the pattern is not due to optical resonance modes or polarity inversion domains. Higher concertation of CN cluster at the rosette-shape area is observed and therefore, the unique CL pattern formation could be related to facet preferential distribution of non-radiative defects, such as excess carbon/nitrogen related defects. We proposed a five-

stage growth model to explain the formation and development of the pattern from nanodisks to nanorods. This chapter helps to extend our understanding of the defects and their related optical properties at different stages of GaN nanorod growth, which contributes to the knowledge of synthesizing nanorods with desirable optical properties.

The growth and characterisation of $In_xGa_{1-x}N$/GaN MQW core-shell structures and the formation of $In_xGa_{1-x}N$ QDs emission are discussed in chapter 5. Through high-resolution CL and transmission electron microscopy (TEM) studies, we found the tip region of the nanorod emits strong QW emission, while indium segregations are observed along the sidewalls of the nanorods. The $In_xGa_{1-x}N$ MQW emission shows high sensitivity to minor changes in trimethylindium (TMIn) source flow and quantum barrier growth temperature. Increasing indium source injection and decreasing quantum barrier growth temperature shift the emission peaks to longer wavelengths as a result of more indium incorporation. This chapter adds our understanding of the growth and optical properties of the $In_xGa_{1-x}N$/GaN MQW and QDs that would be applied in optoelectronic devices such as light-emitting diodes (LEDs) in the future.

6.2 Outlook and future work

In this thesis, considerable progress in the understanding of self-assembled GaN and related $In_xGa_{1-x}N$/GaN multi-quantum well and quantum dot nanorod structures has been made. However, many challenges remain to be tackled. Here we address a few of these challenges and possible future work direction on this topic.

6.2.1 Challenges in nanorod growth and characterisation

We have successfully grown GaN and $In_xGa_{1-x}N$/GaN MQW nanorods, but challenges still existed to achieve nanorods with highly uniform morphology, optical emissions, and the more accurate characterisation results.

(i) Improving the uniformity in height. Both nanorods and nanodisks co-exist on the same substrate, and this height dispersion may be related to continuous nucleation during the growth. Increasing the nucleus density by adjusting the growth conditions may help suppress continuous nucleation and improve the height uniformity.

(ii) Growing GaN nanorods with an appropriate diameter. As the diameters of the nanorods are around 500 nm, the large diameter of the nanorod requires a thick metal layer to form a continuous metal to form contacts in single nanorod device fabrication

[1, 2]. Therefore, adjusting the growth parameters and reducing the nanorod diameter down to 200 nm would be a goal for future growth optimization.

(iii) Achieving uniform MQW emission. We have successfully grown core-shell MQW structure but the strong MQW emission is restricted at the tip of the nanorods. To improve the efficiency of the emission from the nanorods, it is necessary to obtain uniform emission from the entire nanorods.

(iv) Controlling QD emission. Controlling the concentration and location of QD formation should be tackled in future work. Several parameters, such as Si-doping, indium injection concentration, and growth temperature, might be the key to solving this problem.

6.2.2 Future Outlook

Based on $In_xGa_{1-x}N$/GaN MQW growth, the fabrication of the nanorod devices such as nanorod LEDs could be realized in the future. There are several research topics to be tackled such as n-/p- type doping and contacting the nanorods for current injection.

We have studied the effects of n-type dopant silane in chapter 3 where it has significant effects on the morphology and density of the nanorods. Further studies should be carried out on its effects on the optical and electrical properties of GaN nanorod. Effects of p-type doping using bis(cyclopentadienyl) magnesium (Cp_2Mg) on the properties of nanorods should also be studied in the future. Nanorods with n-i-p structures would be grown to investigate their optical and electrical properties.

Examples of contacting the core-shell structure nanorod are shown in figure 6.1. Typical steps of contacting GaN single nanorod are reported by Durand *et al.* [6]: (i). The nanorod is encapsulated in a spin-on-glass layer that transformed into SiO_x by annealing. (ii). Dry etching is used to reveal the wire surface and e-beam lithography is used to define the metal contacts areas. (iii). N-type and p-type of the segment is contacted with Ti/Al/Ti/Au and Ni/Au metal layers, respectively. To contact a core-shell structured nanorod, one of the contacts should be made on the shell segment, while at the other end of the rod, the shell should be etched away to enable the contact on the core segment [7, 8].

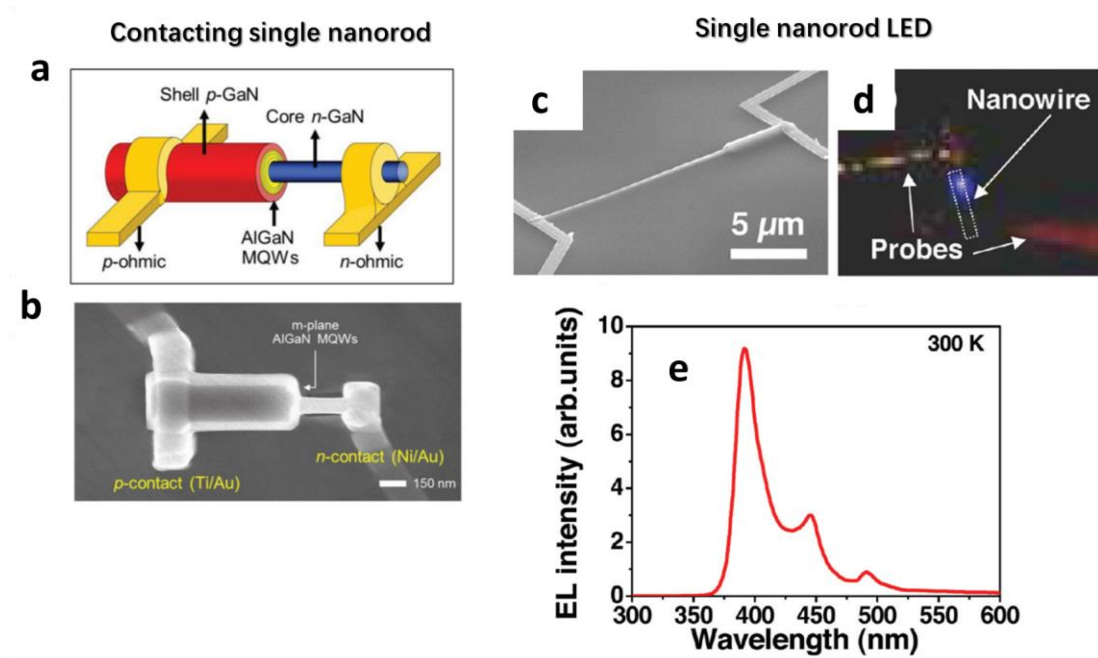

Figure 6.1 Illustrations of single nanorod contacting and single nanorod LED: (a-b) a 3D illustration and SEM image of the single nanorod contacting [9]. (c-e）SEM image, optical microscope, and electroluminescence [7].

Many groups [8, 10-13] have successfully fabricated the single nanorod LEDs. Koester *et al.*[10] has reported a single nanorod LED emits around 392 nm and the indium content inside the $In_xGa_{1-x}N$/GaN MQW is around 16%. Durand *et al.* [6] have demonstrated a GaN/InAlN MQW single nanorod LED that the indium content in the MQW is around 15 % and the bandgap of its emission is around 3.7 eV. To enhance the performance of the nanorod LED, we should focus on several aspects. Firstly, a high-quality p-doped layer is necessary to ensure an effective p-type doping and a high hole-injection rate [14]. Secondly, an effective electron-blocking layer is necessary to increase carrier recombination efficiency. Also, good Ohmic contacts and designs that reduce the optical loss are both beneficial to improve the efficiency of the LEDs [14].

Reference

1. M. Tchernycheva, A. Messanvi, A. de Luna Bugallo, G. Jacopin, P. Lavenus, L. Rigutti, H. Zhang, Y. Halioua, F. H. Julien, J. Eymery and C. Durand, *Integrated photonic platform based on InGaN/GaN nanowire emitters and detectors.* Nano Letters, 2014. **14**(6): p. 3515-3520.
2. F. Qian, S. Gradečak, Y. Li, C. Y. Wen and C. M. Lieber, *Core/multishell nanowire heterostructures as multicolor, high-efficiency light-emitting diodes.* Nano Letters, 2005. **5**(11): p. 2287-2291.

3. T. Langer, H. Jönen, A. Kruse, H. Bremers, U. Rossow and A. Hangleiter, *Strain-induced defects as nonradiative recombination centers in green-emitting GaInN/GaN quantum well structures.* Applied Physics Letters, 2013. **103**(2): p. 022108.
4. W. Liu, C. Mounir, G. Rossbach, T. Schimpke, A. Avramescu, H. J. Lugauer, M. Strassburg, U. Schwarz, B. Deveaud and G. Jacopin, *Spatially dependent carrier dynamics in single InGaN/GaN core-shell microrod by time-resolved cathodoluminescence.* Applied Physics Letters, 2018. **112**(5): p. 052106.
5. P. C. Upadhya, J. A. Martinez, Q. Li, G. T. Wang, B. S. Swartzentruber, A. J. Taylor and R. P. Prasankumar, *Space-and-time-resolved spectroscopy of single GaN nanowires.* Applied Physics Letters, 2015. **106**(26): p. 263103.
6. C. Durand, C. Bougerol, J. F. Carlin, G. Rossbach, F. Godel, J. Eymery, P. H. Jouneau, A. Mukhtarova, R. Butté and N. Grandjean, *M-plane GaN/InAlN multiple quantum wells in core–shell wire structure for UV emission.* ACS photonics, 2013. **1**(1): p. 38-46.
7. C. H. Liao, W. M. Chang, H. S. Chen, C. Y. Chen, Y. F. Yao, H. T. Chen, C. Y. Su, S. Y. Ting, Y. W. Kiang and C. C. Yang, *Geometry and composition comparisons between c-plane disc-like and m-plane core-shell InGaN/GaN quantum wells in a nitride nanorod.* Optics Express, 2012. **20**(14): p. 15859-15871.
8. M. Tchernycheva, P. Lavenus, H. Zhang, A. V. Babichev, G. Jacopin, M. Shahmohammadi, F. H. Julien, R. Ciechonski, G. Vescovi and O. Kryliouk, *InGaN/GaN core–shell single nanowire light emitting diodes with graphene-based p-contact.* Nano Letters, 2014. **14**(5): p. 2456-2465.
9. Y. H. Ra, S. Kang and C. R. Lee, *Ultraviolet light-emitting diode using nonpolar AlGaN core–shell nanowire heterostructures.* Advanced Optical Materials, 2018. **6**(14): p. 1701391.
10. R. Koester, J. S. Hwang, D. Salomon, X. Chen, C. Bougerol, J. P. Barnes, D. L. S. Dang, L. Rigutti, A. de Luna Bugallo and G. Jacopin, *M-plane core–shell InGaN/GaN multiple-quantum-wells on GaN wires for electroluminescent devices.* Nano Letters, 2011. **11**(11): p. 4839-4845.
11. S. W. Kim, Y. H. Park, I. Kim, T. E. Park, B. W. Kwon, W. K. Choi and H. J. Choi, *Synthesis of p-type GaN nanowires.* Nanoscale, 2013. **5**(18): p. 8550-8554.
12. L. Yan, S. Jahangir, S. A. Wight, B. Nikoobakht, P. Bhattacharya and J. M. Millunchick, *Structural and optical properties of disc-in-wire InGaN/GaN LEDs.* Nano Letters, 2015. **15**(3): p. 1535-1539.
13. X. Wang, W. Peng, R. Yu, H. Zou, Y. Dai, Y. Zi, C. Wu, S. Li and Z. L. Wang, *Simultaneously enhancing light emission and suppressing efficiency droop in GaN microwire-based ultraviolet light-emitting diode by the piezo-phototronic effect.* Nano Letters, 2017. **17**(6): p. 3718-3724..
14. A. M. Nahhas, *Review of GaN nanostructured based devices.* American Journal of Nanomaterials, 2018. **6**(1): p. 1-14.